Thermoelectric Stability of Cu_2Se and Magnetic Phenomena in (Ti, Zr, Hf)NiSn Half-Heusler Alloys

by

Trevor Paul Bailey

A dissertation submitted in partial fulfillment
of the requirements for the degree of
Doctor of Philosophy
(Physics)
in the University of Michigan
2020

Doctoral Committee:

Professor Ctirad Uher, Chair
Professor Massoud Kaviany
Professor Çağliyan Kurdak
Professor Lu Li
Associate Professor Pierre Ferdinand Poudeu Poudeu

Trevor Paul Bailey

tpbailey@umich.edu

ORCID ID: 0000-0002-5229-881X

I dedicate this work to my parents, Bruce and Cheryl Bailey, who devoted themselves to my upbringing, provided their support and love, and without whom, I would be nothing.

ACKNOWLEDGEMENTS

The work included herein is primarily that for which I was the main driving force during the past five years at the University of Michigan (UM). The work would not be possible, however, without the guidance and support of many others.

Professor Ctirad Uher has been fundamental in my development as a scientist. His 50+ years of experience in condensed matter physics make him a walking compendium of everything regarding thermoelectrics, superconductivity, magnetism, sample synthesis, measurement techniques and much more. When he and I met to discuss the first draft of my first paper, I of course felt nervous to argue certain points to someone who has essentially seen it all before. But, as with everything he does, he approached the manuscript with energy and rigor and helped me gain the necessary confidence in my work to see it to completion. As a more senior, independent graduate student, I have thoroughly enjoyed our countless meetings full of stimulating physics discussions.

Our closest collaboration at UM is with Associate Professor Pierre Ferdinand Poudeu Poudeu of Materials Science & Engineering. His wealth of thermoelectrics knowledge, synthesis capabilities, and creative projects have been integral to my success as a graduate student. Indeed, Chapters 4 and 5 of this thesis all started with a project he developed regarding magnetic thermoelectrics. I am grateful for the opportunity he allowed me in working alongside a number of his graduate students, especially Dr. Alan Olvera, Dr. Juan Lopez, and Dr. Ruiming Lu.

Professor Lu Li was one of the first members of the Physics Department whom I met during my visit to UM as a senior undergraduate student. His youthful energy and plethora of interesting projects are some of the reasons I decided to attend graduate school here. We have worked closely

over the past few years on several project proposals, and he has remained a role model for my own research. In a similar vein, Professor Çağliyan Kurdak was an important figure in me joining UM. His vibrancy, ingenuity and collaborative spirit were all welcoming signs.

Heat Transfer Physics (ME 539), with Professor Massoud Kaviany, strengthened my knowledge of electrons, phonons, the Boltzmann Transport Equation and much more. It was a pleasure working with Professor Kaviany on a few particularly challenging problem sets. His own thermoelectrics research has also served as a frequent reference for me.

Several alumni of Professor Uher's research group were critical in my training, regarding both experiments and theory. First, Dr. Hang Chi was my initial mentor who taught me most of the measurement techniques in the lab, shared with me his expertise in molecular beam epitaxy, and motivated me to pursue my first project on Cu_2Se. Dr. Si Hui guided me through several of my first measurements, helped me think about the progression of the Cu_2Se project, and explained to me what a Fermi level really is. Dr. Alexander Page instructed me on proper synthesis approaches and lab management, introduced me to half-Heusler alloys, inspired me with his computational skills and scientific artwork, and helped me transition to being an independent researcher. It was a joy working with all three of these scientists, and we remain good friends today. Other past members of Professor Uher's group for whom I am grateful include Dr. Junmei Fan, Dr. Si Wang, Pan Ren, Lynn Endicott, and Jennifer Ma.

The staff of the Physics Department at UM are essential for its continued operations. Many of the staff have had a direct positive impact on me while I have been a part of the Ph. D. program, especially Paul Thurmond, Christina Zigulis, Beth Demkowski, Mary Shinn, Lauren Segall, Grace Johnson, Karen O'Donovan, Carol Rabuck, Holly Wanty, Cynthia McNabb, Angela Sands, Joseph Sheldon and Dalton Burton-Curry.

Last, outside of everything physics related, my family and friends have been an incredible source of life. In one way or another, they all helped me maintain a sense of reality on the days when my biggest problems in life were broken thermocouples or anomalous magnetoresistance.

TABLE OF CONTENTS

LIST OF FIGURES

FIGURE

LIST OF TABLES

TABLE

LIST OF ABBREVIATIONS

BSE backscattered electron

BTE Boltzmann transport equation

EDX energy dispersive X-ray spectroscopy

ETO Electrical Transport Option

FC field-cooled

FH full-Heusler

HH half-Heusler

HT high temperature

LT low temperature

PM paramagnons

PM+C paramagnons and spin clusters

PM+M paramagnons and magnons

PPMS Physical Property Measurement System

PXRD powder X-ray diffraction

RT room temperature

RTA relaxation-time approximation

SEM scanning electron microscopy

SIC superionic conductor

TE thermoelectric

TZHNSS $Ti_{0.25}Zr_{0.25}Hf_{0.50}NiFe_xSn_{0.975}Sb_{0.025}$

UM University of Michigan

VSM Vibrating Sample Magnetometer

WAL weak anti-localization

ZFC zero-field-cooled

ABSTRACT

Vast amounts of heat are emitted by industrial factories, automobiles and geologic formations. To convert the abundance of heat into usable electricity, stable thermoelectric materials with high conversion efficiencies (or equivalently, large zT values) are essential. In this thesis, I first focus on a superionic conductor, Cu_2Se, that is an excellent thermoelectric material, yet known to have dissociation issues in real application conditions. By doping the structure with Sn, I was able to demonstrate improved zT values and increased chemical stability. I describe the homebuilt current stress test that I implemented for emulating a high-temperature power generation setting, which has now become more common in thermoelectric studies of Cu_2Se-based materials.

In a second project, I formed part of a team that showed that magnetic dopants can augment the thermoelectric conversion efficiencies in a half-Heusler alloy, (Ti, Zr, Hf)NiSn. Here, I detail my study of the low-temperature magnetic properties of the composite materials, including the cluster-glass behavior that is visible in the bifurcation of the zero-field-cooled and field-cooled temperature-dependent magnetic susceptibility. I applied the AC susceptibility technique to witness the evolution of the cluster-glass freezing temperatures as a function of driving frequency and strength of the applied magnetic field. The extensive magnetic characterization is important for the recent acceleration of research on magnetic compounds within the thermoelectrics community.

I further discovered that the same half-Heusler composites exhibit a strongly non-monotonic dependence of the heat capacity on applied magnetic field at temperatures below 10 K. In the final project of this thesis, I describe the fitting of multi-level paramagnon and volumetric magnon models to the heat capacity data. Using statistical analysis tools, I show that the two-level paramagnon effect on the heat capacity is the most significant, and could be due to trace impurities or defects within the highly disordered compounds. The Fe-added samples exhibit a unique trend of the heat

capacity with magnetic field at temperatures lower than 4 K. I derive a magnon model as a possible explanation, yet it overfits the data. In the end, I qualitatively attribute the lowest temperature effect in the Fe-added samples to a magnetotransport effect observed in the second project.

Overall, the thesis is primarily motivated by thermoelectrics research, which is seen most directly in the high-temperature thermoelectric property study of Cu_2Se. The magnetic half-Heusler alloys that were shown to possess improved thermoelectric properties at high temperatures are then studied for their magnetic properties, magnetotransport and magnetothermodynamics at low temperatures as a way of discovering more fundamental aspects of the compounds.

CHAPTER 1

Introduction

1.1 Motivation: Thermoelectric Power Generation from Waste Heat

Approximately two-thirds of the world's energy consumption in industrial processes is squandered as waste heat, as highlighted in Figure 1.1 [1]. The smoke stacks of innumerable fossil fuel-burning power stations and steel mills, as well as the exhaust from the tailpipes of more than a billion automobiles worldwide, are primary examples of rejected heat. Thermoelectric (TE) materials, which can convert heat directly into electricity, have great potential to harvest waste heat and thereby curtail the global dependence on fossil fuels and reduce harmful emissions into the atmosphere. To be economically viable, TEs must possess high conversion efficiency, represented by the dimensionless TE figure of merit

$$zT = \frac{S^2\sigma}{\kappa_T}T = \frac{PFT}{\kappa_e + \kappa_L}, \tag{1.1}$$

with S the Seebeck coefficient, σ the electrical conductivity, $PF = S^2\sigma$ the "power factor", T the absolute temperature, and $\kappa_T = \kappa_e + \kappa_L$ the total thermal conductivity split into its two main constituents: the electronic contribution, κ_e, and the lattice contribution, κ_L. A derivation of Eq. 1.1 can be found in Ref. [2], wherein a proper accounting of the heat flow and power output of a TE device (Figure 1.2(a)) is made.

For real-world applications, the corresponding device efficiency for a given zT is expressed as

$$\eta = \frac{T_H - T_C}{T_H}\left(\frac{\sqrt{1+zT}-1}{\sqrt{1+zT}+\frac{T_C}{T_H}}\right) = \eta_C\left(\frac{\sqrt{1+zT}-1}{\sqrt{1+zT}+\frac{T_C}{T_H}}\right). \tag{1.2}$$

Here, T_H is the hot side of the TE device, T_C is the cold side, and η_C is the Carnot efficiency, the maximum allowable conversion efficiency of a heat engine. As $zT \to \infty$, $\eta \to \eta_C$. A plot

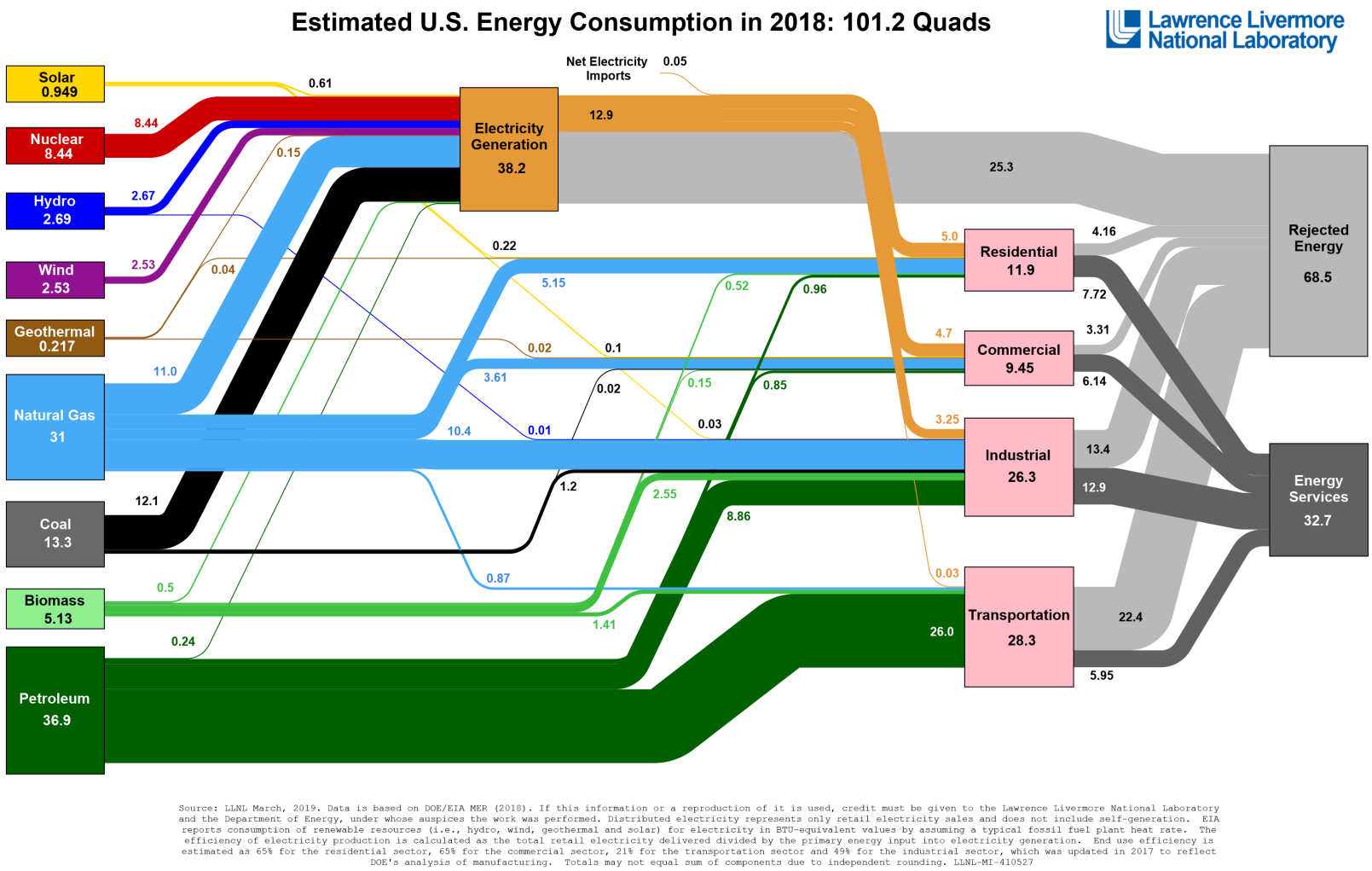

Figure 1.1: **Total energy sources and uses within the United States in 2018.** Taken from Ref. [1]. Units are given in "quads", or quadrillion BTUs (British thermal units). There are approximately four BTUs in the more common "food" calorie. The consumption of 101.2 quads of energy in 2018 in the United States amounts to a 2000 "food" calorie daily diet for around 35 billion people. The population of the United States is near 330 million.

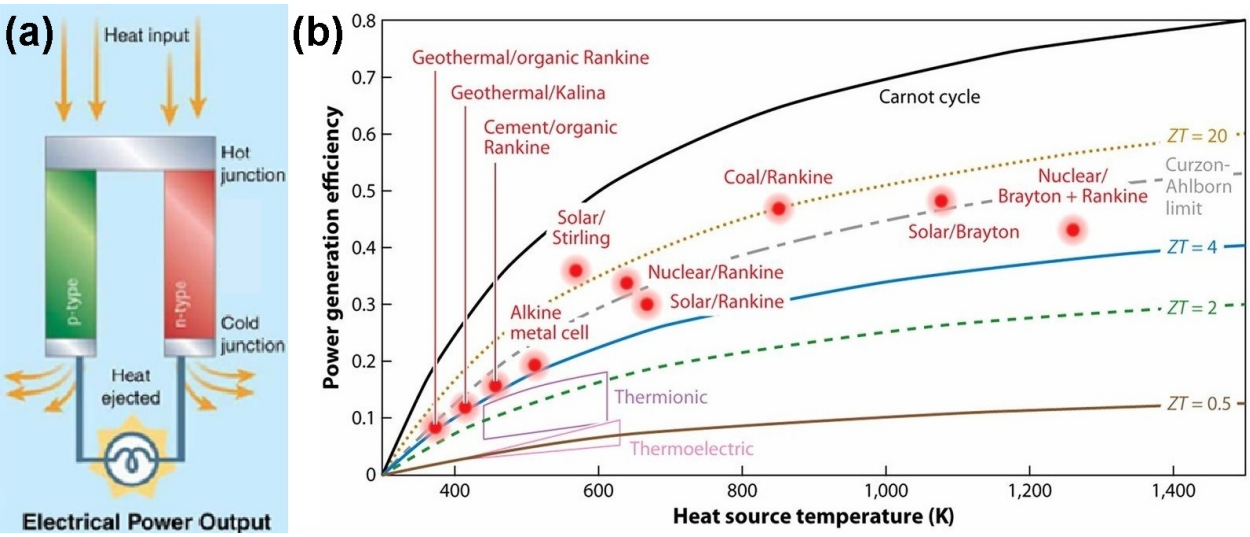

Figure 1.2: **Thermocouple schematic and comparison of various thermodynamic cycles.** (a) Thermoelectric (TE) device [4] consisting of two semiconducting legs, one in which electrons are the dominant charge carrier (n-type) and the other p-type, where the oppositely charged "holes" are the majority carriers. The incident heat energy is converted into output electrical power by the Seebeck effect, as described further in Section 1.2.1. (b) Comparison of the efficiency, $\eta(T_H; T_C = 300\text{ K})$, of various thermodynamic cycles, with the solid black line the Carnot limit. Four different zT values of 0.5 (solid brown line), 2 (dashed green line), 4 (solid blue line) and 20 (dotted gold line) scale from the lowest values in the plot to increasingly higher ones. The grey dotted-dashed line in the middle is the Curzon-Ahlborn limit, the maximum efficiency of a heat engine affected by irreversible finite heat transfer rates. Modified from Ref. [5] with permission from Annual Reviews.

of the device conversion efficiencies against zT is given in Fig. 1.2(b) for an ambient cold side temperature ($T_C \approx 300$ K). $zT \approx 1$ has served as a historical standard for critical, yet niche, applications [3], such as providing the onboard power for deep space missions like Voyager, Pioneer, and others.

Realistically, zT values > 2 and beyond (device conversion efficiencies around 20%) are necessary for broad implementation of TE waste heat recovery from factories, automobiles, and even the human body [6]. Recent reviews by Tan *et al.* [7], Han *et al.* [8], Shi *et al.* [9], and He and Tritt [10] compile the most promising TE material families and the strategies used to optimize their zT values. During the past decade, several classes of TEs have been identified and engineered to attain values of $zT > 2$. We plot the temperature dependence of zT for select materials in Figure 1.3.

The heat engine perspective of a TE device can be run in the opposite direction, i.e. an electrical current can be input into a thermocouple to drive a temperature gradient. Typical applications of TE coolers include temperature management of optical systems, on-chip cooling of semiconductor

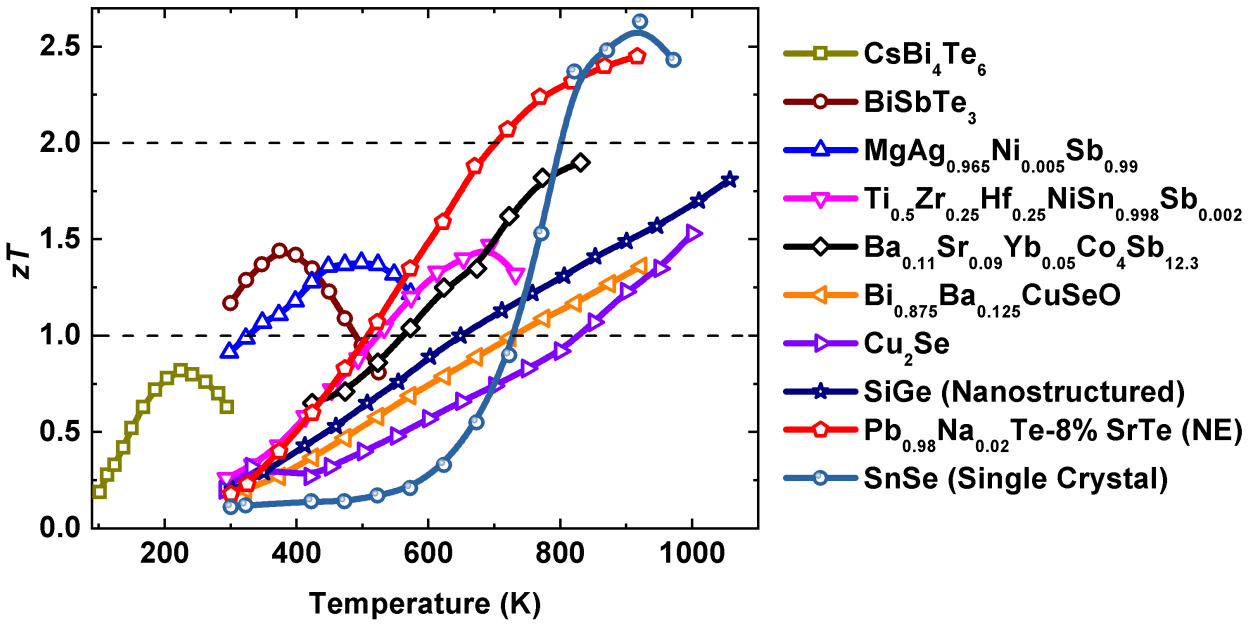

Figure 1.3: **Temperature-dependent thermoelectric figure of merit, zT, for a number of highly researched materials.** The materials include $CsBi_4Te_6$ [11], $BiSbTe_3$ [12], $MgAg_{0.965}Ni_{0.005}Sb_{0.99}$ [13], $Ti_{0.5}Zr_{0.25}Hf_{0.25}NiSb_{0.998}Sn_{0.002}$ [14], $Ba_{0.11}Sr_{0.09}Yb_{0.05}Co_4Sb_{12.3}$ [15], $Bi_{0.875}Ba_{0.125}CuSeO$ [16], Cu_2Se [17], SiGe [18], $Pb_{0.98}Na_{0.02}$Te-8% SrTe [19], and SnSe [20].

devices, and electronic refrigeration of biological substances. TE cooling will not be mentioned much more herein since the TE aspects of the thesis focus on the high-temperature ($>$ 600 K) conversion of heat into electricity. However, the interested reader may consult Ref. [21].

Since the goal of TE research is to increase zT as much as possible for higher device conversion efficiencies (within economic and environmental restraints, of course), it is essential to ask whether condensed matter physics places a fundamental upper bound on zT. To start, we can consider the charge carrier concentration, n, or how many conduction electrons (or the positively charged equivalent "holes") are present per cm^3 in a material. n is one of the most readily tunable aspects of solids, so $zT(n)$ has a direct connection with real-world TE performance. Later, in Section 2.2, we will derive expressions for n, S, σ and κ_e that can be used to assess $zT(n)$, which is plotted in Figure 1.4.

Evidently, the peak that occurs in the numerator of zT as a function of carrier concentration yields an upper bound for zT at a specific value of n_{opt}. Typical values for n_{opt} range from 10^{19} to 10^{20} cm^{-3}, characteristic of highly doped (degenerate) semiconductors. As a result, most of TE research focuses on semiconducting materials, normally with electronic energy band gaps $\lessapprox 1$ eV, which is borne out in the list of materials shown in Fig. 1.3. From Fig. 1.4, we understand that one of the optimization steps in maximizing zT in candidate TE materials is to determine

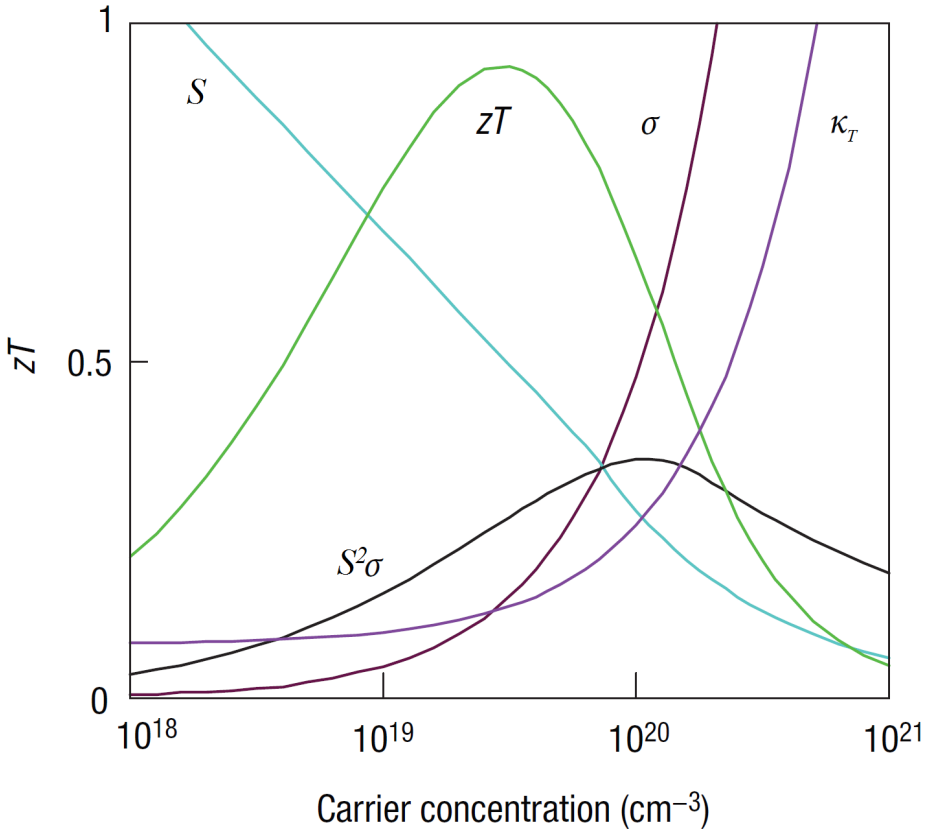

Figure 1.4: **Thermoelectric properties as a function of charge carrier concentration.** The thermoelectric figure of merit, zT, the Seebeck coefficient, S, the electrical conductivity, σ, the power factor, $S^2\sigma$, and the total thermal conductivity, κ_T, are shown as light green, cyan, maroon, black, and light purple solid lines, respectively. The plot demonstrates that fundamental solid-state physics places an upper bound on $S^2\sigma$ that is reflected in a maximum for zT. Modified from Ref. [22], with permission from Nature Publishing Group.

the appropriate n_{opt} through elemental doping, for example. Another approach is to consider that the lattice contribution to the thermal conductivity, κ_L, is decoupled from n. Therefore, carefully selecting and engineering materials with low values of κ_L, usually $\lessapprox 1$ $\mathrm{Wm^{-1}K^{-1}}$, can lead to exceptional zT. Although these are not the only guiding principles of TE research, as outlined in Refs. [7, 8, 9, 10], they are the primary motivations for the TE research presented in Chapters 3 and 4.

1.2 Thermoelectric Phenomena

From Section 1.1, it is clear that TE power generation could be an effective way of utilizing waste heat as long as zT values can be substantially enhanced within economic and environmental constraints. In the current section, we will describe the underlying physical phenomena for TE power

generation (the Seebeck effect) and cooling (the Peltier effect), as well as an important electronic effect in the presence of applied magnetic field, that is, the Hall effect.

1.2.1 Seebeck and Peltier Effects

The joining of two wires of dissimilar metals at a common point, typically called a junction, results in a device known as a thermocouple. Heating the junction creates a non-zero potential difference between the end-points of the open loop, a phenomenon known as the Seebeck effect [2]. If the open loop were closed, an electrical current would circulate within the thermocouple as long as the temperature gradient, ΔT, between the two closed ends remained, as in Fig. 1.2(a). The corresponding voltage, ΔV, driving the current is found experimentally to be

$$\Delta V = S\Delta T, \tag{1.3}$$

where S is the previously mentioned Seebeck coefficient. Rigorous mathematical formulae for the Seebeck coefficient within the framework of the Boltzmann transport equation (BTE) will be derived in Section 2.2. The units of S are V K^{-1}, with most semiconductors for TE applications possessing magnitudes of the Seebeck coefficient from 50 to 300 μV K^{-1} [23].

Viewed in another sense, the electronic charge carriers within the metallic legs of the thermocouple thermally diffuse from the hot junction to the cold. Because the electronic energies of the two separate metals are not equivalent, there is a corresponding potential difference between the hot and cold ends. Possibly more intuitive is the construction of a thermocouple in which one of the legs is an n-type semiconductor, where electrons are the charge "fluid" and the Seebeck coefficient is negative, while the other thermocouple leg is a p-type semiconductor, where the motion of the holes sets the direction of the electrical current and the Seebeck coefficient is positive. In such a case, Fig. 1.2(a), the electrons and holes counter-propagate within the circuit, setting up a counter-clockwise current. The direction of the current would of course be opposite if the two legs were switched.

Starting with the open loop thermocouple again, but with the hot and cold ends at the same temperature initially, a current driven through the junction will cause a local heating or cooling, called the Peltier effect. The physical basis for the heating or cooling is the emission or absorption of energy by the charge carriers as they pass between the two dissimilar metals at the junction. Phenomenologically, the heat, Q, liberated or absorbed at the junction scales linearly with the input current, I:

$$Q = \Pi I, \tag{1.4}$$

with Π the so-called Peltier coefficient. The Peltier effect is the basis for TE cooling. It is generally

more challenging to detect since the driving current also gives rise to Joule heating. Comparing the junction temperature for opposing current directions, in which the Joule heating would be identical yet the Peltier effect would be opposite, is one way of isolating the Peltier signal.

1.2.2 Hall Effect

Due to the Lorentz force, charge carriers in motion feel the presence of a local magnetic field slanted away from the direction of current [24]. The force, $\vec{F_L} = q\vec{\xi} \times \vec{H}$, is perpendicular to both the velocity of the charge carriers, $\vec{\xi}$, and the applied magnetic field, $\vec{H}$. $q = -e$ for electrons and $+e$ for holes, where $e \approx 1.6$ x 10^{-19} C is the elementary charge. The motion is pictured for an electron in a rectangular bar of an n-type material in Figure 1.5. As the electrons pile up on one side of the bar, a measurable potential difference develops between the opposite edges. This phenomenon is known as the Hall effect, with V_H the Hall voltage. The corresponding Hall coefficient is defined as

$$R_H \equiv \frac{E_H}{jH} = \frac{V_H/w}{IH/tw} = t\frac{V_H}{IH}, \tag{1.5}$$

where E_H is the magnitude of the electric field associated with the Hall voltage, j is the current density used to excite the electronic motion along the $\hat{x}$ direction in Fig. 1.5, and t and w are the labeled sample dimensions. The last expression in Eq. 1.5 is the most experimentally useful since voltages and excitation currents are more readily accessible than electric fields and current densities. Typical values of R_H start at $\approx 10^{-3}$ cm^3 C^{-1} for highly degenerate semiconductors, which can be quite difficult to measure experimentally. Less heavily doped, intrinsic semiconductors can have values of R_H closer to 10^1 cm^3 C^{-1} that are quite stable during measurement [23].

At steady state with a constant magnetic field along the $\hat{z}$ direction and electrical current only along $\hat{x}$, the build-up of charge carriers on the side of the sample prevents further accumulation through the opposing Hall field. Considering the corresponding forces acting on the charge carriers, we can set their sum in the $\hat{y}$ direction to be zero:

$$\sum_i F_{i,y} = F_{e,y} + F_{L,y} = q(E_H - \xi_x H) = 0. \tag{1.6}$$

Thus, $E_H = \xi_x H$ can be plugged into the definition of R_H in Eq. 1.5 to yield

$$R_H = \frac{\xi_x}{j} = \frac{1}{nq}, \tag{1.7}$$

where $j = nq\xi_x$, and n is the charge carrier density mentioned in Section 1.1. Because q is the opposite sign for electrons and holes, the Hall coefficient is one way of identifying whether a semiconductor is dominantly n-type or p-type, respectively. This is experimentally borne out in

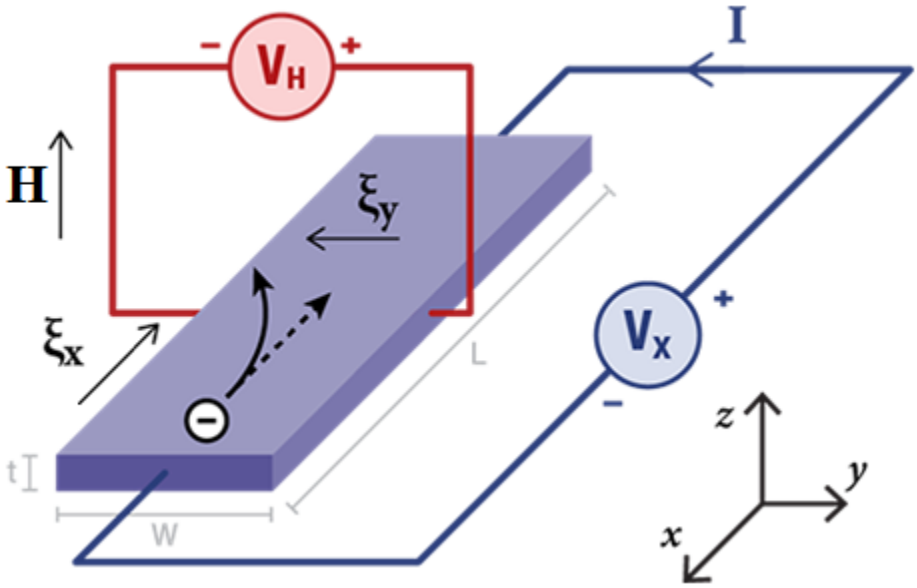

Figure 1.5: **Schematic of the Hall effect for a rectangular solid.** The bar has dimensions w x t x L. A current, I, driven by an excitation voltage, V_x, runs parallel to the long axis of the bar in the $\hat{x}$ direction. At the same time, a magnetic field, H, is directed along $\hat{z}$. The resultant Lorentz force diverts the ξ_x velocity of the electrons to the $-\hat{y}$ direction, setting up the Hall voltage, V_H [25].

the fact that the measured Hall voltage is positive for p-type materials and negative for n-type, due to the charge carriers accumulating on the identical side of the sample regardless of sign. Also, because R_H is a simple constant in Eq. 1.7, V_H scales linearly with the applied magnetic field by Eq. 1.5. Any non-linear V_H vs. H behavior would suggest a different physical picture than the one described above.

Another critically important aspect of Eq. 1.7 is that the experimentally measurable Hall coefficient is directly related to the charge carrier concentration. As demonstrated in Fig. 1.4, $zT(n)$ is maximized at a certain $n = n_{opt}$ that enhances TE performance. Measuring the Hall effect is therefore a key tool for TE research. For example, knowing n for a given TE material and conducting a doping study to alter the charge carrier concentration with insight from the Hall effect measurement, is one approach for optimizing zT. Highly doped semiconductors can have $n \gtrapprox 10^{20}$ cm^{-3}, whereas more intrinsic semiconductors possess values of $n \lessapprox 10^{18}$ cm^{-3} [2, 22].

Furthermore, combining the Hall coefficient with the electrical conductivity, σ, determines the charge carrier mobility, μ, in the following manner:

$$\mu = \frac{\sigma}{ne} = \sigma|R_H|. \tag{1.8}$$

The charge carrier mobility is a measure of how easily charge carriers move through a material when driven by an electric field. Normal TE materials maintain mobilities of $\approx$ 30 to 200 cm^2 V^{-1} s^{-1} [23]. In general, charge carriers can encounter other charge carriers, ionized impurities,

lattice vibrations, grain boundaries, etc. in their path. The form of scattering that dominates the conduction influences the temperature dependences and magnitudes of σ, S and zT, as to be discussed in Section 2.2. To determine the main source of scattering, $\mu(T)$ is required [26]. Both $R_H(T)$ and $\sigma(T)$ are therefore needed. Yet again, we see that measuring the Hall effect, specifically as a function of temperature, is critical for optimizing TE performance, in this case by providing insight into the charge carrier scattering mechanisms.

The above equations (1.6 - 1.8) assume the overwhelming presence of a single charge carrier type with a single charge carrier mobility. In semiconductors and composite materials, there can be multiple charge carriers (electrons and holes) present simultaneously with distinct mobilities and carrier concentrations that complicate the analysis. For example, in a two-carrier system, the electrical conductivity becomes the sum of the individual conductivities, $\sigma = |q|(n_1\mu_1 + n_2\mu_2)$, and the Hall coefficient is then

$$R_H = \frac{\sigma_1^2 R_{H,1} + \sigma_2^2 R_{H,2}}{(\sigma_1 + \sigma_2)^2} = \frac{1}{|q|}\frac{n_2\mu_2^2 - n_1\mu_1^2}{(n_2\mu_2 + n_1\mu_1)^2}. \tag{1.9}$$

Because of the weighting of the individual Hall coefficients, the Hall voltage response to magnetic field can in general be non-linear in the two-carrier system, as detailed thoroughly in Ref. [27]. In such a scenario, the individual charge carrier concentrations and mobilities can be extracted by studying the magnetic field-dependent electrical conductivities and Hall voltages. Chapters 3 and 4 of the thesis contain Hall effect measurement data that is analyzed simply with Eqs. 1.7 and 1.8 because the Hall voltage was linear with respect to the applied magnetic field.

1.3 Classical Magnetic Phenomena

Chapters 4 and 5 involve many aspects of classical magnetism, such as diamagnetism, paramagnetism and ferromagnetism, in addition to more recently discovered forms of magnetism, like cluster glass freezing. Therefore, the following sections describe the classical magnetic phenomena in greater detail to promote ease of understanding in the later chapters. Much of the discussion here follows the works of Ashcroft and Mermin [24], Kittel [28] and Hurd [29].

1.3.1 Fundamental Definitions

Discrete magnetic moments in a solid are associated with the electron spins of the constituent ions. The moments can be induced by the presence of an applied magnetic field, as in diamagnetism and paramagnetism, or they can spontaneously arise from inter-moment coupling, as in ferromagnetism and anti-ferromagnetism.

For characterization purposes, we define the magnetization of an equilibrium system at temperature T in a magnetic field of strength H as

$$M(H,T) \equiv \sum_i m_i(H,T) = -\frac{\partial F(H,T)}{\partial H}, \tag{1.10}$$

where F is the thermodynamic free energy, and the directions of the applied magnetic field and magnetic moment are assumed to be parallel [24]. Each magnetic moment i of strength m_i contributes to the overall magnetization. Typical measurement units for the magnetic moment are known as "emu", or electromagnetic unit, which is equivalent to one-thousandth of an Ampere m^2. The applied field strength is often measured in Tesla (T) or Oersted (Oe), with 1 T = 10 kOe in vacuum. Strongly magnetic materials can exhibit magnetizations of several 10^{-1} emu g^{-1}, when normalized to the sample mass. On the contrary, very weak magnetic materials possess values closer to 10^{-5} emu g^{-1}.

How easily the magnetization is affected by the magnetic field is described by the magnetic susceptibility,

$$\chi \equiv \frac{\partial M}{\partial H}. \tag{1.11}$$

With these definitions in place, we can now briefly detail the classical forms of magnetism.

1.3.2 Diamagnetism

For ions with completely filled electronic shells, the lowest energy (ground) state of the system has zero spin and orbital angular momentum. An applied magnetic field then only affects the total kinetic energy of the electrons via a vector potential, resulting in Larmor/Langevin diamagnetism with

$$\chi_{dia} \propto -e^2 n_I \Big\langle 0 \Big| \sum_i r_i^2 \Big| 0 \Big\rangle, \tag{1.12}$$

where n_I is the ion density and the bracketed term represents the expectation value of the electronic positions in the ground state. Two key features of the diamagnetic susceptibility are that it is negative and temperature independent. The magnitudes of χ_{dia} are typically around 10^{-5} in units of cm^3 per mole. An intuitive way of understanding diamagnetism is that the motion of the electrons around the nuclei represents an internal magnetic field. In the presence of an applied magnetic field, the electrons react to oppose $\vec{H}$ and find a lower energy state, similar to Lenz's law for electrical circuits.

1.3.3 Paramagnetism

For ions with incompletely filled d- or f-electron shells, the interaction of the magnetic field with the non-zero spin and orbital angular momentum significantly changes the free energy. The energy of the interaction between the total angular momentum of the ion, $\vec{J}$, and the pervading magnetic field is given as

$$E_{ion} = -g\mu_B \vec{J} \cdot \vec{H}, \tag{1.13}$$

a coupling that favors alignment of the free spin with $\vec{H}$. In Eq. 1.13, g is the unitless Landé g-factor (also known as the spectroscopic splitting factor) that is approximately 2 for electrons. $\mu_B = 9.274$ x 10^{-24} Joules per Tesla is the Bohr magneton. For the total angular momentum, J, the allowed states can span $-J$, $-J+1$, ..., $J-1$, J for a total of $2J+1$ states. This has a direct impact on the free energy, yielding an overall magnetization of

$$M_{para} = n_I g\mu_B J B_J(g\mu_B JH/k_B T), \tag{1.14}$$

where $B_J(x)$ is the Brillouin function defined as

$$B_J(x) = \frac{2J+1}{2J}\coth\left(\frac{2J+1}{2J}x\right) - \frac{1}{2J}\coth\left(\frac{x}{2J}\right). \tag{1.15}$$

Again, Eq. 1.14 assumes that $\vec{J}$ and $\vec{H}$ are parallel, or that their dot product has value JH [24]. $B_J(x)$ is plotted in Figure 1.6(a) for several pertinent values of J.

From Eq. 1.13, we already know that $\chi_{para} > 0$ since $\vec{M}$ will follow $\vec{H}$. The positivity of $\partial B_J(x)/\partial x$ for all x and $J \neq 0$ (Figure 1.6(a) and Section 1.4.3) is further confirmation. Indeed, in the low-field, high-temperature (HT) limit, i.e. $x = g\mu_B JH/k_B T \ll 1$, $B_J(x) \approx x(J+1)/3J + O(x^3)$, giving a magnetic susceptibility following the Curie Law

$$\chi_{para} \propto (g\mu_B)^2 \frac{J(J+1)}{k_B T}. \tag{1.16}$$

The $1/T$ dependence of χ_{para} is a defining experimental signature of paramagnetism. In general, the magnitudes of χ_{para} are normally of order 10^{-2} to 10^{-3} cm^3 per mole, 100 to 1000 times larger than the diamagnetic component, Eq. 1.12. Notably, the magnetic moments themselves are constantly changing orientation as a function of time, based on their thermal energy, so any experimental probe with frequencies $\lesssim 10$ kHz measures the time-averaged magnetization [30].

To be clear, the "Langevin" paramagnetism outlined above stems from the localized electrons surrounding ions with $J \neq 0$. For $J = 0$, which occurs in electron shells that are one electron short of being half full, a second-order perturbative effect termed Van Vleck paramagnetism is

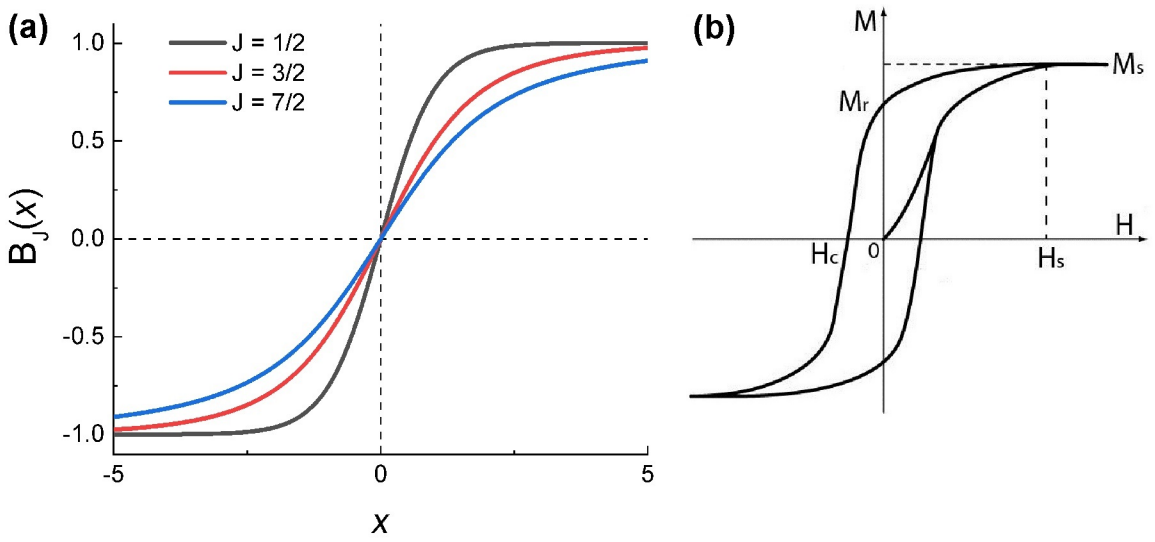

Figure 1.6: **Magnetization of paramagnetic and ferromagnetic systems.** (a) The Brillouin Function, $B_J(x)$, that governs the magnetization of paramagnetic systems as a function of applied field. Here, the independent variable is the unitless $x = g\mu_B JH/k_BT$. The three different values of J represent unique total angular momenta of the paramagnetic ions. (b) "Hysteresis loop" characteristic of ferromagnetic materials initially at zero magnetization then magnetized to high positive and negative fields [31]. M_s, H_s, M_r, and H_c are, respectively, the saturation magnetization, saturation field, remanent magnetization and coercive field described in the text.

present [24, 28, 29]. Furthermore, conduction electrons in metals interact with magnetic fields as a delocalized two-level system. This so-called Pauli paramagnetism, as well as the Van Vleck paramagnetism, are both nearly temperature independent and similar in magnitude to diamagnetism, i.e. 100-1000 times weaker than Langevin paramagnetism.

1.3.4 Ferromagnetism

In many materials, there is some form of interaction between the spins, known as exchange coupling, that results in spontaneous magnetic ordering below some temperature. Given an array of spins in a particular configuration, the total interaction energy in the Heisenberg model is given as

$$E_{exc} = -\frac{1}{2}\sum_j \sum_{i\neq j} J_{ij}\vec{S}_i \cdot \vec{S}_j, \tag{1.17}$$

where J_{ij} is the exchange constant between spins i and j. $J_{ij} > 0$ is a ferromagnetic interaction in which the coupled spins align in the same direction. The corresponding ordering temperature is known as the Curie temperature, T_C. Ferromagnetic phases transition to paramagnetic as T surpasses T_C from the low side. The susceptibility of the associated paramagnetic phase remains the same as Eq. 1.16, but with $T \rightarrow T - T_C$, known as the Curie-Weiss Law. On the other

hand, $J_{ij} < 0$ represents an anti-ferromagnetic interaction in which the coupled spins oppose each other's directions. The ordering temperature in this case is known as the Néel temperature, T_N. The Curie-Weiss Law for anti-ferromagnetic phases is again Eq. 1.16, but with $T \rightarrow T - T_N$

Short-range magnetic order occurs in the case of "direct exchange", where the magnetic moments are sufficiently close to each other such that their wave functions overlap. "Indirect exchange" can couple moments over longer distances by acting through an intermediary. In the case of metals and degenerate semiconductors that are of interest to TE research, the intermediary is often itinerant (conduction) electrons. This particular interaction is known as RKKY coupling for co-discoverers Ruderman, Kittel, Kasuya, and Yosida [32, 33, 34]. $J_{RKKY}(\vec{r}_{ij})$ is an oscillatory function of the spin separation vector $\vec{r}_{ij}$, creating spatial regions of ferromagnetic and anti-ferromagnetic interaction. The combination leads itself naturally to the concept of magnetic frustration to be discussed in Chapter 4.

Much theoretical work has been done in analyzing Eq. 1.17 to understand the ground state and excited states that satisfy the Heisenberg model, and their associated physical characteristics. In short, ferromagnetism in the one- and two-dimensional Heisenberg model exists only at zero temperature, while excited states are possible in three dimensions, by the Mermin-Wagner theorem [35]. Tractable solutions to Eq. 1.17 involve first simplifying the model by selecting out a single direction for the spin (the so-called Ising model) and narrowing the sums to include only nearest neighbors. The exact solution to the 1D Ising model demonstrates that $M = 0$ for $H = 0$, i.e. no spontaneous magnetization. However, for 2D, Onsager's solution exhibits $M \neq 0$ for $H = 0$ for a number of lattices [36]. The spontaneous magnetization in this case is not in conflict with the Mermin-Wagner theorem since the solution is not found in the full 2D Heisenberg model. Currently, no solution exists for the 3D Ising model, but computational simulations can be implemented to understand some of its properties.

In real ferromagnetic materials, either polycrystalline or single crystalline, the magnetic moments are not uniformly aligned throughout the bulk in the absence of an external magnetic field, even with $T < T_C$. Ferromagnets split into microscopic, internally aligned domains because the energy of macroscopic magnetism ($\propto VM^2$, with V the volume) outweighs the interaction energy of Eq. 1.17. A body divided into randomly directed domains of locally aligned moments lowers the associated magnetic energy while sacrificing only a small amount of exchange energy gained by the unfavorable neighboring interactions at the domain boundaries.

The internal moments of a ferromagnetic material can be sufficiently randomized by elevating the temperature to above T_C and allowing the material to cool without applying any magnetic fields. The magnitude of the magnetization will be near its minimum, $M \approx 0$, after such a procedure. If a magnetic field is then ramped up with $T < T_C$, the ferromagnetic moments will align with the field, achieve a saturation magnetization, M_s, at H_s and hold onto a remanent magnetization, M_r,

once the applied field is returned to zero. The spontaneous moments result in a "hysteresis loop" of the magnetization plotted against applied magnetic field as H is swept from 0 to $H > H_s$, then to a symmetrically negative magnitude field and finally back to zero. The magnetic field required to bring the magnetization back to zero after the initial magnetization procedure is known as the coercive field, H_c. A typical hysteresis loop is pictured in Fig. 1.6(b) and is one of the primary indications of ferromagnetism in experimental studies.

Considering the exchange coupling as an internal field that forces spin alignment, we can make an approximation of the magnitude of the field by $k_B T_C = \mu_B H_{int}$. With pure iron as an example, $T_C \approx 1043$ K yields $H_{int} \approx 10^3$ Tesla. For comparison, the magnetic field that guides compasses on Earth is < 1 x 10^{-4} Tesla, 7 orders of magnitude smaller.

1.4 Heat Capacity

The heat capacity of matter in any state (gas, liquid, solid, plasma, etc.) is the amount of energy required to raise a specific volume of the matter by one degree Kelvin. The heat capacity is often given in per mass or per volume units for an easier comparison between materials, and then is called the "specific heat". Experimental studies typically report specific heat data, like that which we present in Chapter 5. In the majority of theoretical considerations for solids, the heat capacity at constant volume is the most convenient parameter to derive, with definition

$$C_V \equiv \left.\frac{\partial U}{\partial T}\right|_V . \tag{1.18}$$

Experimentally, the heat capacity of solids at constant pressure, C_p, is most frequently measured since changing the temperature affects the volume. However, C_p is very close in value to C_V in most three-dimensional cases besides very high temperatures ($T \gtrapprox 500$ K). In the low temperature (LT) studies detailed in Chapter 5, we will apply the theoretical C_V models to the experimentally measured C_p data.

The heat capacity of solids stems mainly from (1) the atomic motion of a crystal structure's constituent elements, (2) the electrons of the individual atoms, and (3) discrete energy levels of the atoms and electrons that become depopulated at temperatures $\lessapprox 10$ K. In the following sections, we derive the full form of C_V for the three different sources, as well as the appropriate limits at low and high temperatures that will be useful in Chapter 5. In essence, we recast the parts of Refs. [24, 28, 37] that are relevant to the heat capacity studies in this thesis.

1.4.1 Lattice Vibrations

At finite temperature, the atoms occupying the lattice sites oscillate around their equilibrium position due to the competition between the thermal energy and the chemical energy of the bonds holding the crystal structure together. The periodicity of the lattice results in cooperative behavior manifested as regular modulation of the atomic position throughout the crystal structure. Such "waves", or "lattice vibrations", are known as "phonons" in the particulate description. Based on the stiffness of the chemical bonds and the geometric arrangement of the atoms in space, the effective energy of the lattice vibrations can be derived. For small displacements around the equilibrium positions, the potential energy scales quadratically with the displacement, known as the "harmonic approximation".

We start by considering a generic form of the total energy of all phonons in a solid:

$$U_{latt} = \sum_{P} \int d\omega D_P(\omega) \frac{\hbar\omega}{\exp\left(\hbar\omega/k_B T\right) - 1}. \tag{1.19}$$

Here, $D_P(\omega)$ is the number of phonon modes with frequency between ω and $\omega + d\omega$, also known as the density of states, for each polarization type, P. Considering a cubic structure in reciprocal space, there is one allowed momentum state per volume $(2\pi/L)^3 = 8\pi^3/V$, where $V = L^3$ is the real-space volume of the primitive cell of length L. Thus, the number of modes within a momentum space sphere of radius k is $N = (V/8\pi^3)(4\pi k^3/3) = Vk^3/6\pi^2$. The density of states for each polarization type is then

$$D_P(\omega) = \frac{dN}{d\omega} = \frac{Vk^2}{2\pi^2}\frac{dk}{d\omega}. \tag{1.20}$$

For three-dimensional solids, one of the most successful models of lattice vibrations is from Debye [38]. Motivated by continuum mechanics, Debye posited that the phonon frequency scales with its momentum, k, and velocity, v_s, i.e. $\omega = v_s k$. Furthermore, each polarization has the same speed of sound, and there is one phonon mode per primitive cell for each polarization type. With $n_D = N/V$ the total number of phonon modes per real-space volume per P, the largest frequency achievable is the "Debye cutoff frequency":

$$\omega_D^3 = 6\pi^2 v_s^3 n_D. \tag{1.21}$$

Incorporating Eqs. 1.20 and 1.21 into 1.19 yields

$$U_{latt} = \frac{3V}{2\pi^2 v_s^3} \int_0^{\omega_D} \frac{\hbar\omega^3 d\omega}{\exp\left(\hbar\omega/k_B T\right) - 1} = \frac{3Vk_B^4 T^4}{2\pi^2 v_s^3 \hbar^3} \int_0^{x_D} \frac{x^3 dx}{e^x - 1}, \tag{1.22}$$

where the factor of 3 in front accounts for the two transverse and one longitudinal polarizations. In the second equality, the substitution of the dimensionless $x = \hbar\omega/k_B T$ was made to remove the

dimensionality of the integral. By differentiating the middle term in Eq. 1.22, the corresponding heat capacity from Eq. 1.18 becomes

$$C_{V,latt} = \frac{3V}{2\pi^2 v_s^3}\int_0^{\omega_D} \frac{\hbar\omega^3(\hbar\omega/k_BT^2)\exp(\hbar\omega/k_BT)}{[\exp(\hbar\omega/k_BT)-1]^2}d\omega = \frac{3Vk_B^4T^3}{2\pi^2 v_s^3\hbar^3}\int_0^{x_D}\frac{x^4e^x dx}{(e^x-1)^2}. \quad (1.23)$$

By scaling the dimensionless x_D by temperature, we can define a characteristic "Debye temperature" as $\theta_D = x_D T = \hbar\omega_D/k_B = \hbar v_s(6\pi^2 n_D)^{1/3}/k_B$. $C_{V,latt}$ becomes the more compact

$$C_{V,latt} = \frac{3k_B^4T^3}{2\pi^2 v_s^3\hbar^3}\left(\frac{\hbar v_s}{k_B\theta_D}\right)^3 6\pi^2 N\int_0^{x_D}\frac{x^4e^x dx}{(e^x-1)^2} = 9Nk_B\left(\frac{T}{\theta_D}\right)^3\int_0^{x_D}\frac{x^4e^x dx}{(e^x-1)^2}. \quad (1.24)$$

The last expression in 1.24 is the exact one we use in Chapter 5 to determine the Debye temperature from experimental data measured from 2 to 400 K. In the LT limit, $x_D \to \infty$, and the integral yields a constant. This is certain by inspection since the integrand is zero at the origin, contains no singularities on the way to ∞ and is exponentially damped. Thus, $C_{V,latt} = \beta T^3$ for some constant β at low temperatures.

1.4.2 Charge Carriers

A gas of free electrons is a simple model for the conduction electrons that propagate almost independently within semiconductors and metals. Unlike the phonons of the previous section, electrons do not have three polarizations, but their intrinsic spin can take on one of two opposing values. Furthermore, due to the Pauli exclusion principle, the probability distribution of electrons of energy E is given by the Fermi-Dirac function $f(E) = (\exp(E-E_F)/k_BT+1)^{-1}$, where E_F is the highest individual energy of the electron system, known as the Fermi energy. With these considerations in mind, the electron equivalent of U_{latt} in Eq. 1.19 is given by

$$U_{elec} = \int dE \frac{ED(E)}{\exp[(E-E_F)/k_BT]+1}. \quad (1.25)$$

The dispersion relation for electrons is also distinct from phonons. In particular, $E = \hbar k^2/2m^*$, where m^* is the effective mass of the electrons. The density of states

$$D(E) = \frac{Vk^2}{\pi^2}\frac{dk}{dE} = \frac{V}{2\pi^2}\left(\frac{2m^*}{\hbar^2}\right)^{3/2}E^{1/2} \quad (1.26)$$

can be substituted into Eq. 1.25 to arrive at

$$U_{elec} = \frac{V}{2\pi^2}\left(\frac{2m^*}{\hbar^2}\right)^{3/2}\int_0^\infty dE\frac{E^{3/2}}{\exp[(E-E_F)/k_BT]+1}. \quad (1.27)$$

By taking the temperature derivative of Fermi-Dirac distribution function in Eq. 1.27, we have the heat capacity $C_{V,elec}$ as

$$C_{V,elec} = \frac{V}{2\pi^2 k_B T^2}\left(\frac{2m^*}{\hbar^2}\right)^{3/2}\int_0^\infty dE \frac{E^{3/2}(E-E_F)\exp\left[(E-E_F)/k_BT\right]}{\left\{\exp\left[(E-E_F)/k_BT\right]+1\right\}^2}. \tag{1.28}$$

For low temperatures, $k_BT \ll E_F$, the appreciable values of the integrand are located right around $E = E_F$. Therefore, we restrict the integration range to $[E_F - k_BT, E_F + k_BT]$ and approximate the integral using the trapezoidal rule to get

$$\begin{aligned} C_{V,elec} &\approx \frac{V}{2\pi^2 k_B T^2}\left(\frac{2m^*}{\hbar^2}\right)^{3/2} k_BT[a(E_F+k_BT)^{3/2}(k_BT) + b(E_F-k_BT)^{3/2}(-k_BT)] \\ &\approx \frac{Vk_B}{2\pi^2}\left(\frac{2m^*E_F}{\hbar^2}\right)^{3/2}\left[a\left(1+\frac{3k_BT}{2E_F}\right) - b\left(1-\frac{3k_BT}{2E_F}\right)\right] \\ &\propto 3k_B^2 T D(E_F)/5. \end{aligned} \tag{1.29}$$

In Eq. 1.29, $a \approx b \approx 1/5$ are two constants from the integrand. The mathematical jump from line 1 of Eq. 1.29 to line 2 utilized the first-order Taylor series of $(1+x)^n \approx 1+nx$ for $x = k_BT/E_F \ll 1$. The trapezoidal method implemented here is more intuitive and simpler than the methods used in Refs. [24, 28] and arrives at the correct dependences but with the coefficient off by a factor of ≈ 5.

Combining Eqs. 1.24 (the contribution of lattice vibrations to the heat capacity) and 1.29, the total heat capacity of a solid in most circumstances at low temperatures ($T \lessapprox 10$ K) can be taken as

$$C_p = \gamma T + \beta T^3. \tag{1.30}$$

In measuring heat capacity experimentally, the data should always first be plotted as C_p/T vs. T^2 to check linearity, with the slope corresponding to β and the y-intercept to γ. Such a scenario is demonstrated in Figure 1.7. Any non-linearity, especially at the lowest temperatures, signals behavior outside the realm of phonons and electrons, which is the focus of the next section.

1.4.3 Discrete Energy Levels

Both electron and nuclear spins have discrete allowed states based on their total angular momentum, J, as discussed in Section 1.3.3. At high enough temperatures, all of the states are equally populated, and the energy associated with the spins does not change appreciably with temperature, yielding essentially zero heat capacity. Conversely, as $T \to 0$ K, the lowest energy state of the spins is the only level populated, and "small" changes in temperature have little impact on the total system energy, again yielding negligible heat capacity. Somewhere in between the two limits,

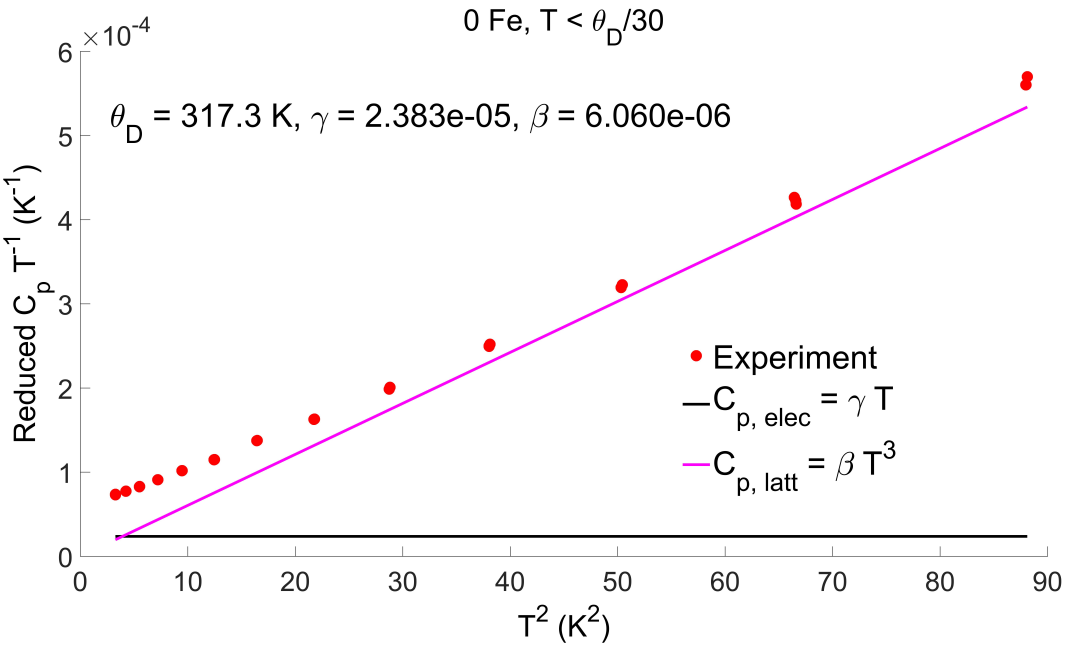

Figure 1.7: **Electron and phonon contributions to the heat capacity.** The experimental data (red circles) is accompanied by the best-fit electron and phonon contributions given by γT (black line) and βT^3 (magenta line), respectively, with the values of γ and β listed in the plot. θ_D is the Debye temperature. The units of γ and β are irrelevant here since C_p has been reduced by a combination of the Boltzmann and Avogadro constants for computational purposes. In agreement with Eqs. 1.24, 1.29, and 1.30, the electron component is constant and the phonon component is linear in the $C_p T^{-1}$ vs. T^2 representation here. The non-linearity of the experimental data at temperatures lower than approximately 4 K indicates that the pure electron and phonon contributions are an insufficient description of the system.

there must be disorder among the energy levels and a positive contribution to the heat capacity. We can estimate the temperatures at which discrete energy levels become relevant by Eq. 1.13. For example, a free conduction electron with spin $\frac{1}{2}$ either up or down exhibits an energy splitting in a magnetic field of 1 Tesla of $T = 2\mu_B/k_B \approx 1$ K. Nuclear magnetic moments are typically about 100 times smaller, so the corresponding temperature splitting in the same 1 Tesla magnetic field would be ≈ 10 mK [37].

We can derive the heat capacity contribution from $2J+1$ discrete energy levels by utilizing Eqs. 1.14 and 1.15, as well as the fact that $U_{para} = -MH$. U_{para} is distinct from E in Eq. 1.13 in that it is a total system energy, not just the moment-field interaction. Accordingly,

$$\begin{aligned} C_{V,para} &= n_I g \mu_B J H \frac{dB_J(g\mu_B JH/k_BT)}{dT} \\ &= -\frac{n_I g^2 \mu_B^2 H^2}{4k_B T^2}\left[(2J+1)^2 \text{csch}^2\left(\frac{(2J+1)g\mu_B H}{2k_B T}\right) - \text{csch}^2\left(\frac{g\mu_B H}{2k_B T}\right)\right] \end{aligned}$$

$$= -n_I k_B y^2 \left[(2J+1)^2 \text{csch}^2((2J+1)y) - \text{csch}^2(y)\right], \tag{1.31}$$

with $y = g\mu_B H/2k_B T$. Eq. 1.31 will be used in Chapter 5 to analyze the LT heat capacity data of a half-Heusler composite series. In addition, the ferromagnetic contribution to the heat capacity in a magnetic field will be there derived and utilized.

CHAPTER 2

Governing Equations in Thermoelectric Transport

2.1 Introduction

From Section 1.1, we understand that the primary goal of thermoelectrics (TEs) research is to achieve high zT values over a broad range of temperatures for TE power generation. $zT = S^2\sigma T/\kappa$ is controlled by the Seebeck coefficient, S, the electrical conductivity, σ, and the thermal conductivity, κ. The underlying physics of the three parameters has a large impact on the zT values achievable in a given material system, as highlighted in Figure 1.4. Therefore, it is critical that we thoroughly develop the model physics that governs the TE transport processes relevant in semiconductors and metals. The most widely regarded method for handling the TE transport physics was derived by Boltzmann and is presented in Section 2.2. The Boltzmann transport equation (BTE) is also treated in Refs. [2, 39, 40].

2.2 Boltzmann Transport Equation

At its core, the BTE describes the return to equilibrium of an out-of-equilibrium system of electrons. It is semiclassical in the sense that it uses the quantum mechanical expression for the electronic Fermi-Dirac distribution function, yet classical generalized forces. In Section 2.2.1, we develop the BTE utilizing the relaxation-time approximation (RTA), and then in Sections 2.2.2 and 2.2.3, respectively, we describe the limits of the BTE in the cases of degenerate semiconductors (or metals) and non-degenerate semiconductors.

2.2.1 Generic Formalism

While the equilibrium Fermi-Dirac distribution function we mentioned in Section 1.4.2 was only a function of the electronic energy, E, the Fermi level, E_F, and temperature, T, we here elevate the function to generically depend on the position of an electron, $\vec{r}$, the electronic momentum, $\vec{k}$,

and the time, t. The three parameters seem to be the most critical for describing out-of-equilibrium systems since by definition non-equilibrium systems are not spatially uniform in temperature and continuously seek equilibrium. For the forces present, we directly include an electric field, $\vec{\mathscr{E}}$, to drive the transport. Later, a temperature gradient will naturally arise within the equations as a representation of a diffusive force.

To begin, we can write down the continuity equation of the distribution function reliant on the convective derivative

$$\begin{aligned} D_t f(\vec{r},\vec{k},t) &= (\partial_t + \vec{v}\cdot\vec{\nabla}_r + \dot{\vec{k}}\cdot\vec{\nabla}_k) f(\vec{r},\vec{k},t) = \left(\frac{\partial f}{\partial t}\right)_{coll} \\ &= \frac{\partial f}{\partial t} + \vec{v}\cdot\vec{\nabla}_r f + \frac{q}{\hbar}\vec{\mathscr{E}}\cdot\vec{\nabla}_k f = \left(\frac{\partial f}{\partial t}\right)_{coll}. \end{aligned} \tag{2.1}$$

The convective term is equal to the collision term in Eq. 2.1 since the electrons in the system will interact with each other and redistribute their individual momenta. The $\vec{\nabla}_i f$ are gradients of the distribution with respect to the variable i. In the second line of Eq. 2.1, the electric field is inserted as the force that shifts the momentum by acting on the charges of magnitude q. The partial time-derivative of the distribution function is quite small compared to the other driving terms, so it can be ignored. We can then solve for the collision term to obtain the Boltzmann transport equation:

$$\left(\frac{\partial f}{\partial t}\right)_{coll} = \vec{v}\cdot\vec{\nabla}_r f + \frac{q}{\hbar}\vec{\mathscr{E}}\cdot\vec{\nabla}_k f. \tag{2.2}$$

The simplest approach to calculating the collision term is to make the relaxation-time approximation (RTA) that the rate of return to equilibrium is set by some time constant, $\tau(\vec{k})$, called the relaxation time. In addition, how quickly the non-equilibrium distribution function changes is directly proportional to how far out of equilibrium the distribution is perturbed. Therefore,

$$\left(\frac{\partial f}{\partial t}\right)_{coll} = -\frac{f(\vec{k}) - f^0(\vec{k})}{\tau(\vec{k})}, \tag{2.3}$$

where $f^0(\vec{k})$ is the equilibrium distribution function. Furthermore, we assume that the distribution function is not too far out of equilibrium so that we can set the gradients that drive the distribution function to equilibrium to be the same ones that keep the system at equilibrium. As a result,

$$\vec{\nabla}_r f(\vec{r},\vec{k},t) \approx \vec{\nabla}_r f^0(\vec{r},\vec{k}) = \left(-\vec{\nabla}_r \xi - \frac{E-\xi}{T}\vec{\nabla}_r T\right)\frac{\partial f^0}{\partial E} \tag{2.4}$$

$$\vec{\nabla}_k f(\vec{r},\vec{k},t) \approx \vec{\nabla}_k f^0(\vec{r},\vec{k}) = \hbar\vec{v}\,\frac{\partial f^0}{\partial E}. \tag{2.5}$$

In Eq. 2.4, we use the "chemical potential", ξ, in place of E_F for full generality, since ξ is the temperature-dependent version of E_F with $\xi(T=0) = E_F$. The temperature gradient arises

naturally through the spatial derivative of the Fermi-Dirac distribution. Because $E = E(\vec{k})$, the spatial derivative of the electron energy is zero and therefore not present in Eq. 2.4. Eq. 2.5 stems from the fact that $\vec{\nabla}_k E = \hbar\vec{v}$. The perturbed distribution function can then be solved for by combining Eqs. 2.2 - 2.5 to get

$$f(\vec{k}) = f^0(\vec{k}) + \tau(\vec{k})\vec{v}(\vec{k})\left(\vec{\nabla}_r\,\xi^* + \frac{E-\xi}{T}\,\vec{\nabla}_r T\right)\frac{\partial f^0}{\partial E}, \tag{2.6}$$

which is the so-called "linearized" BTE due to the assumptions made in Eq. 2.4 and 2.5. We have defined $\vec{\nabla}_r\,\xi^* = \vec{\nabla}_r\,\xi - q\vec{\mathscr{E}}$, with ξ^* the "electrochemical potential" that includes the effect of the electric field on the chemical potential.

Because the whole point of presenting the BTE here is to understand the transport of charge and heat for TE research, we need to define the charge and heat currents. We must sum the electrical current density and heat current density over all electronic energies and account for the three-dimensional density of states (Eq. 1.26), as done similarly in Section 1.4.2. The electrical current density is then

$$\vec{\mathscr{J}} = \frac{q}{V}\int_0^\infty \vec{v}(E)f(E)D(E)dE, \tag{2.7}$$

while the heat current density is

$$\vec{\mathcal{Q}} = \frac{1}{V}\int_0^\infty \vec{v}(E)(E-\xi)f(E)D(E)dE, \tag{2.8}$$

where the amount of heat that each charge carries is $E - \xi$. At equilibrium, there is no net charge nor heat transport, so the term f^0 in Eq. 2.6 is irrelevant to Eqs. 2.7 and 2.8, which then have magnitude

$$\mathscr{J} = \frac{q}{V}\int_0^\infty v^2(E)\tau(E)\left(\vec{\nabla}_r\,\xi^* + \frac{E-\xi}{T}\,\vec{\nabla}_r T\right)\frac{\partial f^0}{\partial E}D(E)dE \tag{2.9}$$

and

$$\mathcal{Q} = \frac{q}{V}\int_0^\infty v^2(E)\tau(E)(E-\xi)\left(\vec{\nabla}_r\,\xi^* + \frac{E-\xi}{T}\,\vec{\nabla}_r T\right)\frac{\partial f^0}{\partial E}D(E)dE. \tag{2.10}$$

To connect Eqs. 2.9 and 2.10 with experiment, we can set the electric field and thermal gradient as acting along the $\hat{x}$ axis of a rectangular bar of a sample material, similar to Fig. 1.5. The velocity of the carriers is then $v_x^2 = v^2/3 = 2E/3m^*$. The gradients of the electrochemical potential and temperature with respect to the position vector, $\vec{\nabla}_r$, are also replaced by the singular direction equivalent, d/dx. Eqs. 2.9 and 2.10 become

$$\begin{aligned}\mathscr{J}_x &= \frac{2q}{3m^*V}\left[\int_0^\infty \tau(E)E\,\frac{d\xi^*}{dx}\frac{\partial f^0}{\partial E}\,D(E)dE + \int_0^\infty \tau(E)E(E-\xi)\left(\frac{1}{T}\frac{dT}{dx}\right)\frac{\partial f^0}{\partial E}\,D(E)dE\right] \\ &= qL_{11}\left(-\frac{1}{T}\frac{d\xi^*}{dx}\right) + qL_{12}\left(-\frac{1}{T^2}\frac{dT}{dx}\right),\end{aligned} \tag{2.11}$$

and

$$\begin{aligned}\mathcal{Q}_x &= \frac{2q}{3m^*V}\int_0^\infty \tau(E)E(E-\xi)\,\frac{d\xi^*}{dx}\frac{\partial f^0}{\partial E}\,D(E)dE \\ &\quad + \frac{2q}{3m^*V}\int_0^\infty \tau(E)E(E-\xi)^2\left(\frac{1}{T}\frac{dT}{dx}\right)\frac{\partial f^0}{\partial E}\,D(E)dE \\ &= L_{21}\left(-\frac{1}{T}\frac{d\xi^*}{dx}\right) + L_{22}\left(-\frac{1}{T^2}\frac{dT}{dx}\right),\end{aligned} \tag{2.12}$$

where the Onsager coefficients, L_{ij}, are defined as

$$\begin{aligned}L_{11} &\equiv -\frac{2T}{3m^*V}\int_0^\infty \tau(E)E\,\frac{\partial f^0}{\partial E}\,D(E)dE, \\ L_{12} &\equiv -\frac{2T}{3m^*V}\int_0^\infty \tau(E)E(E-\xi)\,\frac{\partial f^0}{\partial E}\,D(E)dE = L_{21}, \\ L_{22} &\equiv -\frac{2T}{3m^*V}\int_0^\infty \tau(E)E(E-\xi)^2\,\frac{\partial f^0}{\partial E}\,D(E)dE.\end{aligned} \tag{2.13}$$

It is evident from Eqs. 2.11 and 2.12 that the electrical current density and heat current density are both affected by the electric field and the thermal gradient, not just the intuitive singular driving forces. Because the individual Onsager coefficients are nearly identical in form besides the power of E in the integral, we define an auxiliary integral for later use:

$$K_s \equiv -\frac{2T}{3m^*V}\int_0^\infty \tau(E)E^{s+1}\,\frac{\partial f^0}{\partial E}\,D(E)dE. \tag{2.14}$$

Eqs. 2.11 and 2.12 become

$$\mathscr{J}_x = qK_0\left(-\frac{1}{T}\frac{d\xi^*}{dx}\right) + q(K_1 - \xi K_0)\left(-\frac{1}{T^2}\frac{dT}{dx}\right) \tag{2.15}$$

and

$$\mathcal{Q}_x = (K_1 - \xi K_0)\left(-\frac{1}{T}\frac{d\xi^*}{dx}\right) + (K_2 - 2\xi K_1 + \xi^2 K_0)\left(-\frac{1}{T^2}\frac{dT}{dx}\right). \tag{2.16}$$

With the BTE formalism in place, we can now derive the desired TE transport properties.

2.2.1.1 Charge Carrier Concentration

The number of charge carriers present in unit volume, n, of a solid can be readily controlled through the process of doping, alloying, secondary phase formation, etc. n has a tremendous impact on TE transport and zT, as displayed in Fig. 1.4. Regardless of the equilibrium status of an electronic system, the charge carrier concentration should be constant at a given temperature and Fermi level. The charge carrier concentration is simply a matter of statistics and does not require the BTE nor the current densities, but we derive it first for its fundamental importance.

For the three-dimensional density of states in Eq. 1.26, the charge carrier concentration is calculated as

$$\begin{aligned} n &= \frac{1}{V}\int_0^\infty f^0(E)D(E)dE = \frac{1}{2\pi^2}\left(\frac{2m^*}{\hbar^2}\right)^{3/2}\int_0^\infty \frac{E^{1/2}}{\exp\left[(E-\xi)/k_BT\right]+1}\,dE \\ &= \frac{1}{2\pi^2}\left(\frac{2m^*k_BT}{\hbar^2}\right)^{3/2} F_{\frac{1}{2}}(\eta), \end{aligned} \tag{2.17}$$

where we substituted the reduced energy, $\epsilon \equiv E/k_BT$, and reduced chemical potential, $\eta \equiv \xi/k_BT$, in the first line of Eq. 2.17 to yield the Fermi integral in the second line, defined as

$$F_j(\eta) \equiv \int_0^\infty \frac{\epsilon^j}{\exp\left(\epsilon-\eta\right)+1}\,d\epsilon. \tag{2.18}$$

2.2.1.2 Electrical Conductivity

Because the electrical conductivity and carrier concentration of a given material are usually temperature dependent, the true value of σ and n are taken at a single temperature. With that in mind, to determine the electrical conductivity, we set the temperature gradient of the sample to zero and, consequently, the Fermi level is homogeneous throughout the material. Therefore, by the definition of the electrical conductivity and Eq. 2.15,

$$\sigma \equiv \frac{\mathscr{J}_x}{\mathscr{E}_x} = qK_0\left(-\frac{1}{T\mathscr{E}_x}\frac{d\xi^*}{dx}\right) = \frac{q^2}{T}K_0. \tag{2.19}$$

2.2.1.3 Seebeck Coefficient

The Seebeck coefficient is measured in an open-circuit condition ($\mathscr{J}_x = 0$) and in the presence of a temperature gradient. The first fact, coupled with Eq. 2.15, gives us

$$\frac{1}{T}\frac{d\xi^*}{dx} = -\frac{1}{T^2}\left(\frac{K_1 - \xi K_0}{K_0}\right)\frac{dT}{dx}, \tag{2.20}$$

which conveniently ties into the definition of the Seebeck coefficient as the ratio of the electrochemical potential to the temperature gradient, that is,

$$S \equiv -\frac{1}{q}\frac{d\xi^*}{dx}\left(\frac{dT}{dx}\right)^{-1} = \frac{1}{qT}\frac{K_1 - \xi K_0}{K_0}. \tag{2.21}$$

2.2.1.4 Peltier Coefficient

As a measure of the heat current density driven by the electric field in a temperature-homogeneous material, the Peltier coefficient is, from Eqs. 2.15 and 2.16,

$$\begin{aligned}\Pi \equiv \frac{\mathcal{Q}_x}{\mathscr{J}_x} &= \frac{K_1 - \xi K_0}{T}\frac{d\xi^*}{dx}\left(\frac{qK_0}{T}\frac{d\xi^*}{dx}\right)^{-1} \\ &= \frac{1}{q}\frac{K_1 - \xi K_0}{K_0} = TS.\end{aligned} \tag{2.22}$$

The last equality in Eq. 2.22 is known as the second Kelvin relation that relates the Peltier and Seebeck coefficients through a direct proportionality with the temperature.

2.2.1.5 Electronic Thermal Conductivity

The thermal conductivity contribution by the charge carriers, κ_e, is determined in a similar manner as the Seebeck coefficient, i.e. in the open-circuit condition ($\mathscr{J}_x = 0$) and in the presence of a temperature gradient. κ_e is defined as the ratio of the heat current density to the temperature gradient, such that

$$\begin{aligned}\kappa_e &= -\mathcal{Q}_x\left(\frac{dT}{dx}\right)^{-1} = (K_1 - \xi K_0)\left(\frac{1}{T}\frac{d\xi^*}{dx}\right)\left(\frac{dT}{dx}\right)^{-1} + \ (K_2 - 2\xi K_1 + \xi^2 K_0)\left(\frac{1}{T^2}\right) \\ &= -\frac{1}{T^2}\frac{(K_1 - \xi K_0)^2}{K_0} + (K_2 - 2\xi K_1 + \xi^2 K_0)\left(\frac{1}{T^2}\right) \\ &= \frac{1}{T^2}\left(K_2 - \frac{K_1^2}{K_0}\right).\end{aligned} \tag{2.23}$$

2.2.1.6 Lorenz Number

A final important parameter for TE transport is the so-called Lorenz number that relates the electronic contribution to the thermal conductivity, κ_e, and the electrical conductivity, σ. Using Eqs. 2.19 and 2.23,

$$\begin{aligned}L \equiv \frac{\kappa_e}{\sigma T} &= \frac{1}{T^2}\left(K_2 - \frac{K_1^2}{K_0}\right) q^{-2} K_0^{-1} \\ &= \frac{1}{q^2T^2}\left(\frac{K_2}{K_0} - \frac{K_1^2}{K_0^2}\right).\end{aligned} \tag{2.24}$$

2.2.1.7 Power Law $\tau(E)$

The integrals within Section 2.2.1 all contain $\tau(E)$, the energy-dependent relaxation time. $\tau(E)$ is the parameter through which electronic scattering processes are incorporated within the BTE framework. It is customary and accurate to make the assumption that

$$\tau(E) = \tau_0 E^r, \tag{2.25}$$

where τ_0 is a constant independent of energy, and r is the scattering parameter that sets the power law. For example, $r = -3/2, 0,$ and $1/2$ describe the scattering of charge carriers dominantly by acoustic phonons, neutral impurities, and ionized impurities, respectively. Implementing the electronic density of states (Eq. 1.26) and the relaxation time (Eq. 2.25), we can write the K_s integrals (Eq. 2.14) as

$$K_s = -\frac{T\tau_0\sqrt{m^*}}{3\pi^2}\left(\frac{2}{\hbar}\right)^{3/2}\int_0^\infty E^{s+r+\frac{3}{2}}\frac{\partial f^0}{\partial E}\,dE. \tag{2.26}$$

Using integration by parts, we can simplify Eq. 2.26 even further:

$$\begin{aligned} K_s &= -\frac{T\tau_0\sqrt{m^*}}{3\pi^2}\left(\frac{2}{\hbar}\right)^{3/2}\left[E^{s+r+\frac{3}{2}}\,f^0\Big|_0^\infty - \left(s+r+\frac{3}{2}\right)\int_0^\infty E^{s+r+\frac{1}{2}}f^0\,dE\right] \\ &= \frac{T\tau_0\sqrt{m^*}}{3\pi^2}\left(\frac{2}{\hbar}\right)^{3/2}\left(s+r+\frac{3}{2}\right)(k_BT)^{s+r+\frac{3}{2}}F_{s+r+\frac{1}{2}}(\eta). \end{aligned} \tag{2.27}$$

The boundary term in the first line of Eq. 2.27 is zero at each endpoint, while the second term gives off $(s + r + \frac{3}{2})$ factors of k_BT by changing to the Fermi integral defined in Eq. 2.18.

With the three-dimensional electronic density of states and power law scaling of the relaxation time with energy, we can rewrite σ (Eq. 2.19), S (Eq. 2.21), Π (Eq. 2.22), κ_e (Eq. 2.23), and L (Eq. 2.24) as

$$\sigma = \frac{q^2\tau_0\sqrt{m^*}}{3\pi^2}\left(\frac{2}{\hbar}\right)^{3/2}\left(r+\frac{3}{2}\right)(k_BT)^{r+\frac{3}{2}}F_{r+\frac{1}{2}}(\eta), \tag{2.28}$$

$$\begin{aligned} S &= \frac{1}{qT}\left[\frac{\left(r+\frac{5}{2}\right)(k_BT)^{r+\frac{5}{2}}F_{r+\frac{3}{2}}(\eta)}{\left(r+\frac{3}{2}\right)(k_BT)^{r+\frac{3}{2}}F_{r+\frac{1}{2}}(\eta)} - \xi\right] = \frac{k_B}{q}\left[\frac{\left(r+\frac{5}{2}\right)F_{r+\frac{3}{2}}(\eta)}{\left(r+\frac{3}{2}\right)F_{r+\frac{1}{2}}(\eta)} - \eta\right] \\ &= \frac{\Pi}{T}, \end{aligned} \tag{2.29}$$

$$\kappa_e = \frac{\tau_0\sqrt{m^*}}{3\pi^2T^2}\left(\frac{2}{\hbar}\right)^{3/2}(k_BT)^{r+\frac{7}{2}}\left[\left(r+\frac{7}{2}\right)F_{r+\frac{5}{2}}(\eta) - \frac{\left(r+\frac{5}{2}\right)^2F^2_{r+\frac{3}{2}}(\eta)}{\left(r+\frac{3}{2}\right)F_{r+\frac{1}{2}}(\eta)}\right], \tag{2.30}$$

$$L = \left(\frac{k_B}{q}\right)^2 \left[\frac{\left(r+\frac{7}{2}\right) F_{r+\frac{5}{2}}(\eta)}{\left(r+\frac{3}{2}\right) F_{r+\frac{1}{2}}(\eta)} - \frac{\left(r+\frac{5}{2}\right)^2 F^2_{r+\frac{3}{2}}(\eta)}{\left(r+\frac{3}{2}\right)^2 F^2_{r+\frac{1}{2}}(\eta)}\right]. \tag{2.31}$$

Eq. 2.29 is used in Chapter 3 to solve for η using experimental data for S and r, then the resultant temperature-dependent η is input to Eqs. 2.31 and 2.30 to determine L and κ_e, respectively. Evidently, Eqs. 2.28 - 2.31 are not merely theoretical considerations but actually quite applicable in real-world materials.

2.2.2 The Degenerate Limit

In the case of highly doped (extrinsic) semiconductors, with $n \gtrsim 10^{20}$ cm^{-3}, and metals, with $n \gtrsim 10^{22}$ cm^{-3}, the electron (hole) transport occurs within the conduction (valence) bands. Such a scenario is known as the "degenerate limit" and implies that the Fermi level intersects the bands. With ξ measured starting from the bottom of the conduction band for electrons, or top of the valence band for holes, the degenerate limit indicates that $\xi/k_BT \gg 0$. The Fermi integrals pervading Eqs. 2.17 and 2.28 - 2.31 can be simplified via the Sommerfeld expansion [24] but will not be detailed here besides the following result:

$$\lim_{\eta \gg 0} F_j(\eta) \approx \frac{\eta^{j+1}}{j+1} + \frac{j\pi^2}{6}\eta^{j-1} + O(\eta^{j-3}). \tag{2.32}$$

Putting Eq. 2.32 to work with the carrier concentration (Eq. 2.17) and the electrical conductivity (Eq. 2.28), we can drop the terms of $O(\eta^{j-1})$ due to the direct proportionality with the Fermi integral to find

$$n_{deg} = \frac{1}{3\pi^2}\left(\frac{2m^*\xi}{\hbar^2}\right)^{3/2}, \tag{2.33}$$

$$\sigma_{deg} = \frac{q^2\tau_0\sqrt{m^*}}{3\pi^2}\left(\frac{2}{\hbar}\right)^{3/2}\xi^{r+\frac{3}{2}}. \tag{2.34}$$

Both parameters in the degenerate limit are essentially constant with temperature unless the Fermi level moves within the electronic bands or the effective mass (band curvature) changes with temperature.

Because the Seebeck coefficient contains a ratio of two Fermi integrals (Eq. 2.29), we maintain terms up to $O(\eta^{j-1})$ in the numerator and denominator to yield

$$
\begin{aligned}
S_{deg} &= \frac{k_B}{q}\frac{\left(r+\frac{5}{2}\right)\left[\frac{\eta^{r+\frac{5}{2}}}{r+\frac{5}{2}}+\frac{\left(r+\frac{3}{2}\right)\pi^2\eta^{r+\frac{1}{2}}}{6}\right]-\eta\left(r+\frac{3}{2}\right)\left[\frac{\eta^{r+\frac{3}{2}}}{r+\frac{3}{2}}+\frac{\left(r+\frac{1}{2}\right)\pi^2\eta^{r-\frac{1}{2}}}{6}\right]}{\left(r+\frac{3}{2}\right)\left[\frac{\eta^{r+\frac{3}{2}}}{r+\frac{3}{2}}+\frac{\left(r+\frac{1}{2}\right)\pi^2\eta^{r-\frac{1}{2}}}{6}\right]} \\
&= \frac{\pi^2 k_B}{6q}\left(r+\frac{3}{2}\right)(2\eta^{r+\frac{1}{2}})\eta^{-r-\frac{3}{2}} = \frac{\pi^2 k_B^2 T}{3q\xi}\left(r+\frac{3}{2}\right) \\
&= \frac{\Pi}{T},
\end{aligned}
\tag{2.35}
$$

where the term of $O(\eta^{r-1/2})$ in the first equality of Eq. 2.35 was ignored in the denominator. The Seebeck coefficient follows a linear temperature dependence in the degenerate limit, with values that can be quite small, especially with acoustic phonon scattering dominant ($r \approx -3/2$).

We perform the same manipulations for the electronic thermal conductivity (Eq. 2.30), setting a parameter A to be the product of the bracket prefactor and the $\eta^{-r-3/2}$ that comes from the first order expansion of the denominator. The result is

$$
\begin{aligned}
\kappa_{e,deg} &= A\left(r+\frac{7}{2}\right)\left(\frac{\eta^{r+\frac{7}{2}}}{r+\frac{7}{2}}+\frac{\pi^2}{6}\left(r+\frac{5}{2}\right)\eta^{r+\frac{3}{2}}\right)\left(r+\frac{3}{2}\right)\left(\frac{\eta^{r+\frac{3}{2}}}{r+\frac{3}{2}}+\frac{\pi^2}{6}\left(r+\frac{1}{2}\right)\eta^{r-\frac{1}{2}}\right) \\
&\quad - A\left(r+\frac{5}{2}\right)^2\left(\frac{\eta^{r+\frac{5}{2}}}{r+\frac{5}{2}}+\frac{\pi^2}{6}\left(r+\frac{3}{2}\right)\eta^{r+\frac{1}{2}}\right)^2 \\
&= A\frac{\pi^2}{6}\eta^{2r+3}\left[\left(r+\frac{7}{2}\right)\left(r+\frac{5}{2}\right)+\left(r+\frac{3}{2}\right)\left(r+\frac{1}{2}\right)-2\left(r+\frac{5}{2}\right)\left(r+\frac{3}{2}\right)\right] \\
&\quad + A\frac{\pi^4}{36}\eta^{2r+1}\left[\left(r+\frac{1}{2}\right)\left(r+\frac{3}{2}\right)\left(r+\frac{5}{2}\right)\left(r+\frac{7}{2}\right)-\left(r+\frac{3}{2}\right)^2\left(r+\frac{5}{2}\right)^2\right] \\
&= A\frac{\pi^2}{3}\eta^{2r+3} - A\frac{\pi^4}{18}\eta^{2r+1}\left(r+\frac{3}{2}\right)\left(r+\frac{5}{2}\right) \\
&= \frac{\tau_0\sqrt{m^*}}{3\pi^2T^2}\left(\frac{2}{\hbar}\right)^{3/2}(k_BT)^{r+\frac{7}{2}}\eta^{-r-\frac{3}{2}}\left[\frac{\pi^2}{3}\eta^{2r+3}-\frac{\pi^4}{18}\eta^{2r+1}\left(r+\frac{3}{2}\right)\left(r+\frac{5}{2}\right)\right] \\
&= \frac{\tau_0\sqrt{m^*}}{9}\left(\frac{2}{\hbar}\right)^{3/2}k_B^2\xi^{r+\frac{3}{2}}\left[1-\frac{\pi^2}{6}\left(\frac{k_BT}{\xi}\right)^2\left(r+\frac{3}{2}\right)\left(r+\frac{5}{2}\right)\right],
\end{aligned}
\tag{2.36}
$$

with A reintroduced in the second-to-last line in Eq. 2.36. $\kappa_{e,deg}$ is almost constant as a function of temperature if the small correction term of $O(k_BT/\xi)^2$ is ignored.

The Lorenz number is algebraically nearly identical with the electronic contribution to the thermal conductivity, except that the denominator term in Eq. 2.31 is squared. Therefore, we find

$$
\begin{aligned}
L_{deg} &= \left(\frac{k_B}{q}\right)^2 \eta^{-2r-3}\left[\frac{\pi^2}{3}\eta^{2r+3} - \frac{\pi^4}{18}\eta^{2r+1}\left(r+\frac{3}{2}\right)\left(r+\frac{5}{2}\right)\right] \\
&= \frac{\pi^2}{3}\left(\frac{k_B}{q}\right)^2\left[1 - \frac{\pi^2}{6}\left(\frac{k_BT}{\xi}\right)^2\left(r+\frac{3}{2}\right)\left(r+\frac{5}{2}\right)\right].
\end{aligned}
\tag{2.37}
$$

Without the second order correction term, L_{deg} is a constant with value $L_0 \equiv 2.44$ x 10^{-8} V^2 K^{-2}.

2.2.3 The Non-Degenerate Limit

For intrinsic semiconductors and those that are only lightly doped, typically with $n \lesssim 10^{18}$ cm^{-3}, carrier transport occurs by thermal excitations to the conduction or valence bands from the Fermi level. Such a scenario is known as the "non-degenerate limit" and implies that the Fermi level sits in the middle of the gap between the bands, i.e. $\xi/k_BT \ll 0$. In this limit, the Fermi integrals become

$$
\lim_{\eta\ll 0} F_j(\eta) \approx e^\eta \int_0^\infty \epsilon^j e^{-\epsilon} d\epsilon = e^\eta\,\Gamma(j+1),
\tag{2.38}
$$

where $\Gamma(j+1) = j\Gamma(j)$ is the Gamma function with particularly useful values of $\Gamma(1/2) = \sqrt{\pi}$ and $\Gamma(1) = \Gamma(2) = 1$. With these Gamma function properties and Eq. 2.38 in mind, we can simplify the Eqs. 2.17 and 2.28 - 2.31 to be

$$
n_{ndeg} = \frac{1}{4}\left(\frac{2m^*k_BT}{\pi\hbar^2}\right)^{3/2} e^\eta,
\tag{2.39}
$$

$$
\begin{aligned}
\sigma_{ndeg} &= \frac{q^2\tau_0\sqrt{m^*}}{3\pi^2}\left(\frac{2}{\hbar}\right)^{3/2}\left(r+\frac{3}{2}\right)(k_BT)^{r+\frac{3}{2}}\,e^\eta\,\Gamma\left(r+\frac{3}{2}\right) \\
&= \frac{q^2\tau_0\sqrt{m^*}}{3\pi^2}\left(\frac{2}{\hbar}\right)^{3/2}(k_BT)^{r+\frac{3}{2}}\,\Gamma\left(r+\frac{5}{2}\right)e^\eta,
\end{aligned}
\tag{2.40}
$$

$$
\begin{aligned}
S_{ndeg} &= \frac{k_B}{q}\left[\frac{\left(r+\frac{5}{2}\right)\Gamma\left(r+\frac{5}{2}\right)}{\left(r+\frac{3}{2}\right)\Gamma\left(r+\frac{3}{2}\right)} - \eta\right] = \frac{k_B}{q}\left(r+\frac{5}{2}-\eta\right) \\
&= \frac{\Pi}{T},
\end{aligned}
\tag{2.41}
$$

$$
\begin{aligned}
\kappa_{e,ndeg} &= \frac{\tau_0\sqrt{m^*}}{3\pi^2T^2}\left(\frac{2}{\hbar}\right)^{3/2}(k_BT)^{r+\frac{7}{2}}\,e^\eta\left[\left(r+\frac{7}{2}\right)\Gamma\left(r+\frac{7}{2}\right) - \left(r+\frac{5}{2}\right)^2\Gamma\left(r+\frac{5}{2}\right)\right] \\
&= \frac{\tau_0\sqrt{m^*}}{3\pi^2T^2}\left(\frac{2}{\hbar}\right)^{3/2}(k_BT)^{r+\frac{7}{2}}\,e^\eta\,\Gamma\left(r+\frac{7}{2}\right),
\end{aligned}
\tag{2.42}
$$

$$
\begin{aligned}
L_{ndeg} &= \left(\frac{k_B}{q}\right)^2 \left[\frac{\left(r+\frac{7}{2}\right)\Gamma\left(r+\frac{7}{2}\right)}{\Gamma\left(r+\frac{5}{2}\right)} - \frac{\Gamma^2\left(r+\frac{7}{2}\right)}{\Gamma^2\left(r+\frac{5}{2}\right)}\right] \\
&= \left(\frac{k_B}{q}\right)^2 \left[\left(r+\frac{7}{2}\right)^2\left(r+\frac{5}{2}\right) - \left(r+\frac{5}{2}\right)^2\right] = \left(\frac{k_B}{q}\right)^2 \left(r+\frac{5}{2}\right).
\end{aligned}
\tag{2.43}
$$

Eqs. 2.39 and 2.40 are particularly useful in analyzing temperature-dependent Hall effect measurement data and $\sigma(T)$, respectively, for intrinsic semiconductors. In particular, if we assume that the Fermi level sits in the middle of the electronic energy band gap, then the separation between the top of the valence band and the bottom of the conduction is $E_g = 2E_F$, and $\eta = E_g/2k_BT$. Fitting an exponential curve to $n(T)$ or $\sigma(T)$ therefore allows for extraction of the band gap.

CHAPTER 3

Enhanced zT and Attempts to Chemically Stabilize Cu_2Se via Sn doping

3.1 Motivation: Superionic Conductors as Thermoelectric Materials

One fascinating family of thermoelectric (TE) materials that has generated a lot of interest as of late is the superionic conductors (SICs), typified by Cu_2Se [17] and Cu_2S [41]. As the name entails, SICs are solids in which certain ions (Cu^+ in the case of Cu_2Se and Cu_2S), rather than occupying rigid lattice sites, acquire a directional flow when subjected to an external electric field. The ionic conductivities ($\sigma_I = \mathscr{J}_I \mathscr{E}^{-1}$, with $\mathscr{J}_I$ the ionic current density and $\mathscr{E}$ the electric field) of SICs in their solid state are similar to the σ_I of ionic conductors (e.g., NaCl, CaF_2, etc.) in their liquid state, with values of order 1 $(\Omega\text{-cm})^{-1}$ [42]. This is in stark contrast to normal solids having σ_I of order 10^{-8} $(\Omega\text{-cm})^{-1}$ as a result of their substantially fixed ions. In most SICs, the crystal structure consists of two distinct sublattices, one that forms a rigid, ordered backbone and one where the ions can move in a fluid-like fashion between various interstitial sites.

Thermodynamic studies of the normal-to-superionic phase transition show that the entropy change per atom during the superionic transition is approximately the same as the entropy change per atom upon melting, indicating that half of the crystal, or one sublattice, is quasi-molten, or "liquid-like" [42], as depicted in Figure 3.1. SICs have the potential to be important TE materials because the fluid nature of the quasi-molten sublattice hinders the transport of heat by transverse mode phonons [17, 43], while the fixed sublattice provides a crystalline pathway for electronic conduction. These features reduce κ while preserving σ, respectively, which leads to a significant enhancement in zT.

Indeed, initial reports on Cu_2Se demonstrated $zT \approx 1.5$ at 1000 K [17, 44], which could amount to device conversion efficiencies of around 10%. Since the work of Liu *et al.* [17], a variety of unique synthesis techniques, including self-propagating high-temperature synthesis [45],

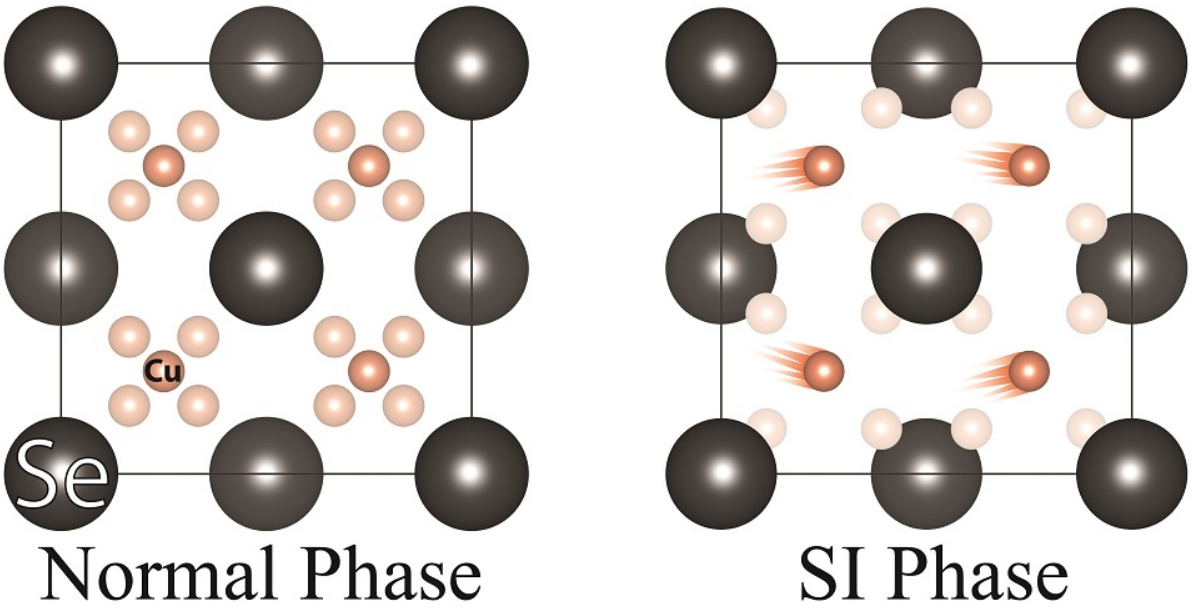

Figure 3.1: **Schematic comparison of the normal phase and superionic phase of superionic conductors**. Here, we illustrate the specific case of Cu_2Se with its face-centered cubic crystal structure. In the normal low-temperature α-phase, both sublattices are fixed, while in the superionic β-phase, the Cu sublattice becomes quasi-molten, and the Cu ions are highly mobile between tetrahedral sites when an electrical field is applied. The opacity of the Cu ions in both phases represents the site occupancy; in the SIC phase, the Cu ions occupy the octahedral sites to a lesser extent than in the normal phase.

plasma-activated reactive sintering [46], and wet chemical synthesis [47, 48], as well as doping efforts [49, 50, 51, 52] and nanostructuring [48, 53, 54] have been used for both stoichiometric and copper-deficient compounds to create similar and even higher values of zT, including $zT \approx 2.1$ at 973 K recorded for nanostructured Cu_2Se by Gahtori *et al.* [54].

Regarding its crystal structure (Fig. 3.1), the normal room temperature (RT) α-phase of Cu_2Se is monoclinic, with the selenium anions forming a rigid framework in which the copper cations statically occupy the interstices [55, 56, 57, 58, 59, 60]. Upon heating, the material transitions to the superionic β-phase around 410 K, with the higher symmetry cubic anti-fluorite structure (space group $Fm\bar{3}m$) [57, 58, 59, 60, 61, 62, 63]. Being superionic, the copper cations in the high-temperature (HT) β-phase can flow freely between the tetrahedral interstitial sites, as determined by X-ray diffraction [58, 63], neutron diffraction studies [64], nuclear magnetic resonance spectroscopy [65], and transmission electron microscopy [60]. *Ab initio* molecular dynamics demonstrate that the trajectories of the Cu atoms stray far away from their equilibrium positions as the temperature is elevated in the β-phase [66]. The disorder of the copper cation leads to thermal conductivity values as low as 0.5 W m^{-1} K^{-1} [54]. Coupling the small κ with the electronic behavior

of a p-type degenerate semiconductor, Cu_2Se possesses promising TE properties.

Yet, Cu_2Se cannot be used for continuous mid- to high-temperature power generation because of its tendency to materially degrade in TE application conditions [67, 68, 69, 70, 71], a prevalent issue for all SICs [72]. Specifically, when Cu_2Se is held at elevated temperatures ($\approx$ 750 K and above) and exposed to large currents ($\approx$ 1 A and above), as would be the case in TE generators, selenium evaporation and copper ion migration result in the expulsion of solid copper from the material. The reaction of free selenium and copper with the electrical contacts of the TE device causes an increased contact resistance, lowering the efficiency of power generation [46, 68, 70]. Furthermore, the eventual physical separation of the material from the electrical contacts of the device, due to the forceful expulsion of copper, terminates operation.

At the time of the study to be presented here [73], attempted solutions to the issue of material degradation in Cu_2Se had been entirely external, meaning that they were applied to the final material product [68, 70]. For example, using baffled ceramic coatings does indeed reduce the selenium evaporation, but undesirably decreases device efficiency by acting as a thermal short. In our study, we pursued the more fundamental, internal approach of substitutional doping, i.e. the replacement of a certain fraction of atoms of the base material with selected elements. Doping is a logical approach to stabilize copper selenide for several reasons.

First, doping can be reliably controlled at the beginning of the material synthesis process, providing the basis for repeatable results. Second, the introduction of foreign elements into the crystal structure of Cu_2Se can potentially block the long-range migration of Cu and, in turn, reduce the material degradation, as has been seen in the related superionic thermoelectric Cu_2S [74]. Similarly, the dopant atoms can act as point defects within the crystal structure and distort the lattice, thereby enhancing phonon scattering and decreasing thermal conductivity [2]. Last, doping is a well-known strategy for optimizing the carrier concentration to maximize the power factor, $PF = S^2\sigma$, provided that the carrier mobility is not degraded [75]. Thus, we chose substitutional doping as a possible means of mitigating the material degradation in Cu_2Se, while simultaneously preserving, or even enhancing, its superior TE properties.

Specifically, in this study, we focus on the compositional series $Cu_{2-2x}Sn_xSe$ with nominal dopant concentrations $x = 0$, 0.01, 0.02 and 0.05. Tin (Sn) was selected as the dopant element for two reasons. First, Sn can dissolve in the Cu_2Se matrix in small concentrations in either its 2+ or 4+ oxidation states [76], with effective ionic radii of $\approx$ 0.76 Å and $\approx$ 0.55 Å, respectively, in comparison to $\approx$ 0.60 Å for Cu^{1+} [77, 78]. The combination of the charge difference and distinct ionic radii between Sn and Cu within the Cu_2Se matrix will result in a distorted lattice. In turn, the electromigration pathway of the Cu^{1+} ions could be significantly hampered, thereby decreasing the loss of solid copper, as was previously shown in the mineral bornite [74]. Second, record high zT values of 2.6 at 923 K were recently demonstrated in single-crystal SnSe [20], making the

combination of Cu_2Se and SnSe an appealing system for TEs [79, 80]. Because of the reported low solubility limit of tin in copper selenide [76], our investigation utilized small concentrations of the dopant element. One final noteworthy advantage of the materials used in this study is that copper, tin and selenium are all earth abundant, inexpensive and nontoxic elements, which renders them suitable for TE applications.

The following three sections detail our work published in Ref. [73]. In particular, Section 3.2 describes the synthesis procedure and the resulting microstructure of the $Cu_{2-2x}Sn_xSe$ (x = 0, 0.01, 0.02 and 0.05) series that we studied. Section 3.3 presents the results of the HT TE property measurements, with the primary conclusion that the $Cu_{1.98}Sn_{0.01}Se$ sample possesses a 15% enhanced zT in comparison to the pure sample over a wide temperature range. Section 3.4 elucidates the outcomes of the current stress test performed in this study as a means of checking the electrical stability of the samples. Overall conclusions can be found in Section 3.5, while an update on more recent results is given in Section 3.6.

3.2 Synthesis and Microstructure

3.2.1 Experimental Details

In an argon atmosphere glovebox, Cu shot (6N, Alfa Aesar), Sn shot (5N, Alfa Aesar) and Se shot (5N, Alfa Aesar) were weighed out to match the stoichiometry of $Cu_{2-2x}Sn_xSe$, with x = 0, 0.01, 0.02 and 0.05. The elements were placed in carbon-coated quartz tubes, evacuated to 10^{-4} torr, and then sealed quickly by an oxygen-propane torch. The resulting ampoules were then heated from RT to 1423 K at 1 K per minute in a closed furnace, soaked at that temperature for 12 hours, slow cooled to 1023 K over the span of one day, annealed for 7 days, and then finally cooled to RT over the span of two days. The approximately 10 g solid ingots were removed from the quartz tubes and ground into powder by agate mortar and pestle in air, typically achieving grain sizes less than 150 microns. Both Cu_2Se and $Cu_{1.90}Sn_{0.05}Se$ ingots featured a layer of Se on the outside that was removed before further processing. The reacted powder was loaded into a 20 mm diameter graphite die lined with graphite paper, then cold pressed and spark plasma sintered at 923 K for 5 minutes at a pressure of 50 MPa. Graphite paper was removed from the samples, and their density, ρ, was determined by the Archimedes method. All samples were 98-100% theoretical density.

After synthesis, the samples were sectioned by a diamond saw into the proper geometries and sizes for characterization. To identify the compounds and structures present in the sintered samples, powder X-ray diffraction (PXRD) was performed using a Rigaku Ultima IV X-ray Diffractometer with incident radiation of wavelength $\lambda = 1.5406\,\text{Å}$. A HT stage was used for PXRD measurements at 473 K in addition to the RT scans. Scanning electron microscopy (SEM)

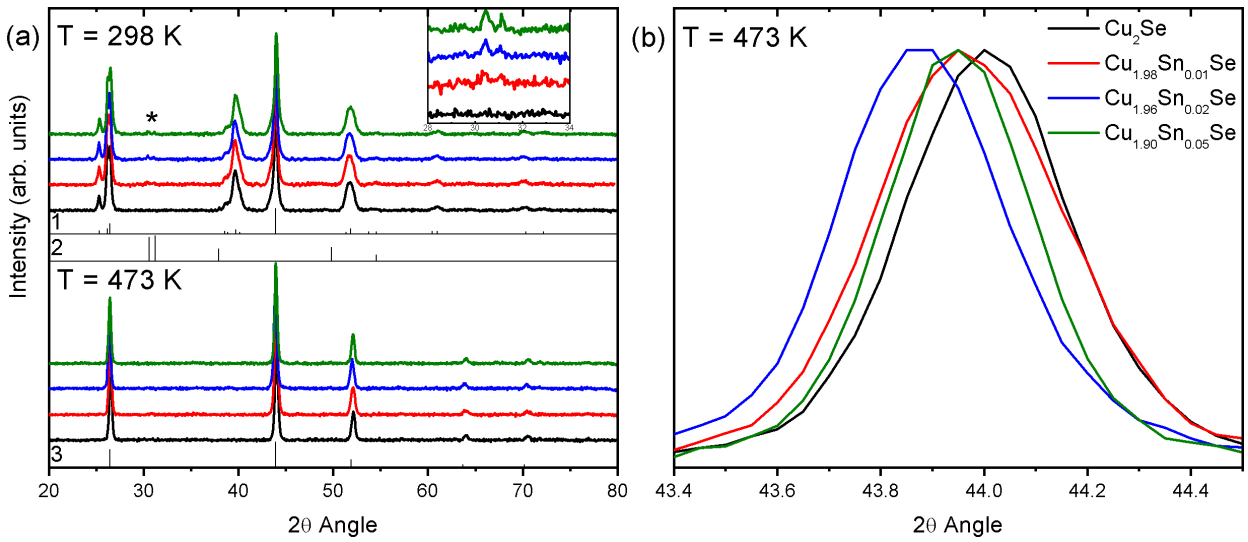

Figure 3.2: **Temperature-dependent powder X-ray diffraction patterns of the four $Cu_{2-2x}Sn_xSe$ samples in the study.** (a) The top panel includes the patterns at T = 298 K, while the bottom panel is for T = 473 K. Below the sample PXRD patterns are the known PDF cards of α-Cu_2Se, SnSe and β-Cu_2Se, labeled by 1, 2 and 3, respectively. At room temperature (RT), the Bragg peaks at $2\theta \approx 31.0°$ (marked by * and shown enlarged in the inset) for the Sn-doped samples are indexed by 3 (SnSe), whereas the rest of the peaks belong to 1 (α-Cu_2Se). Above the phase transition temperature, the patterns are indexed by 2 (β-Cu_2Se) and show no signs of 3 (SnSe), indicating that the secondary phase peaks are below the detection limit of the PXRD machine. This is caused by the well-known Debye-Waller effect and a greater dissolution of Sn in the Cu_2Se matrix at high temperatures, which is further supported by the main diffraction peak shifts to lower values of 2θ at T = 473 K, as shown in (b).

(JEOL-7800FLV) was performed to observe the microstructure, while *in situ* energy dispersive X-ray spectroscopy (EDX) was used to qualify chemical composition. All of the characterization equipment mentioned above is part of the Electron Microbeam Analysis Lab at the University of Michigan (UM).

3.2.2 Results and Discussion

Figure 3.2(a) displays the RT and HT PXRD patterns for the four samples in the study. For clarity, the higher energy and lower intensity Cu K_β lines of the main diffraction peaks have been removed. In all of the samples at $T = 298$ K, every peak of the Cu_2Se α-phase (PDF Card 47-1448) is present, which is in agreement with previous results on stoichiometric and slightly Cu-deficient Cu_2Se. In the doped samples, there is an additional set of peaks around $2\theta \approx 31.0°$ at 298 K, which is highlighted in the inset of Fig. 3.2(a). These specific Bragg peaks belong to SnSe (PDF Card 14-0159), indicating that a secondary phase exists in the sample. Furthermore, as the Sn dopant level is increased, the intensity of the SnSe peaks increases.

At 473 K, the Cu_2Se α-phase peaks are replaced by the sharper β-phase peaks (PDF Card 46-1129), and some of the Cu_2Se α-phase peaks are lost altogether (e.g., $2\theta \approx 38.8°, 40.4°$ and $61.0°$). Notably, the SnSe peaks around $2\theta \approx 31.0°$ seen at RT in the doped samples have disappeared, meaning that their presence is below the detection limit of the PXRD equipment. At least two factors contribute to this effect. First, the increased thermal motion of the atoms at 473 K decreases the intensity of all diffraction peaks, which is the well-known Debye-Waller effect. Second, the further dissolution of the Sn dopant in the Cu_2Se matrix above the phase transition temperature of approximately 410 K decreases the PXRD signal of the secondary phase. The reported larger cell volume of the high-temperature (HT) phase in Cu_2Se [58] can accommodate a greater amount of the Sn atoms in the interstices. Indeed, as can be seen in Fig. 3.2(b), the main diffraction peak of the doped samples occurs at lower angles than the pure sample, meaning that their crystal structures are expanded by the introduction of Sn. Because Sn^{2+} ions are larger than Cu^{1+} ions (≈ 0.76 Å vs. ≈ 0.60 Å), while Sn^{4+} ions are actually smaller (≈ 0.55 Å) [77, 78], the enlarged lattice parameter suggests the presence of Sn^{2+} ions within the Cu_2Se matrix and not Sn^{4+}. This is an important distinction that will be helpful in understanding the carrier concentration data. In addition, the higher angle of the diffraction peak for $Cu_{1.90}Sn_{0.05}Se$ compared to $Cu_{1.96}Sn_{0.02}Se$ may be explained by Sn replacing small fractions of Se, which has a larger radius of ≈ 1.84 Å in its Se^{2-} valence state [78]. The aforesaid loss of Se during the synthesis of the $Cu_{1.90}Sn_{0.05}Se$ sample and the carrier concentration measurements to be mentioned later (Figure 3.4(c)) are consistent with this hypothesis. Despite the noted peak shifts and absence of secondary phase signals in the HT PXRD patterns, we do not assume full solubility of Sn within the Cu_2Se matrix for the doped samples at high temperatures, especially given the reported low solubility limits of less than 3 at% [76].

Backscattered electron (BSE) images of the x = 0, 0.01, 0.02 and 0.05 samples are shown in Figure 3.3. From Fig. 3.3(a), we notice the featureless single-phase matrix of the pure sample. In Figs. 3.3(b-d), the secondary phase detected in the PXRD patterns for the doped samples can clearly be seen in white. EDX spectroscopy of the secondary phase in the doped samples typically indicated approximately 45 at% each of Sn and Se, confirming the chemical composition to be nearly stoichiometric SnSe. Trace amounts of oxygen, carbon and copper accounted for the remainder of the signal in the EDX spectroscopy, which is only an approximate technique. As shown in Fig. 3.3(b), $Cu_{1.98}Sn_{0.01}Se$ possesses irregularly shaped agglomerations of SnSe with a typical dimension of a few microns and separation distances of a few tens of microns. The more highly doped samples (Figs. 3.3(c) and (d)) have the additional feature of continuous SnSe formations at parts of the grain boundaries of the Cu_2Se main phase. As the dopant level is increased, the agglomerations and grain boundary formations grow in volume fraction.

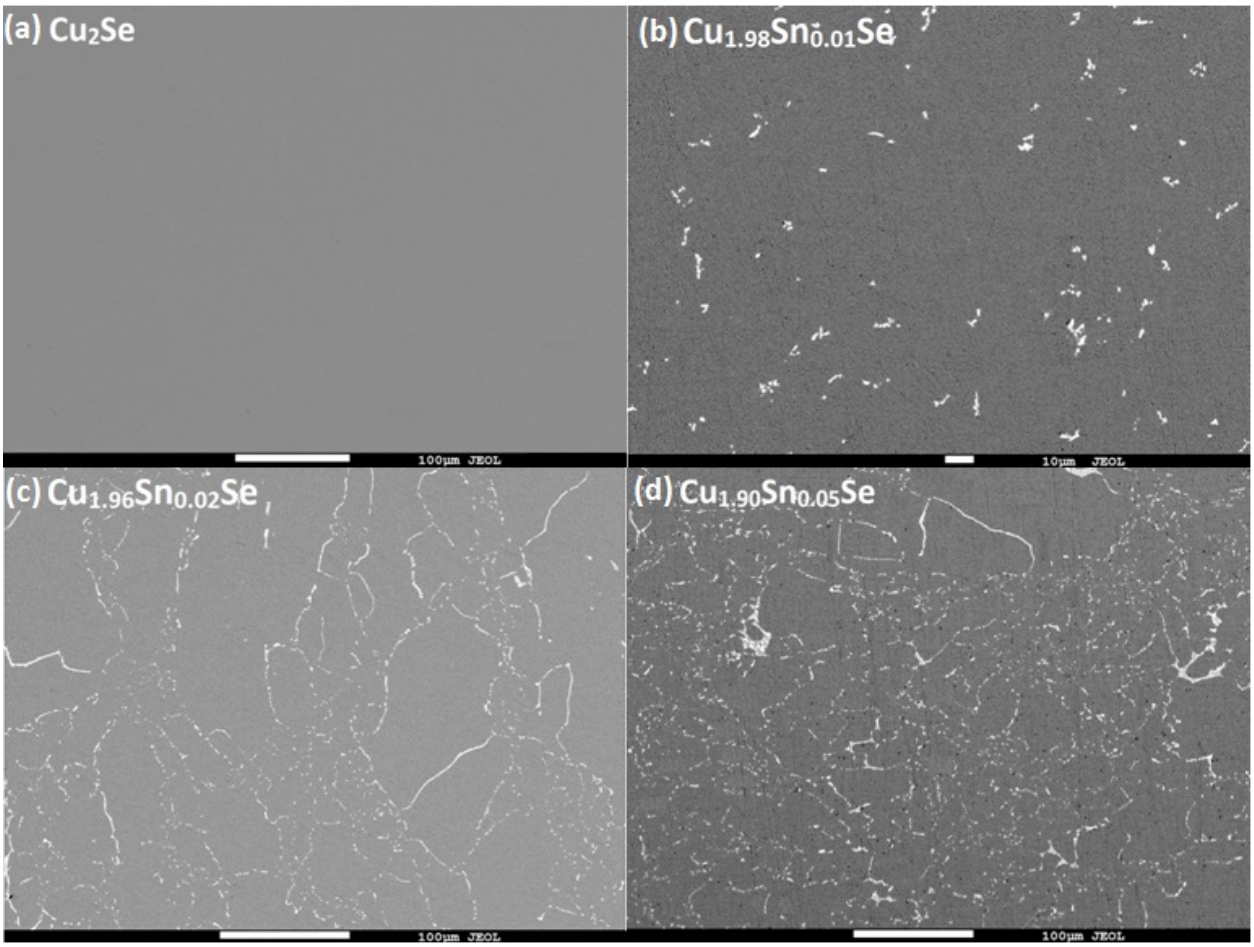

Figure 3.3: **Backscattered electron images of the four $Cu_{2-2x}Sn_xSe$ samples in the study.** (a) Cu_2Se as a single phase, (b) $Cu_{1.98}Sn_{0.01}Se$ with isolated SnSe secondary phase precipitates and (c) $Cu_{1.96}Sn_{0.02}Se$, and (d) $Cu_{1.90}Sn_{0.05}Se$ with more developed networks of the SnSe secondary phase.

3.3 Thermoelectric Properties

3.3.1 Experimental Details

HT electrical property measurements (S and σ) were performed at the Wuhan University of Technology (WHUT) using an ULVAC-RIKO ZEM-3 with 4-point pressure contacts on samples that were approximately 9 mm^2 by 10 mm in length cut perpendicular to the pressing direction. A Netzsch Laser Flash Analysis 457 at WHUT was used for the thermal diffusivity (D) data, with the laser incident on square samples approximately 7.5 mm in width and 1 mm thick cut parallel to the pressing direction. A pyroceram reference sample ensured that the measurement of D was well calibrated over the entire temperature range, and repeated measurements on multiple specimens of the same sample yielded consistent results. In addition, S, σ and D values were confirmed to

within 10% error with measurement equipment at UM. Heat capacity at constant pressure (C_p) measurements were performed at UM using a NETZSCH Differential Scanning Calorimeter Model 404 C with a calibrated Al_2O_3 standard. The thermal conductivity was calculated with the expression $\kappa = \rho D C_p$. HT carrier concentration data was determined by Hall effect measurements with a 1 Tesla field, conducted at UM using a 4-probe AC method with the signal measured by a Linear Research AC Bridge Model LR-700. We assumed a single parabolic band model to extract the carrier concentration, $p = (R_H e)^{-1}$, where R_H is the measured Hall coefficient and $e = 1.602$ x 10^{-19} C is the elementary charge. The hole mobility was calculated as $\mu_H = \sigma R_H$. All HT measurements were performed under inert atmospheres to reduce sample oxidation.

3.3.2 Results and Discussion

The electronic properties of the four samples in this study are displayed in Figure 3.4. All of the curves exhibit a discontinuity around 410 K associated with the phase transition discussed earlier. The data for the pure sample are consistent with previous reports using similar techniques [17, 44, 45, 49, 50, 53]. With increasing temperature, the electrical conductivity of each sample (Fig. 3.4(a)) decreases while the positive Seebeck coefficient (Fig. 3.4(b)) increases, illustrating the typical behavior of a degenerate p-type semiconductor with a single carrier [26]. In general, $Cu_{1.98}Sn_{0.01}Se$ and $Cu_{1.96}Sn_{0.02}Se$ possess slightly diminished σ but enhanced S in comparison to the pure sample, while $Cu_{1.90}Sn_{0.05}Se$ follows the opposite trend: a much enhanced electrical conductivity and diminished Seebeck coefficient. This separation can be explained by the carrier concentration data from our Hall effect measurements (Fig. 3.4(c)), which show the exact same division. We first note that all of the samples exhibit p-type character with carrier concentrations on the order of 10^{20} cm^{-3} that increase with temperature. $Cu_{1.98}Sn_{0.01}Se$ and $Cu_{1.96}Sn_{0.02}Se$ exhibit lower values of the carrier concentration than Cu_2Se, while $Cu_{1.90}Sn_{0.05}Se$ has a distinctly higher value of p.

As noted in previous works on pure Cu_2Se, the intrinsic Cu deficiency of the material removes electrons from the system, resulting in hole (p-type) conduction [17, 81]. In the series of compounds studied here, the PXRD suggests that one Sn^{2+} atom is substituted for two Cu^{1+} atoms, so the hole count of the system should theoretically stay the same. Up to the 2 at% dopant level, the Sn introduced into the compound acts as a n-type dopant potentially by decreasing the native deficiency of Cu in the Cu_2Se matrix, thus reducing the hole count. After the Cu sites become saturated, as suggested by the reported low solubility limit [76], Sn atoms may occupy the Se sites of the matrix, acting as an anionic substitution and contributing two fewer electrons than Se. Such a phenomenon is the most likely cause for the strong p-type dopant behavior seen in $Cu_{1.90}Sn_{0.05}Se$, especially considering the loss of Se during the synthesis of this sample. In ad-

dition, anionic substitution of elements with similar electronegativity differences has been readily achieved in Cu_2Se-based compounds [50, 51, 52]. This explanation is also consistent with the shift of the main diffraction peak of $Cu_{1.90}Sn_{0.05}Se$ to higher angles than that of $Cu_{1.96}Sn_{0.02}Se$, which suggests a reduced lattice constant by the replacement of large Se anions with the smaller Sn.

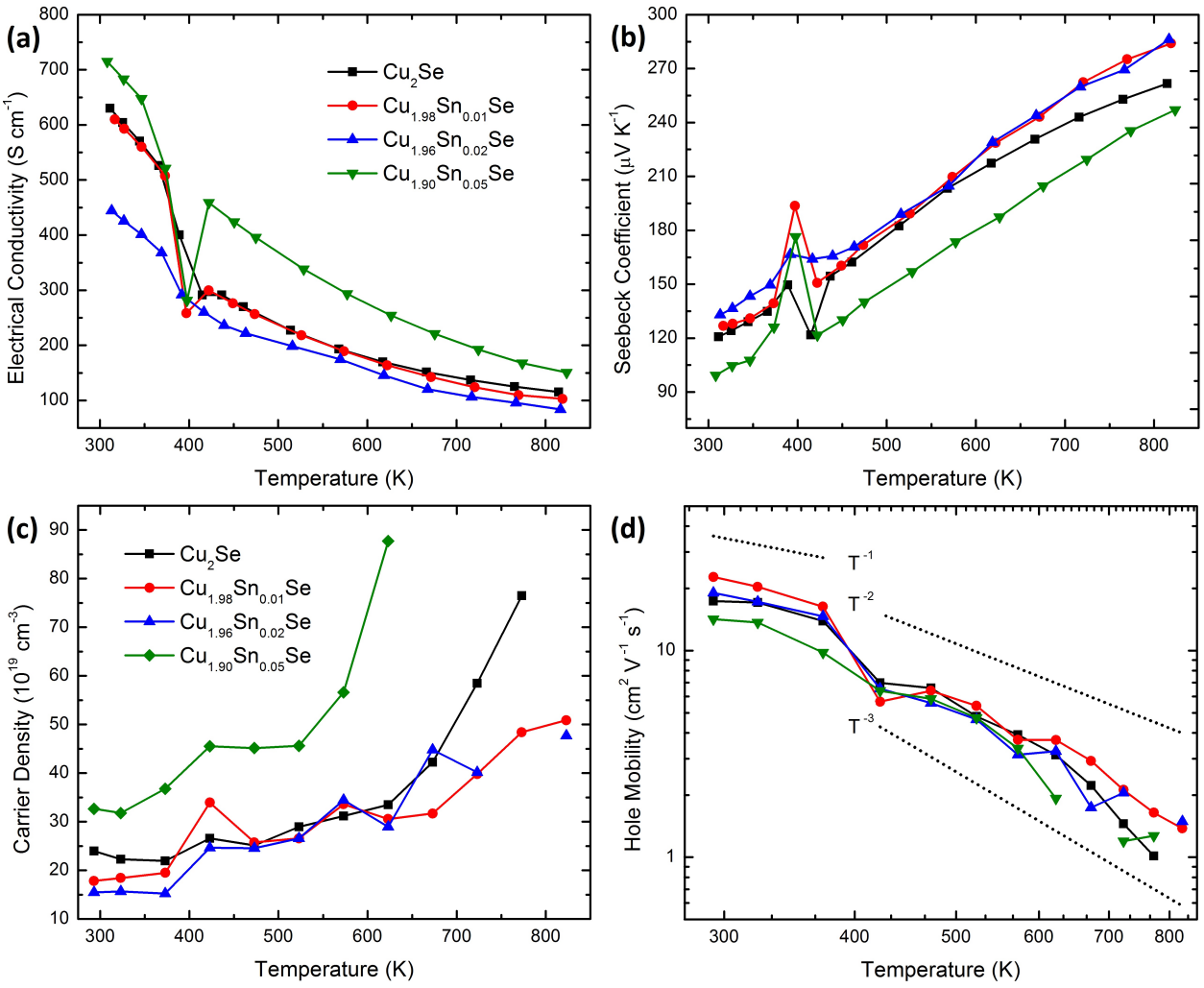

Figure 3.4: **Temperature-dependent electrical properties of $Cu_{2-2x}Sn_xSe$.** The trends of (a) the electrical conductivity and (b) the Seebeck coefficient with respect to the dopant content can be explained by (c) the carrier density calculated from the Hall measurements. (d) shows the hole mobility with dotted lines illustrating different power law slopes to help understand the carrier scattering in the samples. See the text for further discussion.

Using the HT Hall data, we are able to rigorously understand the electronic transport of the materials in the study. Figure 3.4(d) shows the mobility as a function of temperature in a log-log plot in order to extract the exponent ν that describes the dominant charge carrier scattering mechanism, with $\mu_H \propto T^{-\nu}$ [26]. The RT mobilities of the 1 at% and 2 at% doped samples are enhanced in comparison to the pure sample, potentially a result of strain relaxation in the

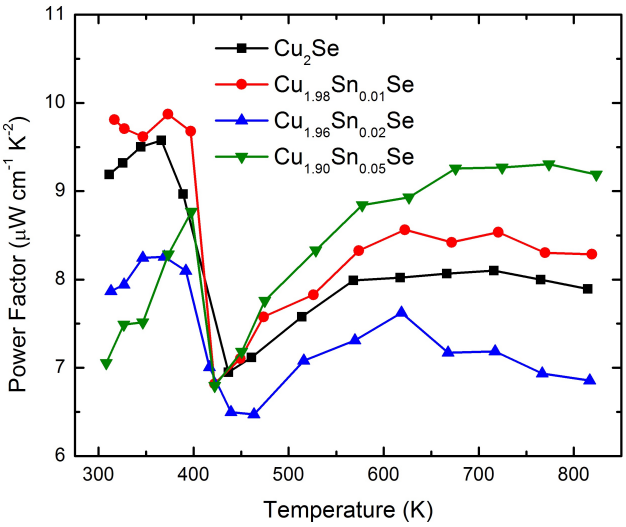

Figure 3.5: **Temperature-dependent power factor of $Cu_{2-2x}Sn_xSe$.**

crystal structure upon small dopant concentrations, which has been seen in other TE materials [82]. $Cu_{1.90}Sn_{0.05}Se$ exhibits reduced RT mobilities most likely due to the increased density of impurities that scatter charge carriers. Below the phase transition, $\nu \approx 1$, indicating that the holes are mainly scattered by acoustic phonons and the carrier effective mass is roughly constant at these temperatures. The mobilities of the samples converge above the phase transition and show reduced values that could be a result of scattering by the disordered Cu ions. The exponent changes to $2 \lessapprox \nu \lessapprox 3$, meaning that acoustic phonon scattering still dominates, but the carrier effective mass is now a growing function of temperature [26].

Combining the electrical conductivity and the Seebeck coefficient, the power factor ($PF = S^2\sigma$) determines how much electricity can be generated by a given temperature gradient. In this study, $Cu_{1.98}Sn_{0.01}Se$ and $Cu_{1.90}Sn_{0.05}Se$ show enhanced PF in comparison to the pure sample (Figure 3.5), with $Cu_{1.90}Sn_{0.05}Se$ possessing the maximum HT value of $PF \approx 9.3$ μW cm^{-1} K^{-2} at 773 K. Unfortunately, $Cu_{1.96}Sn_{0.02}Se$, as a result of its drop in σ without a concomitant rise in S, has a diminished PF with respect to the pure sample. Overall, the electronic properties of the samples are comparable to other excellent TE materials [23].

Figure 3.6(a) presents the thermal conductivity data with the anomalously large $T = 423$ K point near the phase transition removed in order to view the curves on a more clear scale. As expected, the thermal conductivity values for Cu_2Se are quite low, reaching ≈ 0.76 W m^{-1} K^{-1} at 823 K. $Cu_{1.98}Sn_{0.01}Se$ has an even lower thermal conductivity, showing approximately a 10% reduction in comparison to the pure sample above 473 K and reaching a minimum of ≈ 0.69 W m^{-1} K^{-1} at 823 K. $Cu_{1.96}Sn_{0.02}Se$ and $Cu_{1.90}Sn_{0.05}Se$ have larger thermal conductivities than the pure sample, with the magnitude increasing with increasing dopant content and reaching a maximum of ≈ 1.14 W m^{-1} K^{-1} at 823 K for $Cu_{1.90}Sn_{0.05}Se$.

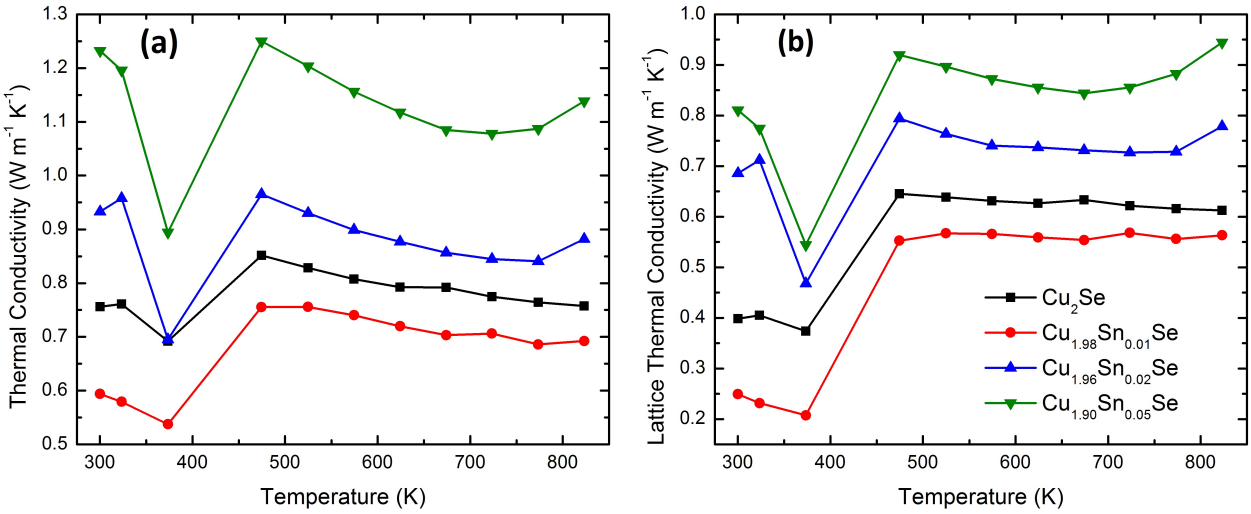

Figure 3.6: **Temperature-dependent thermal conductivities of $Cu_{2-2x}Sn_xSe$.** (a) The total thermal conductivity and (b) the lattice contribution to the thermal conductivity show impressively low values, with the 1 at% Sn-doped sample exhibiting about a 10% reduction in comparison to the pure sample. The data at the α-β phase transition of Cu_2Se seen in all of the samples has been removed from (a) and (b) for the sake of clarity. See the text for the method of calculating the lattice thermal conductivity.

To isolate the lattice contribution to the thermal conductivity, κ_L, we subtracted the electronic contribution, $L\sigma T$, where L is the Lorenz number, from the total thermal conductivity, κ_T, such that $\kappa_L = \kappa_T - L\sigma T$. In order to determine the Lorenz number, we first calculated the reduced Fermi energy, η, by using the experimental Seebeck coefficient data and Eq. 2.29, which is reproduced here:

$$S = \frac{k_B}{q}\left[\frac{\left(r+\frac{5}{2}\right)F_{r+\frac{3}{2}}(\eta)}{\left(r+\frac{3}{2}\right)F_{r+\frac{1}{2}}(\eta)} - \eta\right], \tag{3.1}$$

with the Fermi integrals, $F_n(\eta)$, defined in Eq. 2.18. The experimental S data shown in Fig. 3.4(b) is used as input to Eq. 3.1 while $r = -1/2$ for the acoustic phonon scattering of the holes, as determined from our HT mobility analysis. With η calculated for each sample and temperature, the corresponding Lorenz number is determined by Eq. 2.31, also reproduced here:

$$L = \left(\frac{k_B}{q}\right)^2\left[\frac{\left(r+\frac{7}{2}\right)F_{r+\frac{5}{2}}(\eta)}{\left(r+\frac{3}{2}\right)F_{r+\frac{1}{2}}(\eta)} - \frac{\left(r+\frac{5}{2}\right)^2F^2_{r+\frac{3}{2}}(\eta)}{\left(r+\frac{3}{2}\right)^2F^2_{r+\frac{1}{2}}(\eta)}\right]. \tag{3.2}$$

The values of the Lorenz numbers were on a range of (1.5-1.9) x 10^{-8} V^2 K^{-2}, with the smaller values occurring at high temperature. Across samples, the Lorenz numbers followed the same trend as the carrier concentration, decreasing from the pure sample to the 2 at% dopant level and increasing thereafter. The variation of the Lorenz numbers with temperature and dopant concen-

tration is an important finding that is necessary in rigorously calculating κ_L to isolate it from the heat flow associated with the charge carriers. Figure 3.6(b) shows the resulting lattice thermal conductivity.

In comparison to the pure sample, the 1 at% Sn-doped sample possesses a lattice thermal conductivity reduced by approximately 10%, while the 2 at% and 5 at% doped samples show larger values. In all of the samples, atomic mass and strain fluctuations in the matrix must lead to greater phonon scattering [2]. With $m_{Cu} = 63.55$ amu and $m_{Sn} = 118.71$ amu, the heavier Sn atoms in the Cu_2Se phase act as point defects to scatter high frequency phonons. What ultimately distinguish the samples are their microstructures. For the 1 at% doped sample, the isolated micron-size secondary phase (Fig. 3.3(b)) scatters lower frequency phonons [2] that travel unimpeded in the pure sample, resulting in the reduced lattice thermal conductivity. For the more highly doped samples, the developed network of the SnSe secondary phase decorates parts of the grain boundaries of the Cu_2Se matrix (Figs. 3.3(c) and (d)) that already play a role in scattering phonons. With its well-known low thermal conductivity [20, 83], SnSe as a secondary phase cannot act as a thermal short. Thus, in order for the SnSe secondary phase to increase the lattice thermal conductivity, the SnSe lining parts of the Cu_2Se grains must in fact reduce the reflection of phonons at the grain boundaries in comparison to that which occurs between two neighboring Cu_2Se grains. As a result, the developed networks of SnSe create a smoother passage for heat to flow. To rigorously determine the effects of the Sn dopant on the lattice dynamics, inelastic neutron scattering studies would have to be performed to obtain the phonon density of states and dispersion relations [84].

One final observation to consider regarding the lattice thermal conductivity is the upturn of the values for $Cu_{1.96}Sn_{0.02}Se$ and $Cu_{1.90}Sn_{0.05}Se$ at 723 K and 623 K, respectively. Normally, a rising κ_L at high temperatures would indicate bipolar conduction, where intrinsically generated charge carriers begin to significantly add to the lattice thermal conductivity [2]. The carrier density data in Fig. 3.4(c) indicate that a rise in n occurs at lower temperatures in $Cu_{1.90}Sn_{0.05}Se$ compared to the other samples. The corresponding generation of intrinsic carriers at lower temperatures is then reflected in the bipolar conduction that is seen most readily in $Cu_{1.90}Sn_{0.05}Se$.

Using the expression $zT = S^2\sigma\kappa^{-1}T = PFT\kappa^{-1}$, we calculated the TE Figure of Merit, and the results are shown in Figure 3.7. Except at the phase transition, all of the samples have increasing zT with increasing temperature. With a slightly increased power factor (Fig. 3.5) and reduced thermal conductivity (Fig. 3.6(a)), $Cu_{1.98}Sn_{0.01}Se$ averages a 15% enhancement in the TE figure of merit compared to the pure sample over the broad temperature range of 473 K – 823 K. The more highly doped samples do not possess the optimal combination of electrical and thermal properties to show an enhanced zT. It is interesting to note that Liu *et al.* found the maximum zT values to occur in the Cu_2Se sample containing 3 mol% SnSe [79]. The distinct optimized dopant levels are most likely due to the different synthesis techniques, which indeed resulted in unique

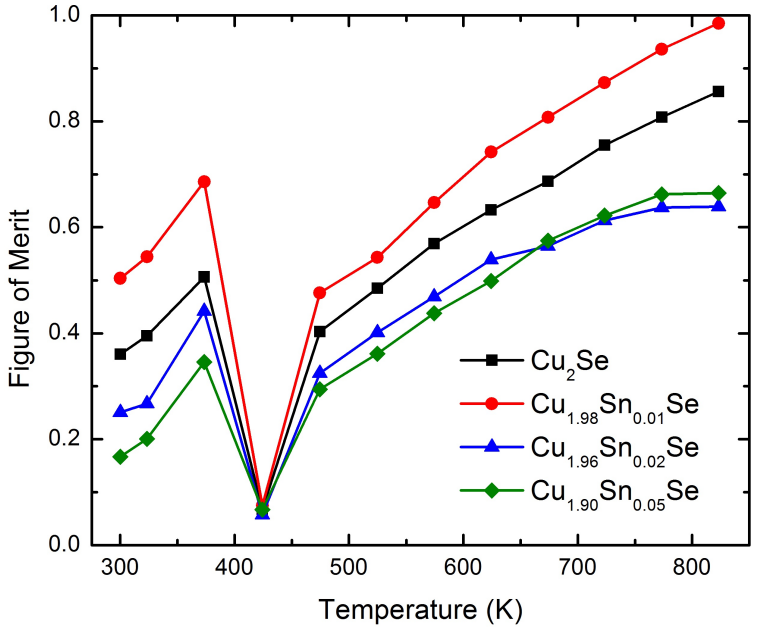

Figure 3.7: **The thermoelectric figure of merit, zT, of the $Cu_{2-2x}Sn_xSe$ samples.** The 1 at% Sn-doped sample possesses 15% enhanced values above 423 K compared to the pure sample.

microstructures and consequently varied TE properties. Overall, to further increase the figure of merit of these compounds, nanostructuring could be a viable technique, as evidenced by previous works [45, 47, 48, 53, 54].

3.4 Current Stress Test

3.4.1 Experimental Details

In order to test the ability of the samples to withstand typical TE generator conditions, we altered the homemade setup normally used for the measurement of S and σ at UM so that greater currents could be passed through the samples. We were guided by the works of Brown *et al.* [70] and Dennler *et al.* [71]. A schematic of a general current stress test is shown in Figure 3.8, while a photograph of our experimental setup is given in Figure 3.9(a). Half-cylinder samples of 1/2" diameter and 2 mm thickness were mounted on a stainless steel block that was placed in a graphite holder, and a stainless steel cap was attached to the top of the sample. Surrounding the graphite holder slightly below the sample is a simple heater of coiled stainless steel wire used to establish a temperature gradient across the sample in attempt to emulate the conditions of TE power generation. Type R thermocouples using Pt and a Pt/Rh alloy were attached to the sample and registered a ΔT of approximately 50 K during the test. The entire unit was placed in a furnace in a closed chamber equipped with electrical feedthroughs. Copper wires attached to the stainless steel

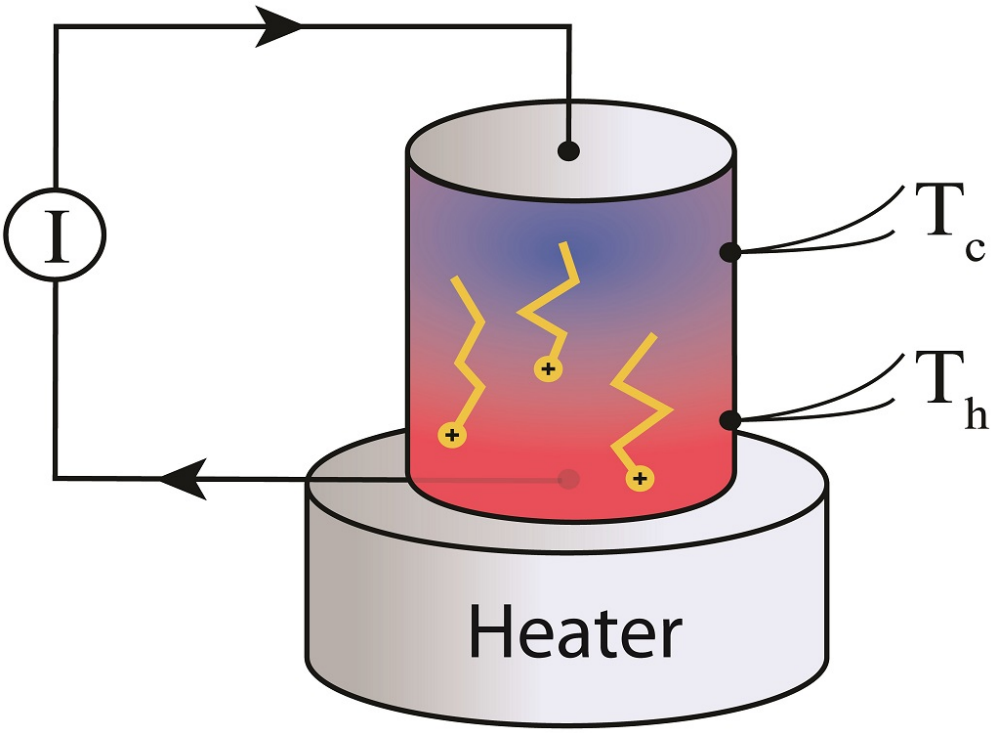

Figure 3.8: **Schematic of a current stress test emulating thermoelectric power generation conditions.** Electrical contacts on the sample allow for several amperes of current to pass continuously through the material while it is held at the desired temperature of operation. Thermocouples attached to the sample measure the temperature gradient along its length, with the hot end established by the heater below the sample. The cations in the material (shown as yellow filled circles with + signs in the middle) are electrically forced to the bottom and build up as solid precipitates if the material is structurally, and consequently, electrically unstable.

cap and block were connected to an external power supply run in constant current mode. During the current stress test, approximately 8 A of current was passed through the samples continuously for 24 hours while the furnace temperature was held at 773 K. The current density amounted to $\approx$ 12 A cm^{-2}, a typical maximum operating condition found in TE generators [71]. The direction of the current opposed the thermal gradient in order to rule out the migration of the copper ions by thermal diffusion. An argon atmosphere within the chamber helped to slow down sample oxidation.

Visual observation of the samples after the current stress test is a way of immediately identifying the chemical stability of the samples. In addition, we used SEM images to view surface changes of the samples under high magnification, as well as backscattered electron (BSE) images to observe microstructural changes as a result of the current stress test. To determine the elemental buildups on the surfaces of the samples after the test, we performed Auger spectroscopy (Physical Electronics Auger Nanoprobe 680). As a means of quantifying the material degradation of

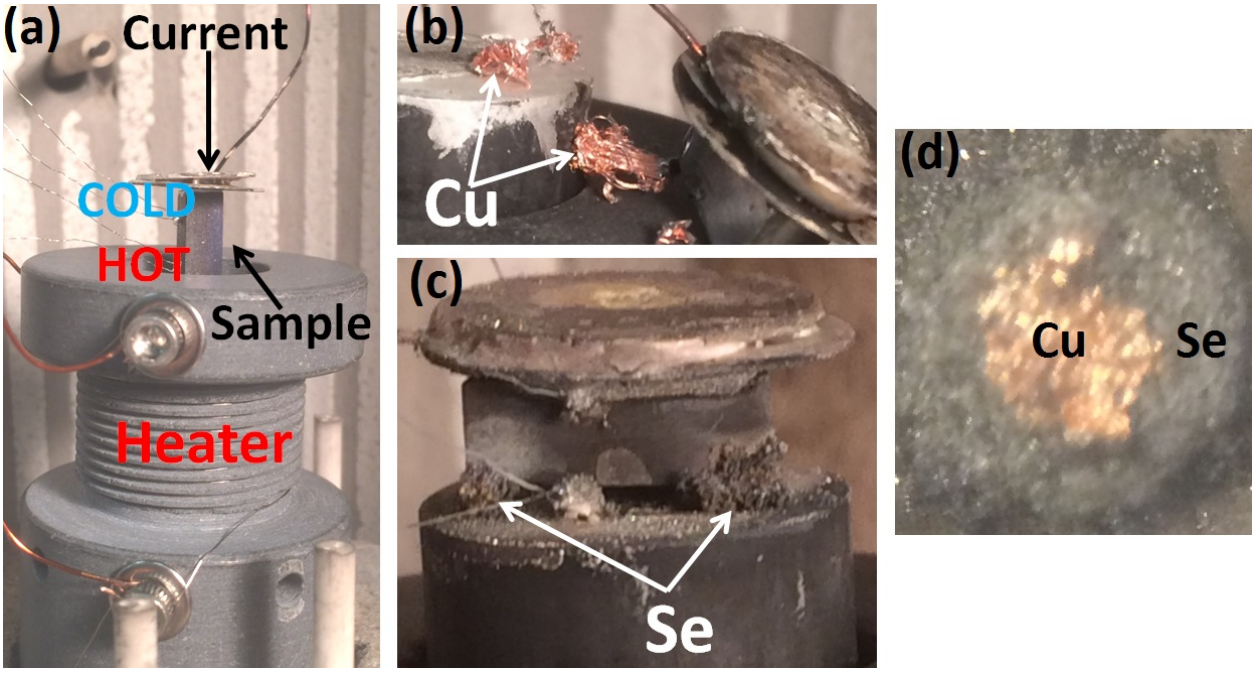

Figure 3.9: **Experimental setup and results of the current stress test performed for $Cu_{2-2x}Sn_xSe$.** The graphite holder with the sample and electrical attachments is shown in (a) with the current direction against the direction of thermal diffusion. Cu ribbons (b) and selenium granules (c) form at the hot end of the samples, as verified by Auger spectroscopy, with Se often surrounding the Cu (d).

the samples, we measured the density before and after the current stress test. Because the main component of the material degradation is the loss of solid copper, which has a larger density than the samples (≈ 9.0 g cm^{-3} vs. ≈ 6.8 g cm^{-3}), we expected the density of the samples to decrease when the copper was expelled.

3.4.2 Results and Discussion

Images of the pure sample and the 5 at% Sn-doped sample after the current stress test are shown in Fig. 3.9(b) and (c), respectively. Two distinct elemental buildups on the bottoms of the samples are evident. First, as illustrated by the pure sample in Fig. 3.9(b), ribbons of copper were expelled at the hot end of the sample, and, second, as evidenced by the 5 at% Sn-doped sample in Fig. 3.9(c), selenium granules also developed at the hot side. Due to its high ionic conductivity and ability to flow between tetrahedral sites within the Cu_2Se matrix, the Cu ions move towards the hot end of the sample by electrical forcing. Once a large enough concentration of Cu is built up at the hot side, most of the Se atoms are pushed away as the solid Cu is forced out. The selenium often builds up in a region surrounding the solid copper precipitate, as shown in Fig. 3.9(d), in a combination of its pure state and reacted states with Cu, according to Auger spectroscopy. The

pure Se, with a melting point of 494 K [85], would be molten at 773 K. As the furnace is cooled to room temperature following the experiment, the selenium crystallizes as granules that collect at the hot side.

In addition to the Se and Cu signals in the Auger spectroscopy, we noticed a small signal from Fe within the selenium granules, indicating that the selenium deposits at the bottom of the sample reacted with the stainless steel block below it. Such chemical reactions with contacts are known to lead to increased contact resistance that is deleterious to device performance [46, 68, 70]. One final byproduct of the material degradation tests for the doped samples were small particles composed of tin oxides. Because no unreacted pure tin was detected in the doped samples by SEM before the current stress test, the possible sources of the tin in the tin oxides are the secondary phase of SnSe and the Sn within the Cu_2Se main phase.

Unfortunately, the current stress test causes material degradation in all of the samples, meaning that the tin dopant does not cure the issue of chemical stability found in these Cu_2Se-based compounds. After the current stress test, the hot ends of the samples were extensively deformed, often revealing the fractured surface, as shown in the SEM image of Cu_2Se in Figure 3.10(a). All of the samples featured holes at the hot ends where the copper was expelled. The holes ranged in size from tens of microns to several hundreds of microns, which is illustrated by the SEM image of $Cu_{1.90}Sn_{0.05}Se$ in Fig. 3.10(b) and the BSE image of the same sample in Fig. 3.10(c). In addition, the secondary phase of the doped samples appeared to be reduced slightly in volume fraction and was altered in shape after the current stress test, as evidenced by the BSE image of $Cu_{1.90}Sn_{0.05}Se$ in Fig. 3.10(c). Unfortunately, we cannot make a comparison of the bulk compositions of the samples due to the EDX signal being polluted by multiple oxides and elements involved in the electrical contacts of the experiment, which renders the data unmeaningful.

We did notice visually that the amount of Cu and Se leaving the samples during the current stress test did diminish with the higher doping content. To confirm this quantitatively, we assessed the density change of the samples during the current stress test, the results of which are shown in Fig. 3.10(d). As expected, due to the mass loss primarily from copper, the density, ρ, of the pure sample was reduced during the current stress test, by approximately 4%. With increasing dopant content, the percent density loss decreased, with the minimum of 2% density loss achieved for $Cu_{1.90}Sn_{0.05}Se$. The error bars attached to the data points in Figure 3.10(d) are calculated by adding the error sources of the density calculation in quadrature. Specifically, for a single density measurement, $\rho = \frac{m}{V} \pm \delta\rho$, of a mass $m \pm \delta m$ of volume $V \pm \delta V$, the relative error is

$$\frac{\delta\rho}{\rho} = \frac{1}{\rho}\sqrt{\left(\frac{\partial\rho}{\partial m}\delta m\right)^2 + \left(\frac{\partial\rho}{\partial V}\delta V\right)^2} = \frac{1}{\rho}\sqrt{\left(\frac{\delta m}{V}\right)^2 + \left(\frac{m\,\delta V}{V^2}\right)^2}$$

$$= \sqrt{\left(\frac{\delta m}{m}\right)^2 + \left(\frac{\delta V}{V}\right)^2}, \tag{3.3}$$

demonstrating that the relative errors in the individual inputs (m and V) contribute equivalently.

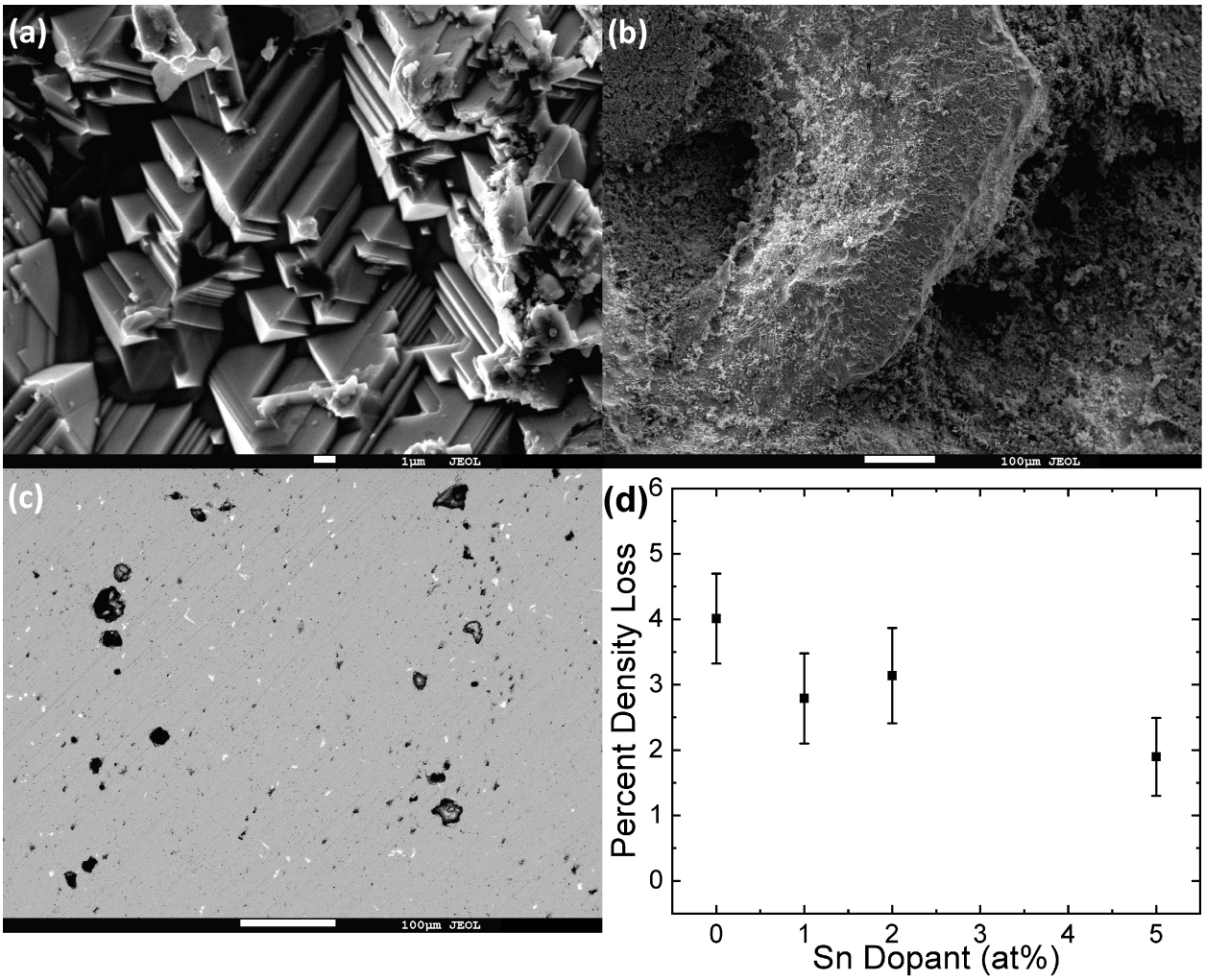

Figure 3.10: **Surface, microstructure, and material loss assessment of the $Cu_{2-2x}Sn_xSe$ samples after the current stress test.** The material degradation of the samples often unveiled the micron-sized crystallites of the fractured surface (a, Cu_2Se). Holes on the surface were common for all of the samples and ranged in size (b and c, $Cu_{1.90}Sn_{0.05}Se$). BSE revealed an altered microstructure (white dots) in the doped samples (c, $Cu_{1.90}Sn_{0.05}Se$) as well as holes (black spots). The percent density loss as a function of the Sn dopant (d) indicates that the material degradation decreases with higher Sn content. The error bars are calculated following Eq. 3.3 described in the text.

For measuring the density loss incurred through the electromigration experiment (current stress test), two separate measurements before and after the experiment are performed, and the relative errors in each are also added in quadrature. In general, the relative error in the mass of several gram

samples is less than 1%, while the relative error in the volume can be 10% or more due to the small sample size. A separate quantitative method that we did not pursue in this study is described in Ref. [74]. The method involves measuring the electrical conductivity of the samples within the current stress test as a function of time. Because the expulsion of Cu from the compounds increases the number of holes contributing to the electronic conduction, the σ of pure Cu_2Se measured during the electromigration experiment should increase over time, t. An electrically stable compound would exhibit a nearly constant σ vs. t if assessed for several days with fine increments ($\approx$ 1 minute), as long as there is no other form of material degradation, such as oxidation. Of course, the proper current density must be applied in keeping with the emulation of TE application conditions.

We propose two potential reasons for the decreased material degradation with the introduction of larger amounts of tin in the materials (Fig. 3.10). First, as discussed before, the tin atoms getting into the Cu_2Se matrix may act as physical and electrical barriers due to their size and charge difference in comparison to the copper atoms. As point defects within the matrix, Sn can distort the long-range pathway for the Cu electromigration in a similar manner as Fe dopants in Cu_2S [74], thereby diminishing the solid Cu expulsion. Second, the secondary phases of SnSe that form at the grain boundaries of the Cu_2Se main phase may hinder the transit of Cu ions. As the Sn dopant content increases, the volume fraction of the SnSe secondary phase increases, as seen in the PXRD peaks (Fig. 3.2(a)) and the BSE images (Fig. 3.3), which may contribute to the decreased material degradation we see at higher dopant values.

In order to stabilize the Cu_2Se-based compounds, more work must be done to prevent the electromigration of the Cu ions. Following a dopant approach with larger ionic radii elements, such as Na and Ca, or multi-valent atoms, such as Fe or Cr, may prove successful, but the exact solubilities of these elements within the Cu_2Se matrix will play a big role. Work on the tetrahedrite $Cu_{12}Sb_4S_{13}$ has shown increased phase stability with Ni substitution [86], while introducing Fe into Cu_2S results in the bornite structure that is more robust under current stress [74]; potentially the same dopants could help the chemical stability of Cu_2Se due to its similar chemical constituents and atomic coordinations. An alternative strategy could be to overdope the matrix, creating compounds of the form Cu_2A_xSe, where the dopant element A could possibly fit into the vacant interstices of Cu_2Se, thereby trapping the Cu ions. Yet, the question remains whether preventing the electromigration of the Cu ions, whose kinetic disorder is a contributing factor to the extremely low thermal conductivity, might actually deteriorate the TE properties of the material. It is possible that Cu_2Se-based compounds, due to their superionic nature, cannot simultaneously possess superior TE properties and remain chemically stable in TE applications. Further investigations are necessary to study this relationship more thoroughly.

3.5 Conclusions

We have reported here the $Cu_{2-2x}Sn_xSe$ (x = 0, 0.01, 0.02 and 0.05) series of compounds that exhibit maximum TE performance for the 1 at% Sn-doped sample. Its unique microstructure and inherent point defect scattering of phonons resulted in a 10% reduction of the lattice thermal conductivity. With an increased power factor, $Cu_{1.98}Sn_{0.01}Se$ demonstrated an enhancement of zT averaging 15% over the broad temperature range of 473 K – 823 K.

In current stress tests designed to emulate the typical operating conditions of TE power generation, the material degradation of the samples decreased with increasing dopant content, as judged by the density loss of the samples during the test. The Sn atoms, acting within the matrix and as a secondary phase, contribute to the decreased material degradation. Yet, because the issues of copper expulsion and selenium precipitation still exist at the 5% dopant level, these compounds are not viable for applications. Pursuing other dopant elements that have shown success in rendering similar systems robust against degradation is one approach for potentially resolving the electromigration issue. However, it is possible that stabilizing Cu_2Se-based compounds may actually eliminate the liquid-like lattice that endows them with superior TE properties. We wish to emphasize that all TE studies of Cu_2Se and other SICs should perform current stress tests in addition to the standard TE property measurements, in order to check the electrical stability of the materials in TE operating conditions. The overarching goal of TE research, which is to benefit society and the environment through the economic and safe utilization of waste heat, can only be realized in these Cu-based materials if they remain robust in applications.

3.6 Latest Results and Future Work

The above work was published in Ref. [73], and a follow-up review article in Ref. [72] surveyed the literature for a broader range of SICs, including Cu_2S, Ag_2Se, MgAgSb, Zn_4Sb_3, and others. As of April 2020, the research article [73] has approximately 35 citations, while the review article [72] has about 15. Instances of current stress tests were quite rare in the literature regarding SIC TEs, numbering about 5 or so [70, 71, 73, 74, 87] compared to 100s of related publications simply reporting zT values. Standard TE measurements are usually carried out with electrical currents on the order of 10-100 mA applied momentarily, whereas the current stress tests require multiple amperes for hours and days. Because most groups conducting TE property measurements utilize commercial equipment, it can be a challenge for them to develop more prolonged tests that emulate real-world TE power generation conditions. In the past three years, many works have considered the issue of electrical stability more thoroughly. We highlight a few of those works here.

A collaborative study initiated by Professor Poudeu at UM, and led by his then-graduate stu-

dent Dr. Alan Olvera [88], found that zT values up to 2.6 at 850 K can be achieved in Cu_2Se by incorporating just 1 mol% of $CuInSe_2$ to create a nanocomposite, as shown in Figure 3.11(a). One of the major breakthroughs of the study was that the zT values at lower temperatures for the Cu_2Se-$CuInSe_2$ samples were all enhanced to much larger values than any other Cu_2Se-based systems. At lower temperatures, the issue of material degradation in Cu_2Se is less of an issue, albeit still prevalent, so the Cu_2Se-$CuInSe_2$ are attractive candidates for TE applications. Indeed, the homebuilt current stress test performed by Olvera demonstrated no visible degradation nor copper extrusion from the Cu_2Se-1mol%$CuInSe_2$ sample. The reference Cu_2Se sample shed multiple Cu wires at the negative electrode when run through the same current stress test. The authors surmised that the dissolution of the In within the Cu_2Se structure, in addition to the nanoscale secondary phase of $CuInSe_2$, both act as physical and electrical barriers to slow the migration of the Cu ions in the presence of an electric field. Surprisingly, the enhanced electrical stability of the Cu_2Se-1mol%$CuInSe_2$ did not increase the thermal conductivity. Rather, the Cu_2Se-1mol%$CuInSe_2$ sample maintains values of κ near 0.4 W m^{-1} K^{-1} above 600 K, while the pure Cu_2Se hosts values that are double that. Thus, the study provided a case in which nanocompositing not only enhanced the zT values, but also helped to stabilize the Cu_2Se-based compounds.

Additional work by Qiu *et al*. [89] examined the chemical potential of the Cu^{1+} ions in a mixed ionic-electronic conduction model to understand the critical applied voltage, V_a, at which Cu metal deposition occurs in a TE device. They found that the applied voltage is the determining factor for electrical stability, not the current density, $\mathscr{J}$, according to thermodynamics. The current density that runs through a material leg in TE operating conditions sets up an associated voltage across the length of the material, and that voltage must be kept underneath the critical voltage, V_c, for electrical stability of the ions. To satisfy $V_a < V_c$, the authors developed segmented $Cu_{1.97}S$ legs (Cu_2S actually has a greater issue with electrical stability compared to Cu_2Se), with two conductive carbon layers inserted equidistant along the sample bar, as shown in Fig. 3.11(c) and (d). The stable carbon layers allow for electronic conduction but block ion migration. Due to the series arrangement of the heterogeneous leg, the voltage across the individual segments of $Cu_{1.97}S$ is cut to a third of the value for an unsegmented leg, given a constant current density. Thus, the three-segment bar of material allows for higher current densities closer to real TE operating conditions without Cu metal deposition. The authors experimentally demonstrated the electrical stability of the $Cu_{1.97}S$ segmented sample at $\mathscr{J} \approx 30$ A cm^{-2} for periods of ten minutes (Fig. 3.11(c)). However, when a 373 K temperature gradient was applied to the material, the maximum current density possible before Cu deposition shrank to ≈ 3 A cm^{-2} (Fig. 3.11(d)). Evidently, further segmentation is essential for stabilizing the material for TE application conditions, and more prolonged testing is needed. Nevertheless, the segmentation approach developed by Qiu *et al*. [89] should be applicable to a wide range of superionic conductors.

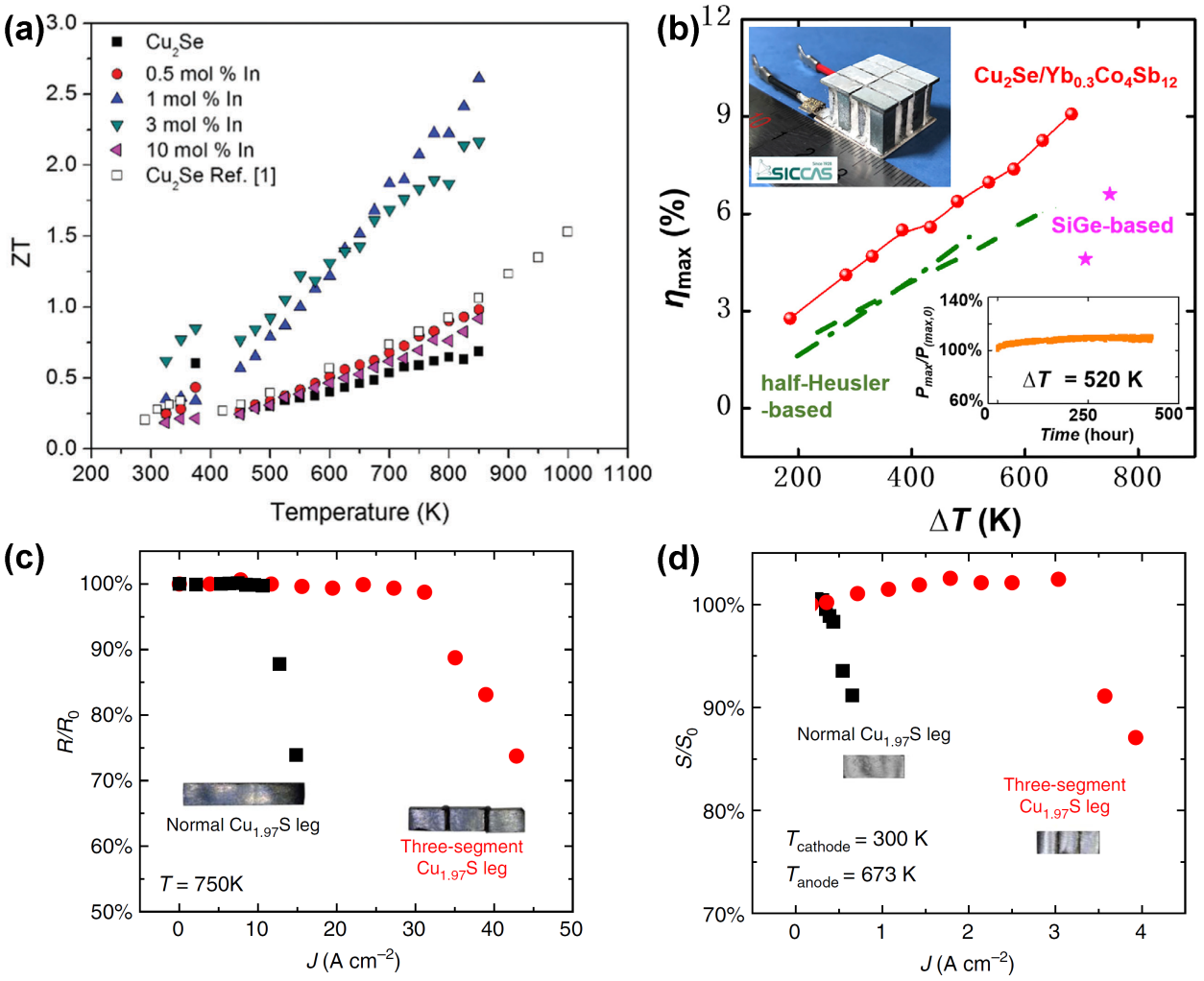

Figure 3.11: **Recent results in thermoelectrics research on superionic conductors.** (a) Temperature-dependent zT values for the Cu_2Se-$x$$CuInSe_2$ composites studied in Ref. [88]. The enhanced zT over the whole temperature range compared to the pure Cu_2Se samples, and the electrical stability witnessed in the current stress test, bode well for applications. (b) Eight-couple $Cu_2Se/Yb_{0.3}Co_4Sb_{12}$ module and maximum efficiency, η_{max}, as a function of the temperature gradient across the device, ΔT. Modified from Ref. [90] with permission from Elsevier. The long-term stability of the power, P_{max}, suggests that the device could operate reliably in real-world TE power generation conditions and compete with other TE materials. (c) Relative resistance, R/R_0, and (d) relative Seebeck coefficient, S/S_0, measured at different applied current densities, J, for a homogeneous $Cu_{1.97}S$ bar and a segmented equivalent [89]. The segmented leg reduces the local voltage such that Cu metal deposition only becomes a major issue at larger current densities compared to the unsegmented equivalent.

Follow-up work by the same group (Ref. [90]) assembled a TE module of p-type Cu_2Se legs with the n-type counterparts being the filled skutterudite $Yb_{0.3}Co_4Sb_{12}$ (Fig. 3.11(b)). The more complicated electrical circuit compared to the previous work (Ref. [89]) results in an expression for V_a that includes the cross-sectional areas of the p- and n-type legs, as well as their individual

Seebeck coefficients and electrical conductivities. By tuning the ratio of the cross-sectional areas, A_p/A_n, the stability condition of $V_a < V_c$ could theoretically be met in the Cu_2Se side of the TE device for a variety of ΔT applicable to real-world power generation conditions. No leg segmentation is required in this approach. Using $A_p/A_n = 4$, the group constructed an eight-couple $Cu_2Se/Yb_{0.3}Co_4Sb_{12}$ module and measured a heat-to-electricity conversion efficiency of $\eta \approx 9\%$ with the cold side of the device held at room temperature and $T_h = 973$ K, i.e. $\Delta T = 680$ K. Long-term aging tests with $\Delta T = 520$ K (to maintain $T_h = 823$ K so that the Sb in the skutterudite leg did not sublimate) displayed $\eta \approx 7\%$ and a continuous power output for 420 hours (Fig. 3.11(b)) without any noticeable degradation in the device construction. The study therefore demonstrates that Cu_2Se can be used as one leg of a couple in a robust TE device with sufficient conversion efficiencies at low cost.

CHAPTER 4

Mictomagnetic Full-Heusler Nanoprecipitates in (Ti, Zr, Hf)$NiFe_xSn$ Half-Heusler Composites

4.1 Motivation: Half-Heusler Composites as Magnetic Thermoelectric Materials

Half-Heusler (HH) compounds are a diverse group of materials that crystallize as cubic structures with chemical formula XYZ, where X and Y are transition metals, such as Ti, Nb, Co, etc., and Z is an s-p element, such as Ge, Sn, Sb, etc. [91]. Due to the large number of stable elemental combinations, HH materials exhibit a wide range of physical phenomena that has spurred on intense research in the areas of topological materials [92], spintronics [93, 94] and thermoelectrics (TEs) [95, 96]. Specifically, TE devices are a low-maintenance, solid-state technology capable of turning temperature gradients into usable electricity [2]. Utilizing the waste heat omnipresent in industrial processes and automobiles, TE devices can generate electrical power for both economical and environmental benefits. Considering the current concern about climate change and fossil fuel usage, the development of TE devices as an alternative energy source is critical [97].

Recently, we synthesized a set of HH composites, $Ti_{0.25}Zr_{0.25}Hf_{0.50}NiFe_xSn_{0.975}Sb_{0.025}$ (TZHNSS), for high-temperature (HT) TE applications [98]. More favorable than simple XYZ compounds, the composites have dramatically reduced thermal conductivities ($\kappa \approx 5$ $Wm^{-1}K^{-1}$ at 300 K for the $x = 0.05$ sample compared to $\kappa \approx 15$ $Wm^{-1}K^{-1}$ at 300 K for HfNiSn [99]). The native phase separation and disorder that occurs when exceeding the solubility limit of the X and Y sites are the sources of the smaller κ, as exemplified in a number of HH systems [100, 101, 102, 103, 104, 105, 106]. Unique to the Fe-added TZHNSS samples, the full-Heusler (FH) XY_2Z secondary phase resulting from the purposefully overstoichiometric Y site is actually magnetic and results in the samples being ferromagnetic until $T_C \approx 650$ K. The interaction of the charge carriers with the magnetic $TiNi_{4/3}Fe_{2/3}Sn$ nanoinclusions aids in maintaining a respectful power factor [98], $PF = S^2\sigma$, where σ is the electrical conductivity and S is the Seebeck coefficient. Overall,

the $x = 0.05$ sample of the TZHNSS composites displayed a 30% improvement in the dimensionless TE figure of merit, $zT = PFT/\kappa$, a direct measure of the heat-to-electricity conversion efficiency.

The utilization of magnetic dopants to simultaneously reduce κ and enhance PF to maximize zT has lately been applied to several families of TE materials [107, 108, 109, 110, 111, 112, 113]. In order to make further improvements in magnetically doped TE materials and spread the technique to heretofore unexplored classes, it is essential to understand the magnetic phenomena present within the compounds. Having shown the benefits of the magnetic FH nanoprecipitates to the HT TE performance of the TZHNSS composite, we here investigate the low-temperature (LT) properties of the compounds, including the DC magnetization, the AC susceptibility and the magnetotransport. We find that the $TiNi_{4/3}Fe_{2/3}Sn$ secondary phase in the Fe-added samples imbues them with long-range magnetic order that displays itself in magnetization hysteresis and a bifurcation of the zero-field-cooled (ZFC) and field-cooled (FC) DC magnetization over the whole temperature range of the study. With the greatest population density of magnetic $TiNi_{4/3}Fe_{2/3}Sn$ nanoparticles, the $x = 0.05$ sample features the largest magnetic moments and a strong superparamagnetic signal with a distribution of blocking (moment freezing) temperatures around $T_f \approx 175$ K. The metallic electrical resistivity of the Fe-added samples contains an upturn near 25 K that we attribute to enhanced magnetic scattering of itinerant charge carriers, i.e. the Kondo effect. Last, we demonstrate the presence of weak anti-localization in the pure TZHNSS sample at temperatures below 4 K, which is significantly suppressed by the ferromagnetism in the Fe-added composites. In total, our work is a careful investigation of the magnetic phenomena that occur in some of the newest TE materials.

4.2 Experimental Methods

A series of $Ti_{0.25}Zr_{0.25}Hf_{0.50}NiFe_xSn_{0.975}Sb_{0.025}$ (TZHNSS) polycrystalline samples, with x = 0, 0.02, 0.05, 0.075 and 0.10, was synthesized following the procedure in Ref. [98]. The fully dense pellets were polished and sectioned into the geometries required for measurements of the DC magnetization, AC susceptibility and magnetotransport properties. Throughout the text and figures, we commonly refer to the HH samples individually as "HH#", where # is the atomic percentage of Fe included in the compound. For example, "HH0" and "HH5" refer to the pure and 5 at% Fe-added TZHNSS samples, respectively.

A Quantum Design Physical Property Measurement System (PPMS) Dynacool model equipped with a 14 Tesla magnet was used for all magnetization and magnetotransport property measurements from 2 to 350 K. For the DC magnetization studies, powder samples of approximately 80 mg were identically encapsulated and oscillated within the Vibrating Sample Magnetometer (VSM) of

the PPMS. To examine the ZFC magnetic moments, each sample was cooled to 2 K without an applied magnetic field, then a 100 Oe (0.01 T) DC field was applied, and the sample was heated to 300 K while measuring the magnetic moment. The samples were subsequently cooled from 300 K to 2 K with an applied field of 100 Oe, then the temperature-dependent FC magnetic moments were measured while warming back to room temperature. Isothermal magnetization curves up to an applied field of 140 kOe were recorded at a variety of temperatures to determine the diamagnetic, paramagnetic and ferromagnetic nature of the samples. AC susceptibility measurements (PPMS ACMS option) were performed for the $x = 0.05$ sample using a bulk chunk of approximately 150 mg mounted on a quartz paddle with varnish. The small background magnetic signal from the quartz paddle was recorded in a separate measurement and subtracted off the raw sample data to yield that presented here. Temperature scans focused on the blocking phenomena in the 100 to 350 K range and utilized an AC drive field of $H_{ac} = 5$ Oe. A number of drive field frequencies, ω, and background magnetic fields, H_{dc}, were implemented to assess the glassy magnetic behavior.

Sample bars of approximate dimensions of 1 mm x 3 mm x 6 mm were mounted with Ag paste contacts and Cu wires for the 2 to 300 K magnetotransport study using the Electrical Transport Option (ETO) of the PPMS. The in-line resistivity, ρ_{xx}, was measured by the standard 4-probe AC technique. The magnetoresistance is defined as: $MR(H) = \frac{1}{2}(\Delta\rho_{xx}(H) + \Delta\rho_{xx}(-H))/\rho_{xx}(H = 0)$, where $\Delta\rho_{xx}(H) = \rho_{xx}(H) - \rho_{xx}(H = 0)$. $MR(H)$ was assessed with the applied current perpendicular to the magnetic field direction and symmetrized over the field sweep of 140 kOe to -140 kOe to remove any effects from the misalignment between the electric and magnetic fields. The transverse (Hall) voltage mutually orthogonal to the applied current and magnetic field was also determined with the PPMS ETO. As a function of the applied magnetic field, the Hall voltage was linear, so the data between -10 kOe and 10 kOe were used for the calculation of the Hall coefficient, R_H. No anomalous Hall signal due to the magnetization was detected, likely because the moments in the samples are quite small. The carrier concentration was extracted as $n_H = (eR_H)^{-1}$, where e is the electron charge.

4.3 Results and Discussion

4.3.1 Microstructural Properties

A thorough discussion of the phases present in the TZHNSS samples and their respective chemical compositions and spatial extent is given in Ref. [98]. A few points are worthy mentioning here. First, the samples feature powder X-ray diffraction (PXRD) patterns with all peaks indexed to the desired HH structure type, and no impurity peaks were detected within the resolution of the PXRD machine. Scanning electron microscopy (SEM) confirmed the multiphase nature of the compounds

that was suggested by the splitting of the (220) peak in the PXRD, the dominant phases being one rich in Ti and one rich in (Zr, Hf). Furthermore, transmission electron microscopy (TEM) discovered Fe-rich FH nanoparticles dispersed among the two different HH phases. Electron probe microanalysis results indicated that the magnetic FH nanoparticles were of approximate composition $TiNi_{4/3}Fe_{2/3}Sn$ with average spatial extent minimized in HH5. Higher levels of Fe doping caused larger FH conglomerations. The size distribution, number and chemical composition of the magnetic domains within the Fe-added TZHNSS samples have a direct impact on the magnetic properties as well as the electronic transport, to be discussed hereafter.

4.3.2 Magnetic Properties of $Ti_{0.25}Zr_{0.25}Hf_{0.50}NiSn_{0.975}Sb_{0.025}$

To understand the effect of the FH $TiNi_{4/3}Fe_{2/3}Sn$ magnetic nanoparticles on the properties of the TZHNSS system, we must first assess the Fe-free base sample, $Ti_{0.25}Zr_{0.25}Hf_{0.50}NiSn_{0.975}Sb_{0.025}$. The zero-field-cooled (ZFC) and field-cooled (FC) magnetic moments, m, for the pure sample are given in Figure 4.1(a). With magnetic moments less than a ten-thousandth of a Bohr magneton, $\mu_B = 9.274 \text{ x } 10^{-24}$ JT^{-1}, per formula unit over the entire temperature range, the sample is essentially non-magnetic and does not host long-range magnetic order. At temperatures below approximately 125 K, the ZFC and FC magnetization curves diverge, with the collective moments cooled without an applied field shrinking in overall magnitude. The temperature at which the ZFC-FC divergence occurs is known as the irreversibility temperature, T_{ir}. Typically, such ZFC-FC bifurcation is attributed to spin-glass behavior or superparamagnetism [29, 30, 114, 115, 116, 117]. In either case, at temperatures lower than some freezing temperature, T_f, defined as the maximum in the ZFC curve, the magnetic moments constituting the system are essentially frozen in space. Raising the temperature unblocks some of the moments, which then contribute to an increasing susceptibility. Here, $T_f \approx 37$ K. Because superparamagnetism requires localized nanoscale regions of magnetically ordered particles, we do not expect that it would be relevant in the Fe-free TZHNSS sample. Furthermore, the lack of a sharp m vs. H slope at temperatures higher than T_{ir} at low fields (Fig. 4.1(b)) does not align with superparamagnetism. The possibility of spin-glass behavior is more convincing. The natural phase separation of the compound, the high likelihood of antisite disorder, and the full ionization of the Sb dopant could all lead to frustration of the magnetic moments. The resulting spin glass would account for the ZFC-FC bifurcation. Unfortunately, because the magnetism in the pure sample is so weak, we cannot rigorously confirm the spin-glass state through other available experimental techniques (the AC susceptibility measurement) that will be applied later to the more strongly magnetic Fe-added TZHNSS samples.

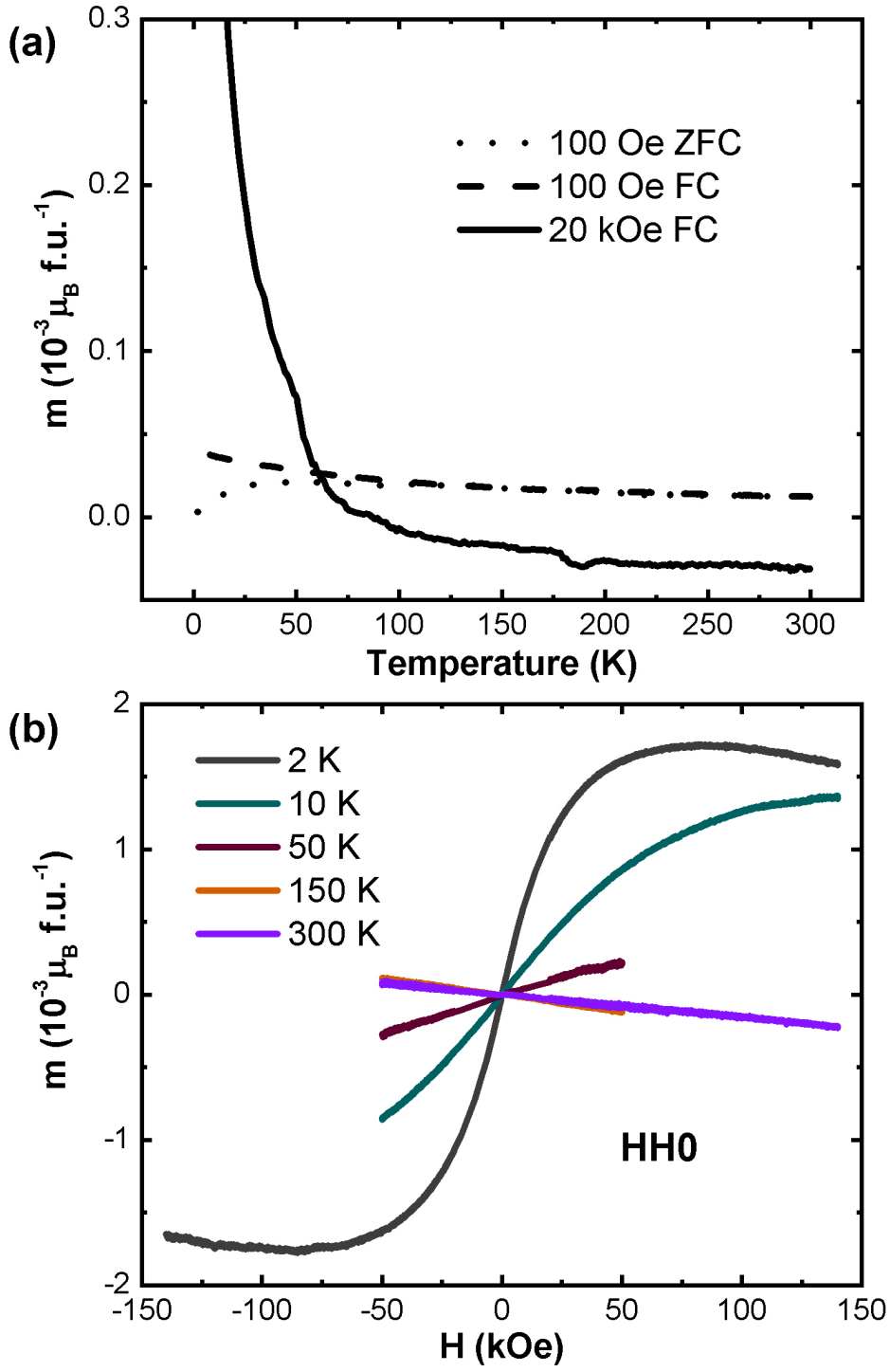

Figure 4.1: **Magnetic properties of the pure $Ti_{0.25}Zr_{0.25}Hf_{0.50}NiSn_{0.975}Sb_{0.025}$ sample.** (a) Zero-field-cooled (ZFC) and field-cooled (FC) temperature-dependent magnetic moments of the pure TZHNSS sample under an applied magnetic field of 100 Oe (dotted and dashed lines, respectively) and 20 kOe (FC, solid line). (b) DC magnetization as a function of applied field at a variety of temperatures for the pure TZHNSS sample.

Looking at the 20 kOe FC curve for the pure TZHNSS sample in Fig. 4.1(a), the diamagnetic response at room temperature persists down to $\approx$ 80 K, below which a paramagnetic signal dominates. The diamagnetism at temperatures higher than 80 K is simple to understand. According to the Slater-Pauling rule for HHs, all (Ti, Zr, Hf)NiSn compounds should possess zero magnetic moment because their d-bands are full [93]. In practice, TiNiSn is known to be strongly diamagnetic, whereas HfNiSn is either diamagnetic or paramagnetic based on temperature and synthesis conditions [118]. Because the pure TZHNSS sample studied here is a composite of $Ti_xZr_yHf_{1-x-y}NiSn$ phases, the magnetization will be a weighted sum of the individual contributions, resulting in the observed paramagnetic to diamagnetic transition. In addition, localized moments stemming from defects (site disorder) and/or impurities, such as the ionized Sb dopant, can contribute to a paramagnetic signal at the lowest temperatures.

4.3.3 Magnetic Properties of $Ti_{0.25}Zr_{0.25}Hf_{0.50}NiFe_xSn_{0.975}Sb_{0.025}$

Figure 4.2 demonstrates the weak ferromagnetism characteristic of the Fe-added TZHNSS samples. With moments that are fractions of Bohr magnetons per Fe atom, it is evident that the magnetism does not stem directly from bare Fe atoms or Fe agglomerations. Rather, the source of the ferromagnetism is the Fe-rich FH inclusions of various sizes and narrow range of chemical compositions that are verified to be magnetic based on their electron count [93, 98] and previous susceptibility measurements [119]. In Fig. 4.2(a), the ZFC-FC curves for the Fe-added samples are displayed. The curves agree well with our previous work [98], except for the ZFC data of the $x = 0.10$ sample, which feature a downturn with decreasing temperature in Ref. [98]. We suspect that the sensitivity of the magnetism on the underlying microstructure and corresponding nominal composition, to be discussed shortly, may account for the difference.

With the FC susceptibility returning at higher values than the ZFC, all Fe-added samples exhibit a similar ZFC-FC bifurcation as that of the pure TZHNSS sample. However, the divergence between the ZFC and FC curves starts at the highest temperature of the VSM measurement ($T_{ir} =$ 300 K), and the magnitude of the separation is considerably larger than that observed in the pure sample. The open hysteresis loops at 2 K and 300 K (Figs. 4.2(c,d), respectively) indicate that inherent magnetic frustration is responsible for the ZFC-FC bifurcation, favoring a greater alignment of the moments as the samples are cooled with field. Magnetic frustration is common in alloys where the magnetic elements may be disordered on different sites within the crystal structure, such as in the FH phase $TiNi_{4/3}Fe_{2/3}Sn$ present in the Fe-added TZHNSS composites [30]. If the temperatures of the ZFC-FC measurement were extended to the $T_C \approx 650$ K determined in our HT study [98], it is likely that we would find $T_{ir} \approx T_C$ because the magnetic frustration would be washed away at $T > T_C$.

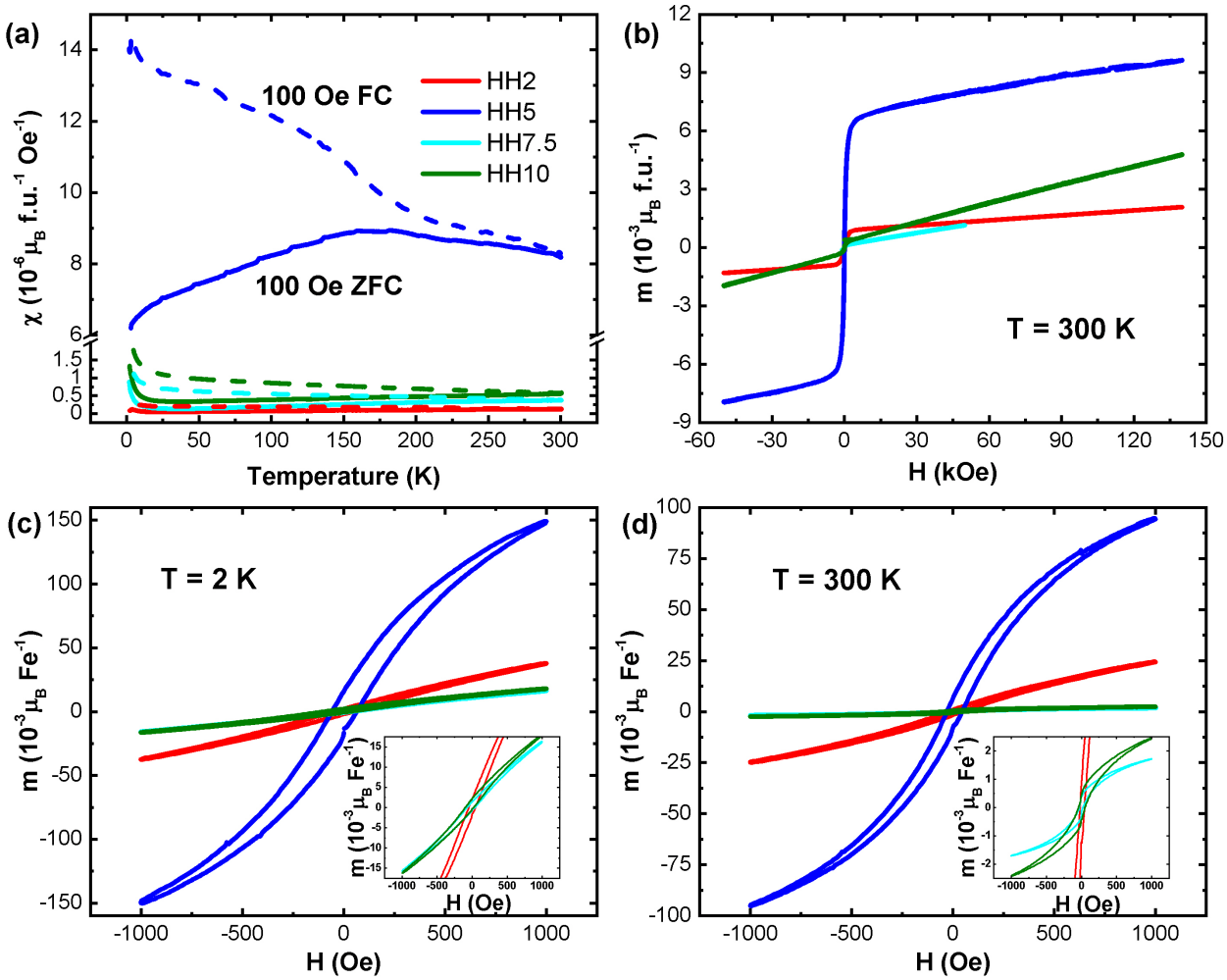

Figure 4.2: **Magnetic properties of the Fe-added $Ti_{0.25}Zr_{0.25}Hf_{0.50}NiFe_xSn_{0.975}Sb_{0.025}$ samples.** (a) Zero-field-cooled (ZFC) and field-cooled (FC) temperature-dependent magnetic susceptibility of the Fe-added TZHNSS samples under an applied magnetic field of 100 Oe (solid and dashed lines, respectively). (b) High-field magnetic moments at 300 K, illustrating the sharp superparamagnetic nature most notable in the 5 at% Fe-added TZHNSS sample. Hysteresis loops for the Fe-added samples are shown at 2 K (c) and 300 K (d), with the insets being zoomed-in versions of the lower moment samples.

Maxima present in all the ZFC curves, most notable in the HH5 sample with $T_f \approx 175$ K, are suggestive of either spin-glass or superparamagnetic behavior. The sharp rise in magnetization as the applied field is increased (Fig. 4.2(b)) strongly supports the role of superparamagnetism, which we expected after witnessing a high concentration of fine (< 50 nm) ferromagnetic nanoparticles in our microscopy study of the 5 at% Fe-added sample. Nanoscale magnetic domains with sufficient thermal energy ($T > T_f$, the so-called blocking temperature) can overcome the built-in anisotropy to behave like paramagnets with large moments [29, 30, 114]. Reducing the size of the nanoparticles decreases the energy barrier for the superparamagnetic behavior, resulting in lower

values of T_f. The transition to and from the superparamagnetic state is sharp if the nanoparticle size is narrowly distributed, but otherwise broadens when there is a greater range of nanoparticle sizes. Corresponding to the broad size distribution of magnetic nanoparticles present in HH5, the $T_f \approx 175$ K noted in Fig. 4.2(a) is merely the maximum of a wide transition that may span 100 to 250 K.

One of the hallmarks of the superparamagnetism is the universal relation at temperatures higher than T_f between the normalized magnetization, m/m_s, where m_s is the saturation magnetization, and the temperature-reduced applied field, H/T [120, 121, 122]. At temperatures lower than T_f, superparamagnetism is frozen out, the long-range magnetic interactions return, and the m/m_s vs. H/T curves no longer overlap. Figure 4.3(a) exhibits this exact scenario as additional evidence for superparamagnetism in HH5. The 150 and 300 K curves follow each other closely, whereas the lower temperature data separates. Because the lightly doped HH2 contains far fewer ferromagnetic nanoparticles than in HH5, the superparamagnetism is not as strong (Fig. 4.2(b)), and the tendency of the nanoparticles to agglomerate in the more heavily doped samples [98] diminishes the superparamagnetic signal.

By definition, superparamagnetic particles are non-interacting and do not give rise to hysteresis. Yet, clearly there are remanent fields in the magnetization of the HH5 sample at temperatures above and below T_f (Fig. 4.2 (c,d)). Such a behavior has been observed previously in more traditional, ideal superparamagnetic systems [123, 124] and can be accounted for by a broad distribution of magnetic domain sizes. Typically on the scale of microns, larger magnetic clusters can interact and form a cluster glass as the temperature is lowered. Cluster glasses exhibit hysteresis at temperatures above and below the blocking temperature and display many of the same features as superparamagnets. Given the distribution of magnetic nanoparticle size we observed in the Fe-added TZHNSS samples, we expect both superparamagnetic and cluster-glass domains to be present. To further investigate the combination in HH5, we assessed the AC susceptibility as a function of temperature and drive field frequency, ω, a technique that is well grounded both experimentally and phenomenologically in the field of spin glasses and superparamagnetism [30, 115, 116, 117, 125]. The real part of the AC susceptibility, χ', measures how well the magnetic moments align in-phase with the AC drive field, H_{ac}. For the small $H_{ac} = 5$ Oe used here, χ' represents mainly magnetic domain wall motion because aligning entire magnetic domains, even those that only extend several nanometers, with the field requires larger amplitudes. The imaginary part of the susceptibility, χ'', is the out-of-phase response of the material to the AC drive field that stems from long relaxation times of excited spins compared to the inverse frequency of H_{ac}. χ' and χ'' for HH5 at four different values of ω are displayed in Fig. 4.3(b).

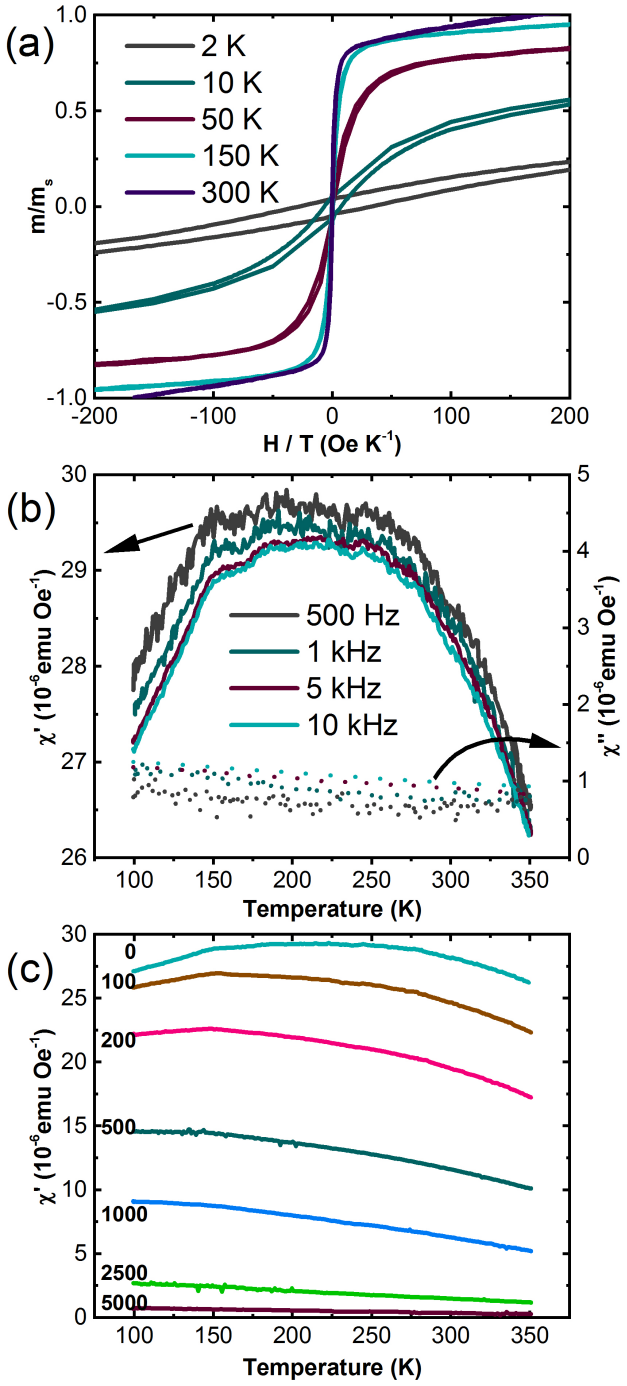

Figure 4.3: **$Ti_{0.25}Zr_{0.25}Hf_{0.50}NiFe_{0.05}Sn_{0.975}Sb_{0.025}$ (HH5) superparamagnetism and cluster-glass behavior.** (a) Normalized DC magnetization versus H/T for different temperatures. (b) The real (χ', solid lines) and imaginary (χ'', dotted lines) parts of the AC susceptibility shown for different excitation frequencies, $H_{ac} = 5$ Oe, and zero background magnetic field, $H_{dc} = 0$ Oe. (c) $\chi'(T)$ with several background magnetic fields, labelled in bold to the left of the curves in units of Oe; $\omega = 10$ kHz, $H_{ac} = 5$ Oe.

Notably, HH5 exhibits a maximum in χ' between 175 and 225 K depending on the AC drive

field frequency. The temperature range corresponds well with the $T_f \approx 175$ K extracted from the DC-measured ZFC curve. At temperatures lower than T_f, the real part of the susceptibility decreases as the magnetic domain wall motion and small magnetic domain switching becomes increasingly difficult. Examining the frequency dependence of χ', we notice that the temperature T_f at which the maximum occurs shifts to higher values as ω is increased (Fig. 4.3(b)), a typical behavior of spin glasses and superparamagnets. It should be noted that the critical temperatures in ferromagnets and antiferromagnets also display a similar frequency dependence, but with ω on the order of MHz and GHz due to very short spin-spin relaxation times [30, 120, 125, 126]. In the present study, the excitation frequencies are experimentally limited to 10 kHz, which is suitable for the investigation of glassy behavior that is present in longer spin-lattice relaxation times. For glassy states, the relaxation times of the magnetic moments increase with decreasing temperature following an Arrhenius description. Therefore, higher frequency AC drive fields will experience the greatest χ response at higher temperatures where the relaxation times are shorter. The shift in T_f as a function of ω can be used to distinguish ideal spin-glass, cluster-glass and superparamagnetic states via the phenomenological parameter

$$\delta T_f = \frac{\Delta T_f}{T_f \Delta(\log \omega)}. \tag{4.1}$$

From the experimental data in Fig. 4.3(b), $\delta T_f \approx 0.10$, compared to values typically associated with cluster glasses (≈ 0.05) and superparamagnets (≈ 0.10 to 0.30) [30, 127]. The intermediate value corroborates the presence of both phenomena, as already suggested by the DC magnetization and microscopy studies. The combination of the fine magnetic nanoparticles (< 50 nm) and larger interacting clusters gives rise to a "mictomagnetic", or mixed, state.

In most of the spin-glass literature, the value of χ'' is typically up to an order of magnitude smaller than that of χ', and χ'' as a function of temperature usually contains a maximum within a few degrees of that seen in χ'. The two characteristics are evident from the Casimir-du Pré equations that govern the effects of spin-lattice relaxation in an oscillating magnetic field [128]:

$$\chi' = \chi_S + \frac{\chi_T - \chi_S}{1 + \omega^2\tau^2};\ \chi'' = \omega\tau \left(\frac{\chi_T - \chi_S}{1 + \omega^2\tau^2} \right), \tag{4.2}$$

where χ_S is the adiabatic susceptibility (the spin and lattice do not exchange energy), χ_T is the isothermal susceptibility (the spin and the lattice are at the same temperature) and τ is the relaxation time. In the limits $\omega\tau \gg 1$ and $\omega\tau \ll 1$, $\chi' \to \chi_S$ and $\chi' \to \chi_T$, respectively, while χ'' approaches zero. Between the two extremes, i.e. $\omega\tau \approx 1$, the two are comparable, and for $\omega\tau = 1$ exactly, $\chi' = \chi'' + \chi_S$, thus reconciling the typically larger values of χ' than those of χ''. From Eq. 4.2, it is not too difficult to show that $\frac{d^2\chi''}{d\omega^2} \propto \frac{d\chi'}{d\omega}$, meaning that a maximum in the real part occurs when the imaginary part is changing slope the fastest [30]. According to the functional form of χ'', a

maximum occurs near its own inflection point, thus yielding the neighboring maxima in χ' and χ''. Yet, in Fig. 4.3(b), no maximum in χ'' accompanies that seen in χ', and the χ'' values are so diminished that they are essentially equal to the background levels of the quartz paddle used in the PPMS measurement. Unfortunately, because χ' itself is already quite small, the further reduced χ'' is not detected by the susceptometer. Thus, no analysis can be performed on the imaginary component of the susceptibility.

As a final step in characterizing the magnetic interactions in the HH5 sample, we again performed the AC susceptibility measurement at $\omega = 10$ kHz and $H_{ac} = 5$ Oe, but with background magnetic fields, H_{dc}, spanning from 100 Oe to 5 kOe. The temperature- and magnetic field-dependent χ' is shown in Fig. 4.3(c). With increasing H_{dc}, the magnitude of the real part of the susceptibility constantly declines, as expected from the softening of the DC magnetization curves at larger fields (Fig. 4.2(c,d)). The maximum witnessed at zero applied field shifts to lower temperatures, and a prominent kink develops near 150 K, likely corresponding to the freezing of magnetic nanoparticles with a concentrated spatial extent < 50 nm. At higher background magnetic fields, the AC drive field becomes less relevant, and the freezing phenomena subside. With the analysis of the magnetic properties in the Fe-added TZHNSS samples complete, we now turn to the magnetotransport and the unique interactions of the itinerant (conduction) electrons with the magnetic $TiNi_{4/3}Fe_{2/3}Sn$ phases present in the samples.

4.3.4 Kondo Effect and Weak Anti-Localization

The degenerate semiconducting nature of the TZHNSS compounds is demonstrated in the in-line electrical resistivity, ρ_{xx}, plotted in Figure 4.4(a). Similar to the magnetization as a function of the amount of Fe, the electrical resistivity increases to a maximum for the HH5 sample, drops at the 7.5 at% Fe level and rises thereafter. The trend matches with that of the carrier concentration (Fig. 4.4(b)) and agrees with the HT data [98]. Given that the observed magnetic nanoinclusions within the Fe-added TZHNSS samples decrease in size and increase in number density until the 5 at% Fe level, then begin to agglomerate at greater dopant levels, we expect an interaction between the charge carriers and the magnetic secondary phase to be the cause of the observed variation in the electrical properties. Specifically, a localization behavior of the charge carriers around the magnetic nanoinclusions would explain the diminished carrier concentration and enhanced resistivity.

For most of the temperature range, $\frac{d\rho_{xx}}{dT} > 0$, as expected from the small electronic band gaps of HHs and associated large carrier concentrations (mid 10^{20} cm^{-3} to 10^{21} cm^{-3}) [99, 118, 129]. An exception to the metallic behavior can be found in the electrical resistivity of the Fe-added samples, a close-up of which is shown in Fig. 4.4(c). Evidently, minima in ρ_{xx} occur near 25 to 30 K and $\frac{d\rho_{xx}}{dT} < 0$ at lower temperatures, which is entirely absent in the pure TZHNSS sample.

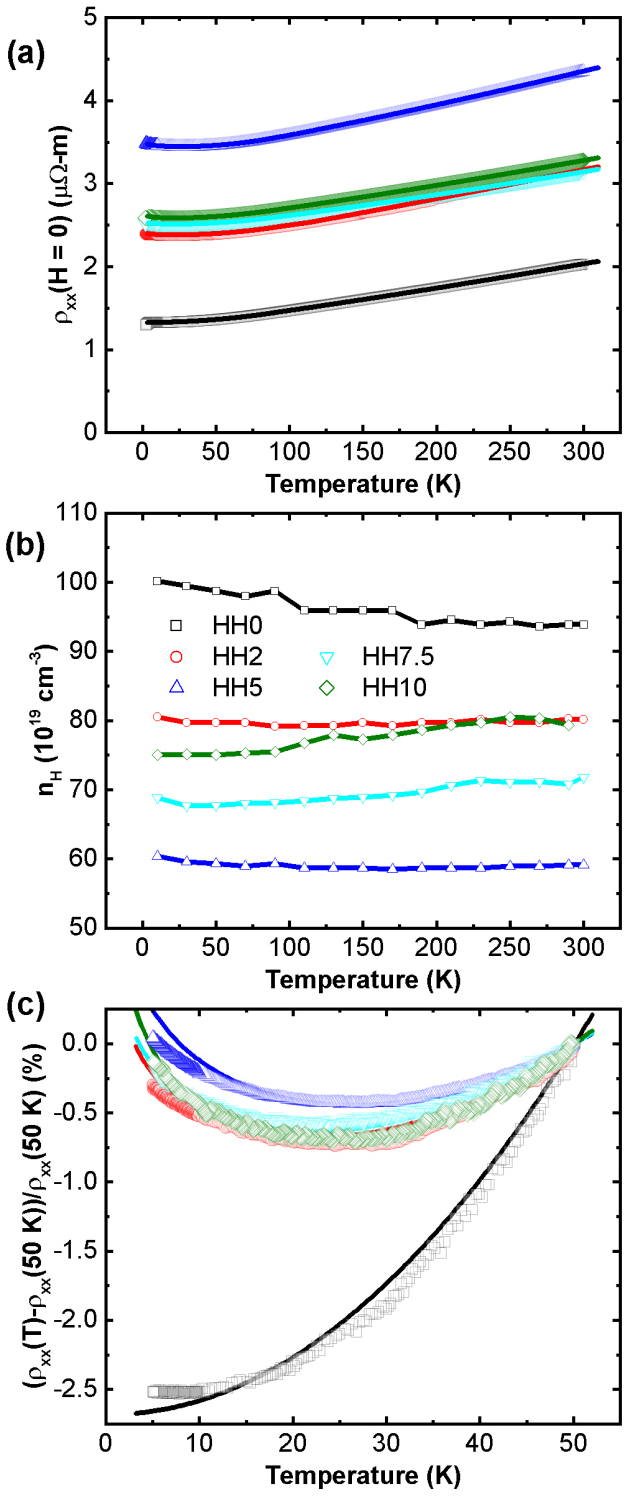

Figure 4.4: **Electronic properties of the $Ti_{0.25}Zr_{0.25}Hf_{0.50}NiFe_xSn_{0.975}Sb_{0.025}$ composites.** (a) Electrical resistivity and (b) carrier concentration of the five samples over the full temperature range. (c) Electrical resistivity normalized to the individual values at 50 K, showing minima near 25 to 30 K in the Fe-added samples. In (a) and (c), the open symbols are the experimental data, and the solid lines are the fits extracted from Eq. 4.3.

The source of the behavior could be the freezing out of carriers that were thermally excited to an Fe-induced impurity band separated from the Fermi level by a few meV. However, the carrier concentration is essentially constant as a function of temperature below 100 K. Furthermore, the associated scattering of charge carriers by ionized impurities would yield a $\rho_{xx} \propto T^{-3/2}$ functional dependence that does not agree well with the data.

An alternative, more intuitive explanation for the resistivity minimum is the Kondo effect [130, 131]. Dilute magnetic phases within metals and semiconductors can act as localized spins that interact with itinerant electrons through exchange coupling, based on the Pauli exclusion principle. As the temperature is lowered and other electron scattering mechanisms become less important, the interaction between free carriers and the magnetic ions intensifies, contributing positively to the resistance below the Kondo temperature, T_K. Because magnetic iron was added into the phase-separated HH samples of this study, it is natural to expect that some form of the Kondo effect may occur, either through widely dispersed single Fe atoms or magnetic secondary phases spatially separated on the microscale. Our X-ray diffraction and transmission electron microscopy studies found no evidence for the presence of individual iron atoms randomly located throughout the compounds and indeed demonstrated the existence of an Fe-rich secondary FH phase ($TiNi_{4/3}Fe_{2/3}Sn$) in the materials [98]. Typically, the Kondo effect resulting from the presence of bare magnetic elements, such as Fe, Co, Cr, Mn, etc., widely dispersed in metallic and semiconducting matrices can result in something like a 10% upturn in ρ_{xx} below T_K. Here, the effect is $< 1\%$, which suggests that the magnetic source is not elemental Fe, but rather the FH phase in the Fe-added TZHNSS composites.

To substantiate the charge carrier scattering by the dispersed magnetic phases, we fit the resistivity data to the following functional form:

$$\rho_{xx} = \rho_{xx,0} + aT^b - c\ln(T), \tag{4.3}$$

where $\rho_{xx,0}$ is the residual resistivity and a, b and c are free parameters [130, 131]. The second term in Eq. 4.3 covers generic scattering in disordered solids, while the last term represents the magnetic screening. Procedurally, the parameters of the model (Eq. 4.3) were allowed to take on distinct values at temperatures above and below 100 K, far from the Kondo temperature, except for the constraint $c = 0$ above 100 K and for the Fe-free TZHNSS sample. The results of the fitting are plotted as solid lines in Fig. 4.4(a,c), with the corresponding parameters listed in Table 4.1. At the lowest temperatures, the coupling between the Kondo centers and the itinerant electrons becomes stronger than the electron-electron interaction ($b \approx 2$) to yield the minimum in the electrical resistivity closely matching the data. Evaluating the ratio of the Kondo and disorder terms at $T = 25$ K (Table 4.1), $\frac{c\ln(25)}{a*25^b}$ is much larger ($\approx$ 55 to 70%) for the HH5 sample than for the rest of the Fe-added samples. With an increased number of the magnetic nanoinclusions and a comparatively

Table 4.1: Fitting parameters extracted from the comparison of the electrical resistivity data for $Ti_{0.25}Zr_{0.25}Hf_{0.50}NiFe_xSn_{0.975}Sb_{0.025}$ (Fig. 4.4(a)) to Eq. 4.3. The units of $\rho_{xx,0}$ are $\mu\Omega$-m; $a(T < 100$ K) is given in $10^{-12}\Omega$-m-K^{-b}; b is unitless; c and $a(T > 100$ K) are given in nΩ-m and nΩ-m-K^{-b}, respectively. The last column represents the ratio of the Kondo and disorder terms in Eq. 4.3 at $T = 25$ K.

Sample	$\rho_{xx,0}(T < 100$ K)	$a(T < 100$ K)	$b(T < 100$ K)	c
HH0	1.33	13.01	2.03	-
HH2	2.41	4.46	2.25	10.6
HH5	3.50	4.45	2.30	19.3
HH7.5	2.54	10.12	2.06	11.9
HH10	2.63	24.49	1.91	17.7
	$\rho_{xx,0}(T > 100$ K)	$a(T > 100$ K)	$b(T > 100$ K)	$\frac{c\ln(25)}{a*25^b} * 10^{-3}$
HH0	1.25	1.03	1.16	-
HH2	2.22	1.49	1.13	5.5
HH5	3.30	1.10	1.20	8.5
HH7.5	2.43	0.63	1.23	5.0
HH10	2.50	0.84	1.20	5.0

lower carrier concentration, the HH5 sample evidently plays host to stronger Kondo screening.

In Kondo's theory, the magnetic ions are treated as non-interacting and dilute, i.e. paramagnetic. Therefore, it may seem that the Kondo effect cannot take place in the Fe-added TZHNSS samples, which we have shown to contain ferromagnetic ordering. However, the presence of free spins that contribute a paramagnetic behavior within an overall ferromagnetic material can still give rise to the Kondo effect, as has been observed in ferromagnetic GaMnAs films [132] and (Fe, Co)-Pd-Si alloys [133]. In each case, a distribution of the magnetic moments allows for essentially free spins to develop the Kondo effect while the non-zero moments maintain a spontaneous magnetization. As we noted previously, the dispersed $TiNi_{4/3}Fe_{2/3}Sn$ clusters vary in size and composition throughout the Fe-added TZHNSS samples, yielding a range of effective moments. We have discerned that the magnetic nanoinclusions lead to superparamagnetism and free spins, whereas the larger micron-sized precipitates give rise to weak ferromagnetism (coercive fields $\approx$ 100 Oe). The mictomagnetic nature of the Fe-added samples therefore allows for the simultaneous presence of the Kondo effect and ferromagnetism.

The Fe-free TZHNSS sample does not feature an electrical resistivity minimum like the Fe-added samples, but does exhibit a decreasing ρ_{xx} below a temperature of $\approx$ 4 K. A plot of the electrical resistivity normalized by $\rho_{xx}(T = 2$ K) for the pure sample is displayed in Figure 4.5(a). Two potential causes of the resistance drop-off are the following: (1) the presence of elemental Sn ($T_C \approx 3.7$ K) and its binaries that would render part of the sample superconducting below

T_C; and (2) the weak anti-localization (WAL) effect. A quantum intereference phenomenon that occurs at low temperatures in disordered solids, the WAL effect is the result of the phase coherence length of a charge carrier exceeding the mean free path between its elastic collisions [134]. In such a quantum diffusive transport regime, the time-forward and time-backward scattering amplitudes can interfere destructively to yield a lower resistive state, i.e. anti-localization. The application of a magnetic field breaks time reversal symmetry, which destroys the quantum interference of the time-reversed diffusive pathways of the charge carriers and lifts the WAL effect. In Type 1 superconductivity, the Cooper pairs are broken above a critical magnetic field, and the normal state is restored. Thus, when the TZHNSS sample is cooled in the presence of a large magnetic field of 8 T, the lower resistance state at temperatures below 4 K no longer exists (open squares in Fig. 4.5(a)).

To discover whether (1) or (2) is the proper explanation of the resistance drop-off in the pure TZHNSS sample, we assessed the magnetoresistance, MR, plots of which are given in Figs. 4.5(b,c). The first item to note is that returning to the normal resistive state at 2 and 3 K requires magnetic fields of $\approx$ 10 kOe. The potential presence of superconducting Sn and its binaries would give way to the non-superconducting state at fields no greater than $\approx$ 500 Oe [135]. As a result, the enhanced conductivity at temperatures lower than 4 K in the TZHNSS sample is not due to superconducting secondary phases. To substantiate the presence of the WAL effect, we assessed the electrical conductivity data as a function of temperature and applied magnetic field within the well accepted WAL model. The temperature-dependent in-line electrical conductivity, $\sigma_{xx}(T)$, in a weakly delocalized state in three dimensions can be expressed as

$$\sigma_{xx}(T) = \sigma_{xx}(T = T') - \frac{2e^2}{\pi^2 ha}(T^{\frac{p}{2}} - T'^{\frac{p}{2}}), \tag{4.4}$$

where T' is a reference temperature typically taken as the lowest temperature of the study, and h is the Planck constant [134]. The characteristic length scale of the delocalization is set by a such that an electron travels on average a distance of $L_{del} = aT^{-p/2}$ between inelastic collisions, which are disruptive of the phase. p is a scattering parameter that describes the source of the inelastic potential as Coulombic (electron-electron) in impure materials ($p = \frac{3}{2}$), Coulombic in the pure regime ($p = 2$), or due to electron-phonon interactions ($p = 3$). Fitting the data for the pure sample to Eq. 4.4 over the temperature range of $\approx$ 1.8 to 4 K, the closest matching scattering parameter is $p = \frac{3}{2}$, reflecting the expected impurity-laden nature of the disordered semiconducting compound. The best-fit value $a = 9.0 \pm 1.9$ Å is the average length over which an electron in pure TZHNSS maintains its quantum phase at 1 K. The red line in Fig. 4.5(a) represents the least-squares match between the experimental data and Eq. 4.4.

Given the success of the temperature-dependent fitting to the WAL model and the previous observation of weak anti-localization in other HH compounds [118], the WAL effect is a reasonable

explanation for the large $\Delta\rho_{xx}$ at the lowest temperatures in our study. In fact, the presence of the WAL effect should not be surprising given the poor charge carrier mobility (< 50 cm^{2}V^{-1}s^{-1}) that makes for a small electronic mean free path and greater likelihood that the phase coherence length will surpass it. Another important ingredient for the WAL effect is strong spin-orbit scattering, which is certainly anticipated with the heavy elements in TZHNSS.

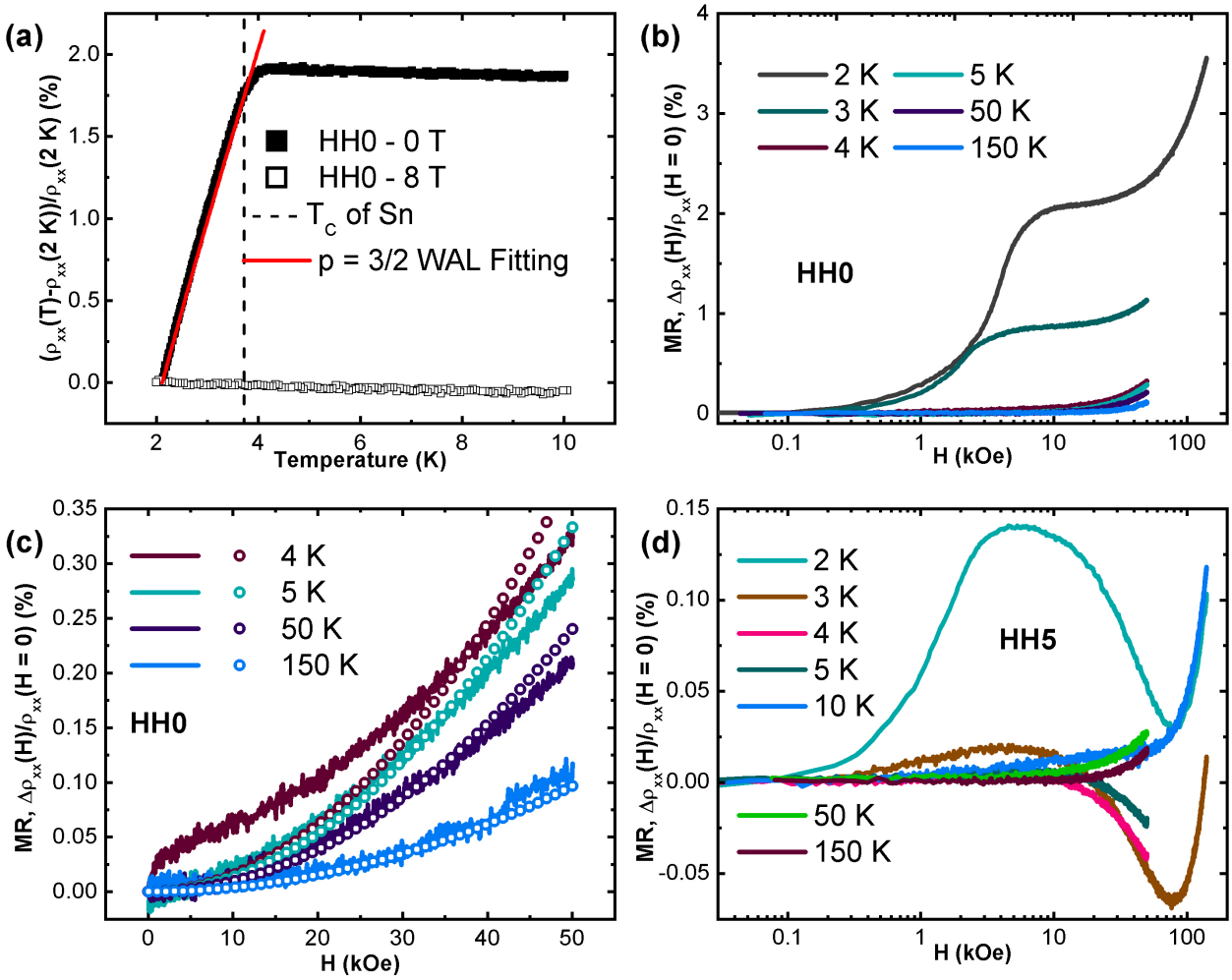

Figure 4.5: **Weak anti-localization and magnetoresistance, MR, of the half-Heusler composites.** (a) Electrical resistivity of the pure $x = 0$ sample normalized to the 2 K value with (open squares) and without (solid squares) applied magnetic field. The superconducting critical temperature of elemental tin is shown for reference. The red solid line is the $p = \frac{3}{2}$ WAL fitting described by Eq. 4.4. (b) MR of the pure $x = 0$ sample against applied magnetic field at a variety of temperatures. Note the logarithmic scaling of the x-axis. (c) Close-up of the MR with smaller fields than in (b) and a linear x-axis. The open circles are best-fit quadratic terms reflecting the classical magnetoresistance outside the anti-localized state. (d) MR of the $x = 0.05$ sample with logarithmic scaling of the x-axis.

Also noteworthy in Fig. 4.5(b) is the polytonic nature of the magnetoresistance in the Fe-free

TZHNSS sample at 2 and 3 K in the delocalized state. We find that at 2 K, the MR rises linearly for fields up to $\approx$ 2.5 kOe, then increases quadratically before returning to the normal resistive state with $H \approx 10$ kOe, which is characteristic of the WAL effect. The seemingly saturated MR is further enhanced at larger fields with quadratic growth up the highest field of the study, $H =$ 140 kOe, likely due to classical magnetoresistance from the Lorentz force. Similar results hold at 3 K, except that the breaking of the anti-localization occurs near 7.5 kOe. From Fig. 4.5(c), a remnant of the WAL state at 4 K is evident in the short rise of the MR at the lowest fields, while the higher temperature curves follow the classical H^2 dependence (open circles). The absolute values of the MR decrease as a function of temperature owing to the reduced charge carrier mobility from electron-phonon scattering at higher temperatures.

Because magnetic fields are not equivalent in the time-forward and time-backward directions, the magnetism inherent to the Fe-added TZHNSS samples should serve to suppress the WAL effect observed in the pure sample. Indeed, the MR witnessed in $Ti_{0.25}Zr_{0.25}Hf_{0.50}NiFe_xSn_{0.975}Sb_{0.025}$ at 2 and 3 K is significantly reduced for $x > 0$, as exemplified by the data for HH5 shown in Fig. 4.5(d). At 2 K, the magnetoresistance rises linearly until $\approx$ 2.5 kOe and changes to a quadratic trend before reaching the normal resistive state near 5 kOe, about half that needed for the pure sample. Higher fields display $\frac{dMR}{dH} < 0$, likely as a result of preferential spin scattering providing a somewhat easier pathway for electron transport. Such a behavior is a manifestation of the interaction between the localized moments in ferromagnets and the itinerant charge carriers [136, 137, 138]. Once the magnetization is saturated, no additional gains in preferential spin scattering occur, and the classical positive magnetoresistance begins to dominate above approximately 80 kOe at 2 K. At higher temperatures, the smoother path provided by aligned spins becomes less effective as other scattering mechanisms, such as electron-phonon interactions, strengthen, yielding the standard $MR \propto H^2$. The different Fe-added samples follow the exact same trends in the MR as that displayed by the HH5 sample (Fig. 4.5(d)) with only slight variations in the magnitudes.

4.4 Conclusions

Taking the series of half-Heusler (HH) composites, $Ti_{0.25}Zr_{0.25}Hf_{0.50}NiFe_xSn_{0.975}Sb_{0.025}$, from our previous work on magnetically doped high-temperature (HT) TEs, we have explored their low-temperature (LT) DC magnetization, AC susceptibility and magnetotransport properties. The ferromagnetic signal observed at high temperatures expresses itself as a combination of superparamagnetism and cluster-glass behavior, known as mictomagnetism. The hysteresis in the DC magnetization from 2 to 300 K, the separation of the zero-field-cooled (ZFC) and field-cooled (FC) magnetic moments and the frequency- and field-dependent maxima in the AC susceptibility all

point to spin freezing phenomena in the magnetically doped samples. We illustrate the magnetic phenomena in greatest detail using the HH5 sample, given its larger magnetic moments resulting from the high concentration of magnetic $TiNi_{4/3}Fe_{2/3}Sn$ nanoparticles within the structure. Regarding the magnetotransport, we witnessed a rise in the metallic electrical resistivities of the Fe-added samples at approximately 25 K, which we believe is a manifestation of the Kondo effect. At the lowest temperatures (< 4 K), we found evidence of weak anti-localization in the pure TZHNSS sample that is quite subdued in the magnetic samples. The analysis herein is a prime example of the techniques and models needed for understanding diverse magnetic phenomena inherent to many of the latest TE materials where magnetic elements and secondary phases are being utilized.

CHAPTER 5

Magnetic Field-Dependent Heat Capacity in a Half-Heusler Composite

5.1 Motivation: Field-Dependent Heat Capacity as Essential Insight to Magnetic Refrigeration

The effect of an applied magnetic field, H, on ground-state thermodynamic properties, including the magnetic susceptibility, χ, magnetization, M, and heat capacity, C, has been critical in understanding the condensed matter physics that enables a wide range of technologies. Prime examples are the magnetocaloric effect for magnetic refrigeration [139, 140, 141], single molecule magnetism for information storage [142, 143], and the spin Seebeck effect for spintronics [144, 145]. Concerning magnetocalorics specifically, the magnetic contribution to the heat capacity at temperature T, $C_m(H,T)$, is particularly important in calculating the corresponding device figure of merit. $C_m(H,T)$ is also intrinsically tied to the most fundamental models of magnetism in condensed matter physics, including the classic Heisenberg model [146, 147] and the more recent Fermi liquid theory [148]. While studies of $C_m(H,T)$ as a function of temperature are numerous, they often struggle to disambiguate the types of magnetism present in material systems and miss out on the unique response of $C_m(H,T)$ to an applied magnetic field [149]. The rare heat capacity studies that successfully incorporate magnetic fields can be insightful [150, 151, 152], but frequently the underlying physical mechanism is unclear, and the effect is considered to be anomalous [153, 154, 155, 156, 157, 158].

To thoroughly explore the dependence of the heat capacity on magnetic field in a range of material systems, we selected a paramagnetic half-Heusler (HH) composite and its mictomagnetic counterparts (ferromagnetic $T_C \approx 650$ K) that we recently engineered for TE applications [98, 159]. As a diamagnetic comparison, we also examine the magnetothermodynamics of pure, elemental gold. At low temperatures (LTs) ($T = 2$ to 10 K), the experimentally measured C_p (heat capacity at constant pressure) in the purely paramagnetic compound features a maximum as

a function magnetic field. The mictomagnetic samples additionally display a high-field quenching of the heat capacity. We are able to satisfactorily explain most of the $C_p(H)$ behavior based on paramagnon contributions. However, the paramagnon model cannot account for the low-field heat capacity of the mictomagnetic samples at temperatures lower than 4 K. We therefore derive the magnon contribution with quartic dispersion in field to model the ferromagnetic component of C_p within the mictomagnetic samples. Despite containing only one additional free parameter, the combined paramagnon and magnon model overfits the experimental data. Separate measurements of C_p down to 0.36 K support the paramagnon analysis, yet still demonstrate the presence of a separate low-temperature magnetic field-dependent heat capacity contribution. We qualitatively connect the distinct behavior to a magnetotransport effect witnessed in our previous work [159], namely the possibility of Sn-based superconducting binaries. The $C_p(H)$ trend in the mictomagnetic samples highlights the power of assessing the heat capacity as a function of field at a given temperature compared to the lower sensitivity $C_p(T)$ studies at a given field.

5.2 Experimental Methods

Three polycrystalline HH composites of chemical formula $Ti_{0.25}Zr_{0.25}Hf_{0.50}NiFe_xSn_{0.975}Sb_{0.025}$ (TZHNSS), where x = 0, 0.05, and 0.10, were synthesized following the procedure in Ref. [98]. The exact compounds stem from our previous work optimizing the materials for thermoelectric applications. The Ti, Zr, and Hf alloying are useful in lowering the thermal conductivity, while the Sb tailors the charge carrier concentration of the compounds. Several 10-20 mg pieces were taken from each fully dense polished ingot in order to conduct the heat capacity measurements. Throughout the text and figures, we commonly refer to the HH samples individually as "HH#", where # is the atomic percentage of Fe included in the compound. Specifically, "HH0", "HH5", and "HH10" refer respectively to the 0, 5, and 10 at% Fe-added TZHNSS samples. Pure gold (Au) wire of 99.9% purity was purchased from NETZSCH for a diamagnetic comparison.

A Quantum Design Physical Property Measurement System (PPMS) Dynacool model equipped with a 14 Tesla magnet was used for all heat capacity measurements from 0.36 to 400 K. Initial temperature-dependent measurements in zero magnetic field were performed for all samples of the study upon cooling to 2 K. For the 2 to 10 K temperature scans in magnetic field, the chamber was initially set to 2 K to allow the sample holder to stabilize temperature for two hours. Then, the magnetic field was ramped to a desired value before bringing the temperature to 10 K and waiting a few minutes for temperature stability. The heat capacity was then measured in 1 K increments during cooling, with the temperature stabilized before each measurement. The process was repeated for magnetic fields of 0 to 14 T in fine increments. At each temperature and field, the sample heater was turned on to collect the time-dependent temperature response data, $T(t)$. The two-tau

modeling of $T(t)$ returned C_p values with less than 5% error. For the heat capacity measurement, a small dab of N-grease was first placed on the sample stage for an addendum measurement without the sample. Once the addendum measurement was complete, an approximately 10-20 mg thin, polished piece of the individual samples was placed on the greased stage for the sample measurement. The difference in the C_p between the sample measurement and the addendum yields the C_p of the sample. The same procedure was utilized for the measurement of $C_p(H,T)$ for HH10 down to 0.4 K, with 0.2 K increments used for the in-field scans. The He-3 option of the PPMS, which uses a specially designed sample holder to minimize background noise, addenda values and addenda field dependence, was needed to achieve such low temperatures.

5.3 Results

5.3.1 Microstructural Properties

A detailed microstructural analysis of the TZHNSS samples can be found in Ref. [98]. We summarize the important aspects here. The TZHNSS samples are composite materials with regions of Ti-rich HH and (Zr, Hf)-rich HH, as indicated by the powder X-ray diffraction (PXRD) and scanning electron microscopy (SEM). No impurity peaks were detected within the resolution of the PXRD patterns. The chemical compositions and spatial extent of the individual phases are given in Ref. [98]. Transmission electron microscopy (TEM) unveiled Fe-rich FH nanoparticles scattered among the two distinct HH phases. The magnetic FH nanoparticles are of approximate composition $TiNi_{4/3}Fe_{2/3}Sn$, as per electron probe microanalysis. In HH5, the nanoparticles are mainly isolated and $\lessapprox$ 10 nm in spatial extent. Larger conglomerations of the Fe-rich phase (up to several hundreds of microns in diameter) are present in HH10.

5.3.2 Heat Capacity as a Function of Magnetic Field

The magnetic field dependence of the heat capacity for the four samples of the study are displayed in Figure 5.1, at temperatures of 2 to 5 K, where the largest magnitude effects occur. Unlike diamagnetic Au, which features essentially constant $C_p(H)$, the HH samples exhibit starkly non-monotonic trends of the heat capacity as a function of magnetic field. Specifically, HH0 and HH5 show pronounced peaks in the heat capacities at several T, then significant declines in C_p at higher magnetic fields. The maxima contract in magnitude as the temperature is raised, while also shifting to larger magnetic field strength. For HH10, the trends are much different. At 2 K, $C_p(H)$ is fairly flat until approximately 2 T, after which it drops precipitously by 50% at 14 T, an equivalent $C_p(H)$ quenching as the HH5 sample at 2 K. Similar behavior is seen for HH10 at 3 K, but with a smaller

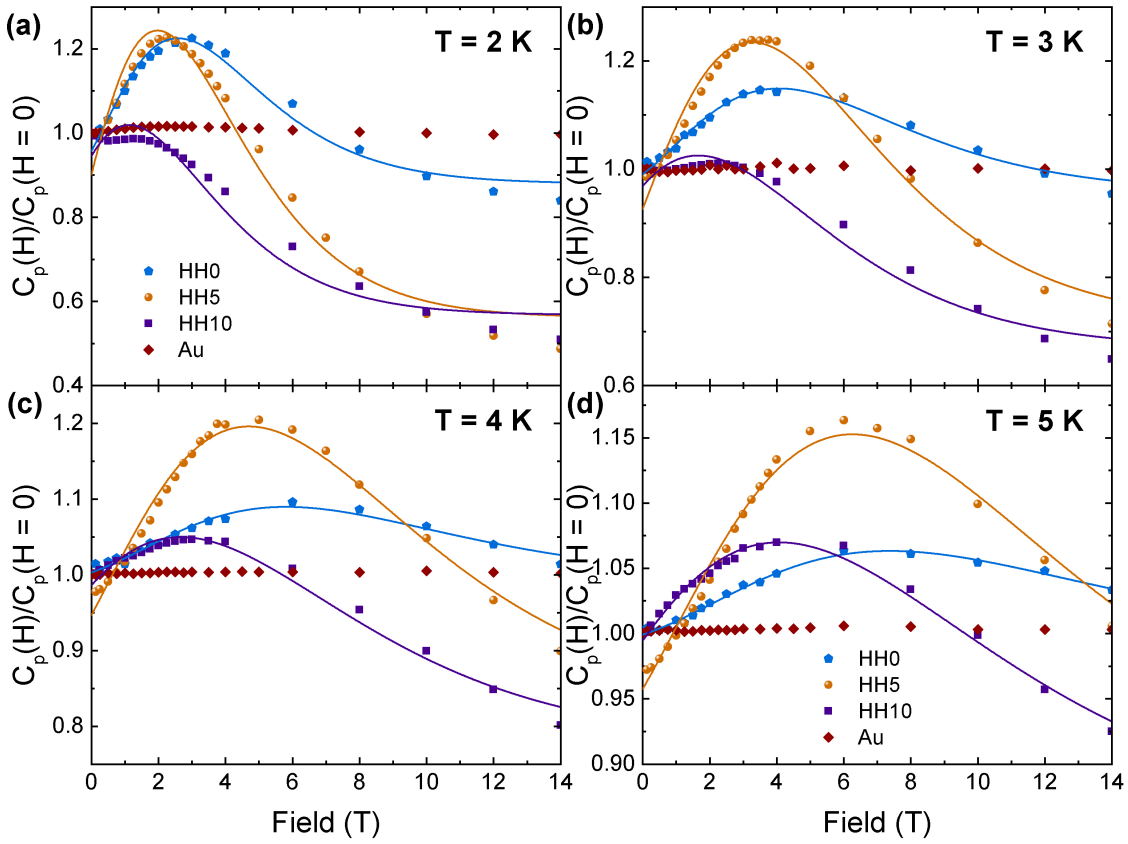

Figure 5.1: **Magnetic field-dependent heat capacity of the $Ti_{0.25}Zr_{0.25}Hf_{0.50}NiFe_xSn_{0.975}Sb_{0.025}$ samples and Au.** In (a)-(d), the best-fit curves (solid lines) are least-squares solutions of the experimental data (scattered points) to the paramagnon (PM) model at 2 to 5 K, respectively.

quenching of 35%. At 4 and 5 K, the $C_p(H)$ trends for HH10 mimic those of the other two HH samples, displaying a broad maximum at several T with an eventual decline. We stress here that the temperature-dependent C_p at set fields (Figures 5.5 and 5.7) show no signs of the unique behavior in HH10, highlighting the sensitivity of the $C_p(H)$ study.

To explain the field dependence of C_p of the three HH samples, we sought out intuitive models that could fit the experimental data with reasonable confidence intervals. Details for each model can be found in Sections 5.4.1 - 5.4.3, while the fitting procedure and error analysis are elaborated in Section 5.4.4. No modeling was performed for Au since its maximum change in $C_p(H)$ of a mere 1.5% at 2 K is within the addendum $C_p(H)$ limits (Figures 5.2(f) and 5.9(a)). Because diamagnetic Au displayed no signifcant $C_p(H)$ effect, and paramagnetic phases are a common feature of the HH samples, the role of paramagnetism in the magnetic field-dependent heat capacity was a natural first step in our inquiry. Indeed, for HH0 (Figure 5.2(a)-(e)), the best-fit minimal model over the whole temperature range is one of multi-level paramagnons (the PM model, for short), which I derived in Section 1.4.3 as Eq. 1.31, reproduced here in the following form:

$$C_{p,para} = -n_I k_B y^2 \left[(2J+1)^2 \text{csch}^2(2J+1)y - \text{csch}^2 y\right]. \tag{5.1}$$

In Eq. 5.1, n_I is the concentration of paramagnetic ions, each of total angular momentum, J, and $y = \mu_B H/k_B T$ [28]. For the HH composites, we allow for the possibility of small internal fields, $H_{int,para}$, within the sample due to the presence of Ni in the compound and the large amount of disorder that can create weak coupling of neighboring spins [152, 160, 161]. Therefore, $H = H_{int,para} + H_{ext}$, with H_{ext} the magnetic field applied by the PPMS during the experiment. The fitted curves displayed in Fig. 5.1 capture the structure of $C_p(H)$ with intuitively small internal fields, $H_{int,para} \approx 1$ T, and total angular momentum, $J = 1/2$. Our statistical analyses in Figure 5.2 demonstrate reasonable overall confidence intervals for the fit of the PM model to the data. The two-level paramagnetic contribution to the heat capacity agrees well with the strong paramagnetic signal in the magnetization of HH0 at low temperatures [98, 159]. Further, the $J = 1/2$ is a logical choice for HH0 that corresponds to an electron in an unfilled shell of a bonded atom with quenched orbital momentum [162]. The best-fit parameters of the PM model applied to the specific heat of HH0 are listed in Section 5.4.1, Table 5.1. We believe the source of the behavior in HH0 to be either ionized impurities or defects. Further discussion can be found in Section 5.4.1.

The PM model can capture the $C_p(H)$ behavior fairly well in HH5 at temperatures above 2 K and in HH10 for temperatures above 3 K. However, attempts to fit the $C_p(H)$ data with the PM model at 2 K for the HH5 sample and at 2 and 3 K for HH10 were not as successful as the fitting for HH0. The large confidence intervals of the corresponding fits in Figures 5.3(a) and 5.4(a)-(b) demonstrate the presence of a separate contribution to the $C_p(H)$. Considering that the two samples contain ferromagnetic regions in addition to their paramagnetic phases, we believed that magnons could play a role in $C_p(H)$. We therefore derived the magnon contribution to the heat capacity, $C_{p,ferro}$, as detailed in Section 5.4.2. The lengthy final expression in Eq. 5.15 is dependent on two free parameters: the spin stiffness, D, and the volume fraction of the magnon phase, v_M. Combining $C_{p,ferro}$ with $C_{p,para}$ (Eq. 5.1), we have the PM+M (paramagnons and magnons) model. After adjusting the units to match the experimental data, we were able to model the distinct behavior of $C_p(H)$ for the HH5 and HH10 samples at 2 and 3 K. The fitted curves in Figures 5.3(f) and 5.4(f) match the experimental data for HH5 and HH10 quite well, respectively. However, our statistical analysis demonstrates that the PM+M model overfits the data, as reflected in the 95% confidence intervals of the magnon fit parameters that span both positive and negative values surrounding the mean value. We can estimate v_M based on our previous microscopy work (Ref. [98]), thereby removing one of the free parameters in the PM+M model. Yet, the uncertainities in D still remain several orders of magnitude larger than the mean value. Overall confidence intervals for the fits of the PM+M model to the $C_p(H)$ of HH5 and HH10 were not calculable. Therefore, we cannot rigorously use the PM+M model to explain the additional

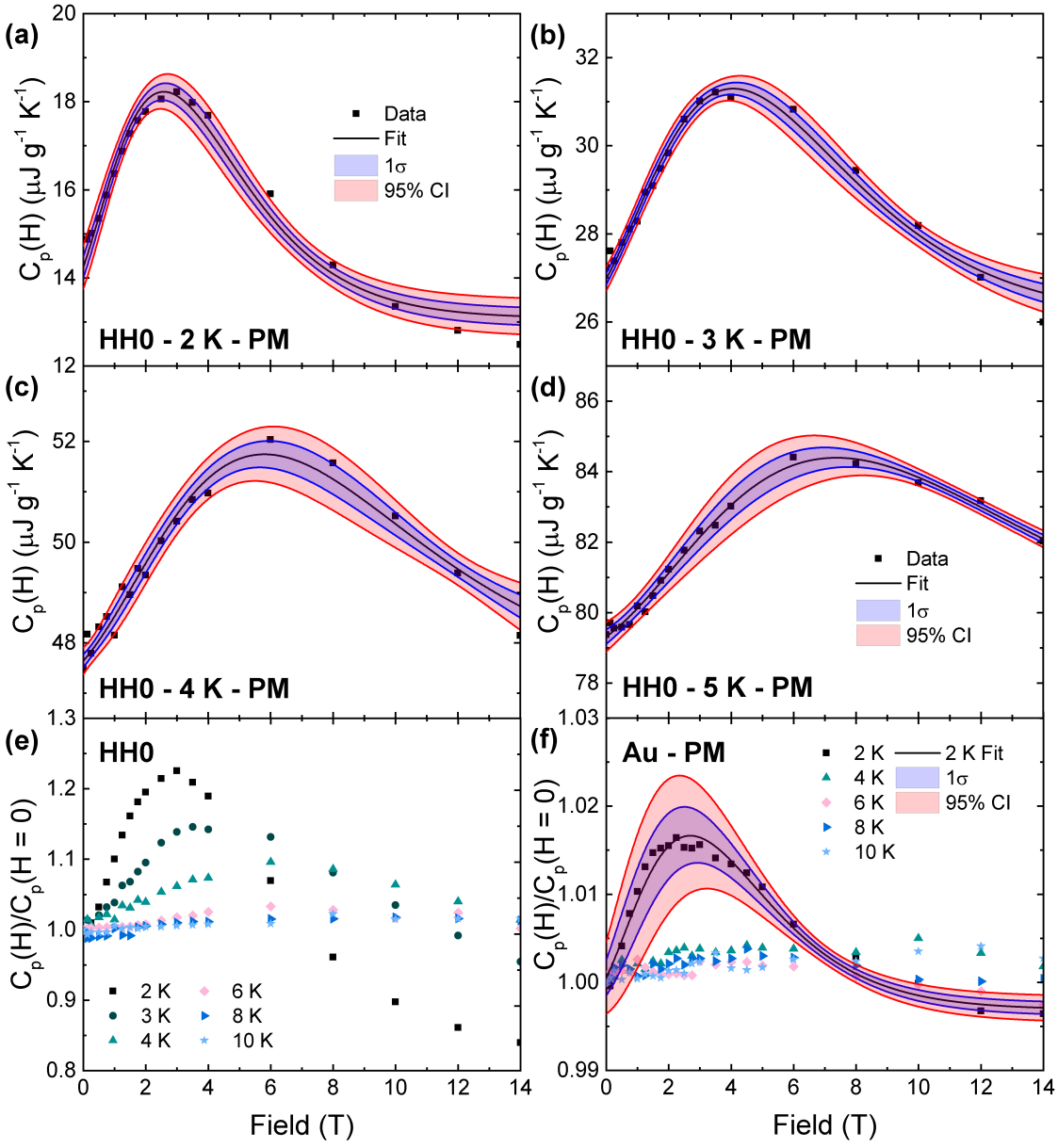

Figure 5.2: **Paramagnon analysis of the specific heat data of HH0, and the normalized values for Au.** (a)-(d) Experimental data (black squares) for HH0 ranging temperatures from 2 to 5 K, respectively. The 95% confidence intervals (red shading) and 1σ deviations (blue shading) for the fits to the PM (paramagnons) model (solid black line) are also included. (e) and (f) are normalized heat capacities as a function of magnetic field at several temperatures for HH0 and Au, respectively.

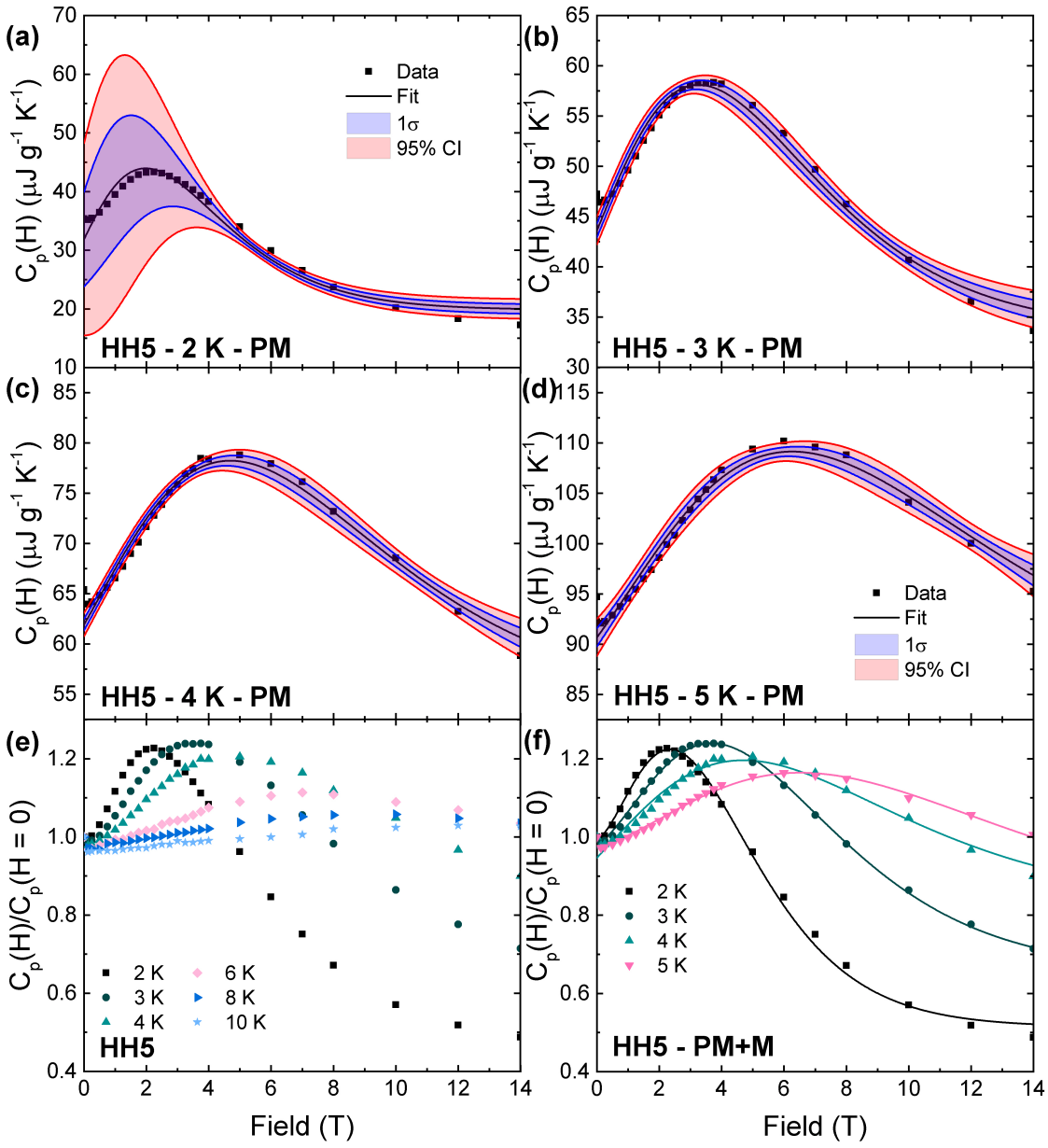

Figure 5.3: **Paramagnon and magnon analysis of the specific heat data of HH5.** (a)-(d) Experimental data (black squares) for HH5 ranging temperatures from 2 to 5 K, respectively. The 95% confidence intervals (red shading) and 1σ deviations (blue shading) for the fits to the PM (paramagnons) model (solid black line) are also included. (e) Normalized heat capacity as a function of magnetic field at several temperatures for HH5. (f) Best fits of the PM+M (paramagnons and magnons) model to the $C_p(H)$ of HH5 ranging temperatures from 2 to 5 K. Confidence intervals for the fits in (f) were not calculable.

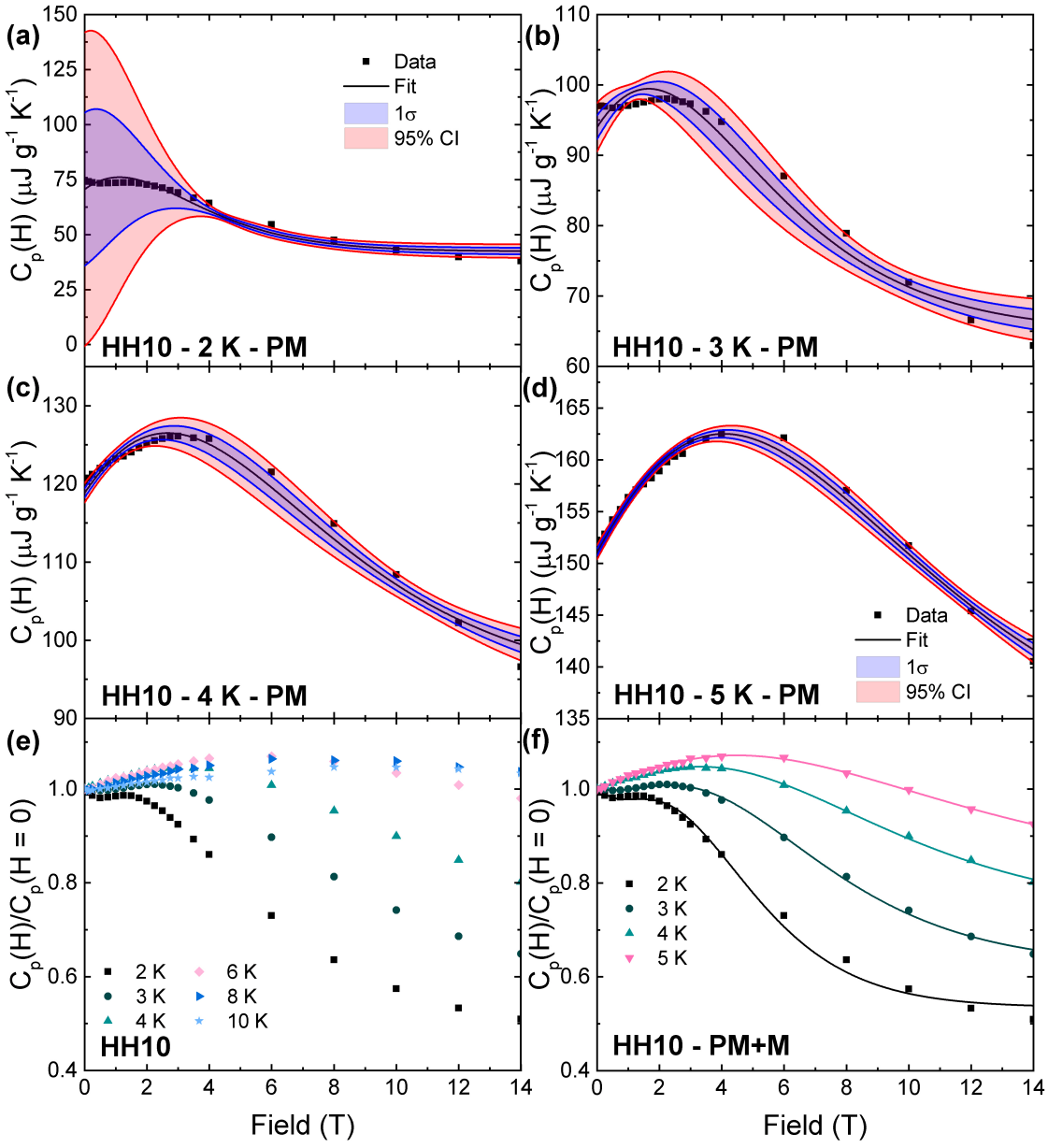

Figure 5.4: **Paramagnon and magnon analysis of the specific heat data of HH10.** (a)-(d) Experimental data (black squares) for HH10 ranging temperatures from 2 to 5 K, respectively. The 95% confidence intervals (red shading) and 1σ deviations (blue shading) for the fits to the PM (paramagnons) model (solid black line) are also included. (e) Normalized heat capacity as a function of magnetic field at several temperatures for HH10. (f) Best fits of the PM+M (paramagnons and magnons) model to the $C_p(H)$ of HH10 ranging temperatures from 2 to 5 K. Confidence intervals for the fits in (f) were not calculable.

$C_p(H)$ behavior of HH5 and HH10 at 2 and 3 K. Attempts to fit the data to a spin cluster model, as a way of accounting for both the intercluster and intracluster interactions of the magnetic secondary phases in HH5 and HH10, were equally unsuccessful. Additional information on the spin cluster model can be found in Section 5.4.3. To entirely eliminate D as a free parameter in the PM+M model, future work could utilize either first-principles calculations or inelastic neutron scattering experiments to assess the spin stiffness of the $TiNi_{4/3}Fe_{2/3}Sn$ phase. That way, the impact of $C_{p,ferro}(H)$ could be readily determined without any fitting.

To further explore the unique trends of $C_p(H)$ in the Fe-added samples at the lowest temperatures, we measured the heat capacity of HH10 down to 0.36 K using the He-3 option of the PPMS. The results are shown in Figure 5.5. Although no evident peak as a function of temperature occurs in C_pT^{-1} (Fig. 5.5(a)) at zero field, the application of a 1 T magnetic field does create a maximum around 0.6 K. The peak shifts to higher temperatures and broadens as larger magnetic fields are applied. Maxima in C_pT^{-1} versus T^2 at such low temperatures are often labeled as "Schottky peaks" and described by a generic energy level splitting that can result from nuclear or electronic magnetic moments. The impact of the spin-1/2 Schottky phenomenon on the heat capacity can be found in Refs. [24, 28, 37] and is given by

$$C_{p,Sch} = n_{Sch}k_B\left(\frac{2ye^y}{e^{2y}+1}\right)^2 = n_{Sch}k_By^2\left(\frac{2}{e^y+e^{-y}}\right)^2 = n_{Sch}k_By^2\text{sech}^2y. \tag{5.2}$$

Eq. 5.2 is exactly Eq. 5.1 for $J = 1/2$, seen by using a number of hyperbolic trigonometric function identities ($\sinh 2y = 2\sinh y\cosh y$ and $\cosh^2 y - \sinh^2 y = 1$) as follows

$$\begin{aligned} C_{p,para}(J=1/2) &= -n_Ik_By^2\left(\frac{4}{\sinh^2 2y} - \frac{1}{\sinh^2 y}\right) = -n_Ik_By^2\left(\frac{1-\cosh^2 y}{\sinh^2 y\cosh^2 y}\right) \\ &= n_Ik_By^2\text{sech}^2y. \end{aligned} \tag{5.3}$$

More generically, it is not too difficult to show that the multi-level paramagnon expression (Eq. 5.1) is equivalent to a multi-level Schottky phenomenon with the number of non-degenerate levels set by the angular momentum, $N = 2J + 1$, an expression for which can be found in Ref. [163]. The presence of the so-called "Schottky peak" in the temperature-dependent C_pT^{-1} at the lowest temperatures, and its equivalence with the paramagnon perspective, is assuring that our analysis of the $C_p(H)$ in terms of the PM model is a correct approach, even for HH5 and HH10 below 4 K.

We plot the normalized best fits to the $C_p(H)$ of HH10 at temperatures below 2 K in Fig. 5.5(b). The corresponding confidence intervals are shown in Figure 5.6, while the best-fit parameters are listed in Table 5.1 of Section 5.4.1. The reemergence of a sharp maximum in the heat capacity as a function of magnetic field at the lowest temperatures (Fig. 5.5(b)) is further support that the PM model is appropriate for analyzing $C_p(H)$ since the peak amplitude grows with

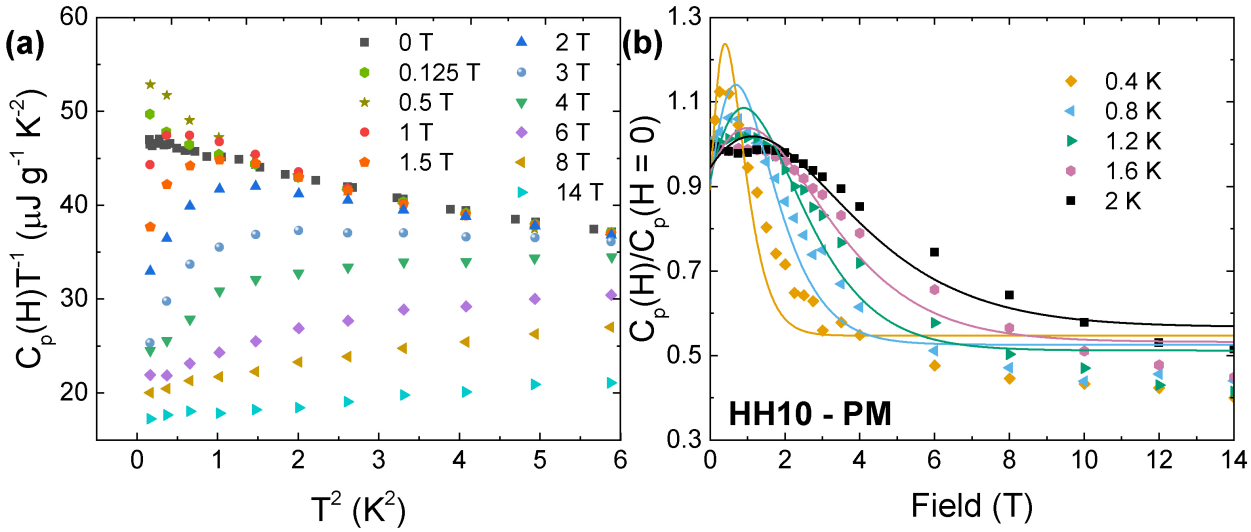

Figure 5.5: **Specific heat data of HH10 at temperatures below ≈ 2.4 K.** (a) $C_p(H)T^{-1}$ against T^2 for HH10 at a number of magnetic fields. (b) Normalized heat capacity as a function of magnetic field at several temperatures for HH10 with the best fits of the PM model. Confidence intervals for the fits in (b) are displayed in Figs. 5.4 and 5.6.

decreasing temperature. However, the poor fits and large confidence intervals (Fig. 5.6) confirm that a separate effect is impacting the $C_p(H)$, as we already expected from the 2 and 3 K data. The unique phenomenon of $C_p(H)$ in HH10 at low fields and temperatures is not noticed in the temperature dependence of C_p at set fields (Figs. 5.5 and 5.7), highlighting the importance of the field-dependent measurement.

In our previous work (Chapter 4, Ref. [159]), we identified a magnetotransport effect in the samples at the lowest temperatures (< 4 K) that we attributed to weak anti-localization (WAL). The lowered electrical resistivity required fields of ≈ 1 T at 2 K to return to the normal electronic state, which we argued ruled out the presence of superconducting Sn-based binary compounds. Looking at the drop in $C_p(H)$ at 2 K, we see that it coincidentally stops at around 1 T, after which the expected rise and fall of the PM model kicks in. Furthermore, the inexplicable $C_p(H)$ trend at low fields in HH5 and HH10 occurs only below 4 K, exactly as the magnetotransport effect. The WAL state heat capacity manifests iteself as either a field-dependent electronic contribution, $\gamma(H)T$, or a Schottky-like form [134, 164, 165]. In Section 5.4, Figure 5.8(a), we demonstrate that γ is mainly independent of magnetic field for all of the samples. Further, the presence of another Schottky-like term, in addition to the paramagnon contribution, would magnify the $C_p(H)$ enhancement with field upon decreasing the temperature from 2 K, contrary to the decline in $C_p(H)$ at low fields and temperatures (Fig. 5.5(b)).

Elemental superconductors can exhibit enhanced critical fields when their spatial extent is reduced to the nanoscale. For example, indium nanoparticles of diameter < 50 nm exhibit critical

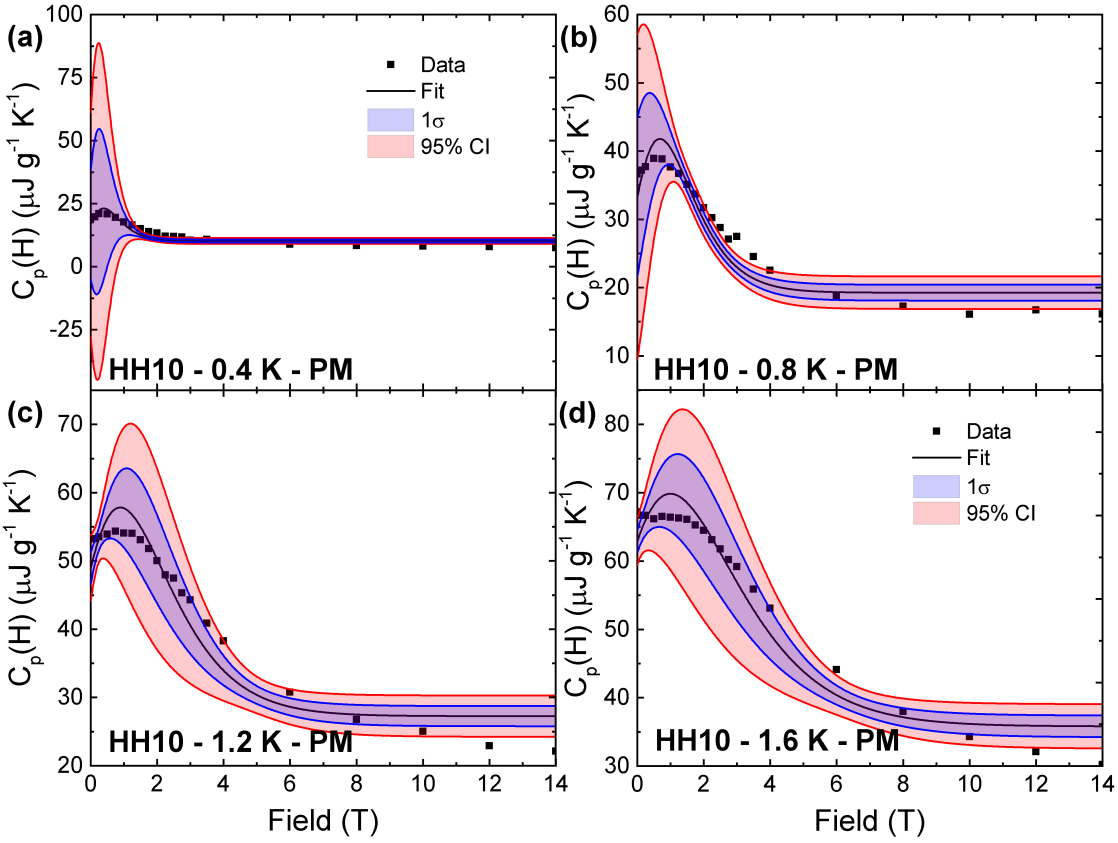

Figure 5.6: **Paramagnon analysis of the specific heat data of HH10 at temperatures from 0.4 K to 1.6 K.** (a)-(d) Experimental data (black squares) for HH10 ranging temperatures from 0.4 K to 1.6 K, respectively. The 95% confidence intervals (red shading) and 1σ deviations (blue shading) for the fits to the PM (paramagnons) model (solid black line) are also included.

fields up to $\approx$ 10 T [166], and similarly sized tin nanowires require fields of $\approx$ 2 T to return to the normal resistive state at 2 K [167]. In general, cooling through the superconducting transition results in an increased state of heat capacity. Applying magnetic fields in the superconducting state constantly diminishes $C_p(H)$ until reaching the normal state [168, 169]. Such a decline could account for the low-field behavior of the heat capacity of HH5 and HH10 at temperatures lower than 4 K. Although we did not detect any Sn-based binaries in the microscopy of the samples [98], it is possible that such nanoscale phases could go unnoticed if in small concentrations. Because the introduction of Fe adds further chemical disorder to the compound and increases the phase separation, certain Sn-based binaries could become more energetically favorable as the alloy demixes. We believe the greater likelihood of Sn-based superconducting binaries in HH5 and HH10 could therefore at least qualitatively explain the unique $C_p(H)$ behavior seen below 4 K.

5.4 Modeling of $C_p(H,T)$

To understand the behavior of the heat capacity data as a function of magnetic field, we explored a number of physical models. Our goal was to find the most intuitive description with the least free parameters that fit the experimental data with narrow confidence intervals.

The three models described below are labeled as: PM (paramagnons), PM+M (paramagnons and magnons), and PM+C (paramagnons and spin clusters). In the analysis of the experimental data, we assume that the electronic coefficient, γ, and the phononic coefficient, β, in the fitting are independent of magnetic field and temperature. In other words, at each temperature of the analysis, we take $C_p(H,T_0) = A(T_0) + f(H,T_0)$, where $A(T_0)$ is a constant equal to the sum of the electronic and phononic contributions, $A(T_0) = \gamma T_0 + \beta T_0^3$, and $f(H,T_0)$ is the magnetic contribution based on the individual models. Without making any assumption about the model $f(H,T)$, we can assess the $C_p(H,T)T^{-1}$ vs T^2 for the different magnetic fields, shown in Figure 5.7(b), (d), (f), and (h). The slope of the data at temperatures $\approx$ 7 to 10 K, where the non-linearities are essentially absent, reflects the coefficient β. Visually, it seems that β is influenced slightly by the field but not overwhelmingly so, nor consistently from sample to sample. Because phonons are not charged, their interaction with magnetic fields is typically considered to be neglible unless mediated by strong phonon-electron coupling or phonon-induced diamagnetism [170, 171]. Other sources of heat capacity can exhibit a T^3 dependence that is field dependent, such as spin fluctuations in nearly ferromagnetic alloys [172]. However, we will soon show that β is mainly independent of field (Figure 5.8(b)) so we have no reason to consider such phenomena.

Regarding the electronic contribution for the HH5 and HH10 samples, we do notice a changing y-intercept of the $C_p(H,T)T^{-1}$ vs T^2 plots for the different magnetic fields, again without assuming any form for $f(H,T)$. A field-dependent γ is not unprecedented, having been reported in weakly ferromagnetic compounds [170, 173] and superconductors [152]. Based on an electron+phonon model applied to the $C_p(H = 0, T : [2,10]$ K) data (Fig. 5.7(a), (c), (e), and (g)), the electronic contribution to C_p becomes greater in magnitude than the phonon contribution at temperatures less than $\approx$ 3 K (6 K) in the HH5 (HH10) samples, whereas $C_{p,elec} < C_{p,latt}$ for HH0 down to 2 K. The greater weight of $C_{p,elec}$ at lower temperatures for the Fe-added samples is in agreement with the apparent magnetic field sensitivity of the y-intercept of $C_p(H,T)T^{-1}$ vs T^2 for those samples (Figs. 5.7(d) and (f)). In other words, as the electronic contribution becomes a significant portion of C_p at the lowest temperatures, the potential magnetic field dependence of γ is more visible. However, the merely visual analysis and simplistic electron+phonon model can be heavily influenced by the effect that causes the upturn in C_p at the lowest temperatures. Basically, the apparent dependence of γ and β on the magnetic field may be an artifact of the dependence of $f(H,T)$ on magnetic field.

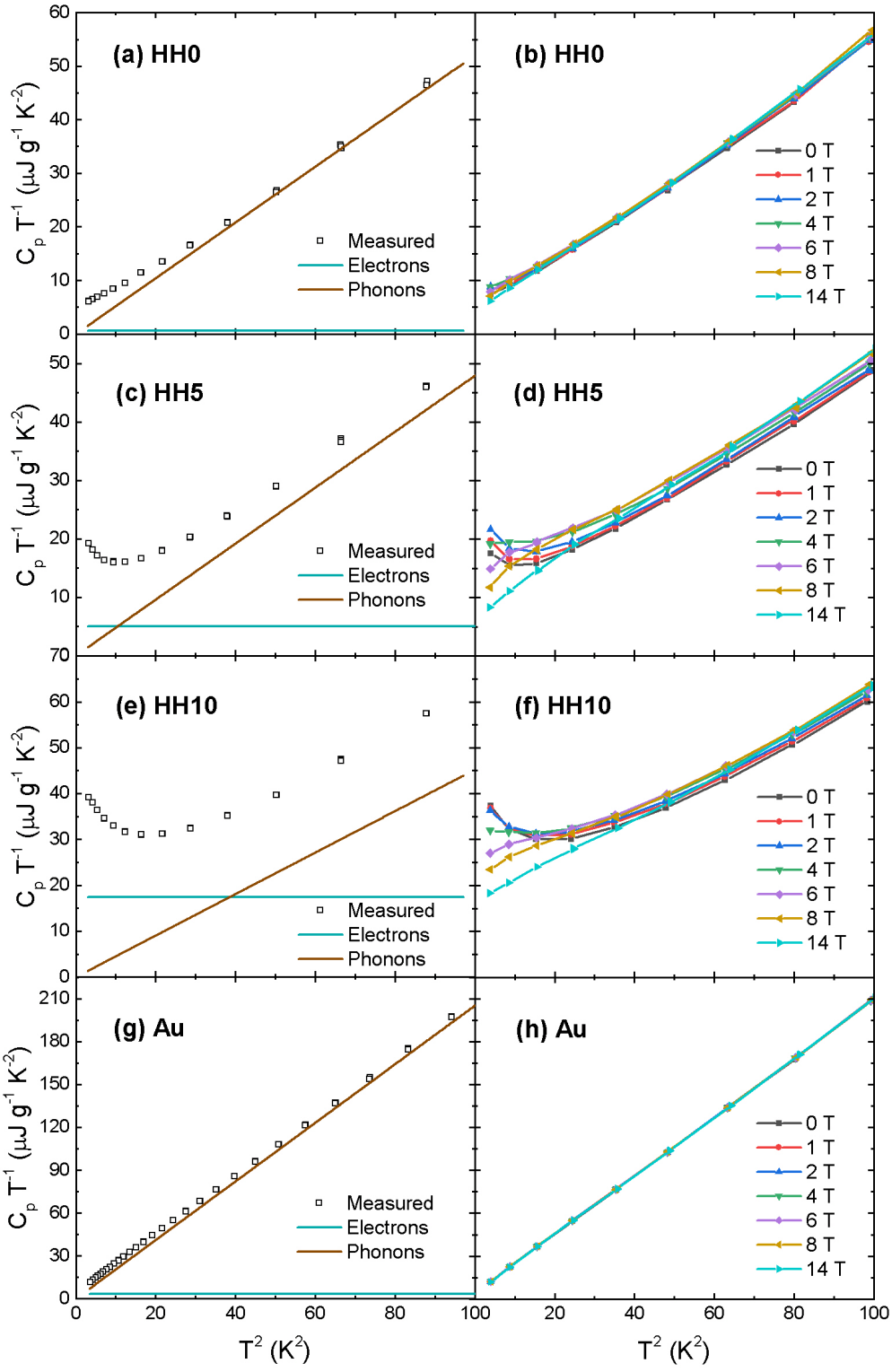

Figure 5.7: **Zero-field electron and phonon contributions to the heat capacity of the half-Heusler composites and Au, and temperature-dependent specific heat at a variety of magnetic fields.** At zero magnetic field ((a), (c), (e), and (g)), the data is fit with a model that simply accounts for electron and phonon contributions, which are shown individually. (b), (d), (f), and (h) illustrate the field-dependent C_pT^{-1} at temperatures lower than 10 K.

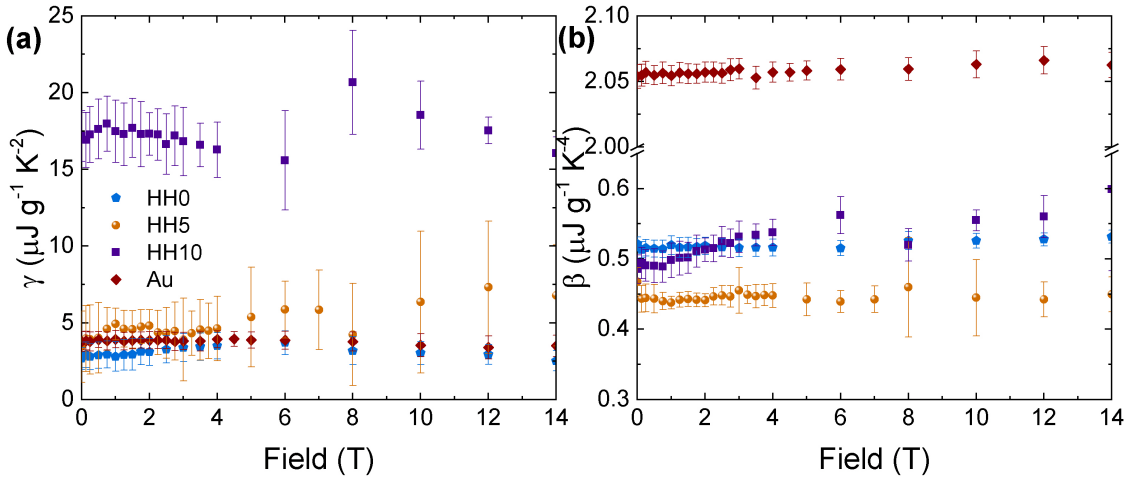

Figure 5.8: **Magnetic field-dependent electron and phonon coefficients of the $\mathbf{Ti_{0.25}Zr_{0.25}Hf_{0.50}NiFe_xSn_{0.975}Sb_{0.025}}$ samples and Au.** (a) The electronic coefficient, γ, and (b) the phononic coefficient, β. The coefficients are extracted from an electron+phonon+paramagnon model fit to the temperature-dependent C_p data at each field.

Once we identified the PM model as the most appropriate $f(H,T)$ for the fitting of $C_p(H)$ for all of the samples (Section 5.3.2), we fit C_p as a function of temperature from 2 to 10 K for each magnetic field used during the study. The resultant $\gamma(H)$ and $\beta(H)$ shown in Fig. 5.8 demonstrate the overall lack of field dependence of the electronic and phononic terms, especially at low fields, which substantiates our approach to the modeling of $C_p(H)$. Up to about 4 T, the γ and β are mostly constant, with the exception of a slightly increasing ($\approx 10\%$) β for HH10, although still within the estimated error. At higher fields, the estimated coefficients become somewhat noisier as the least-squares solver struggles with the decreasing presence of the paramagnon term in the model.

5.4.1 Model PM: Paramagnons

The HH samples consists of regions of paramagnetism and diamagnetism, with HH5 and HH10 possessing additional ferromagnetic regions [98, 159]. The magnetic susceptibility at temperatures lower than 10 K shows a dominant signal from paramagnetism. $C_{p,para}$ is derived in Section 1.4.3 as Eq. 1.31 and reproduced in Section 5.3.2 as Eq. 5.1. From a particulate perspective, the heat capacity contribution is due to "paramagnons", so we label the model as PM. The PM model contains the following four free parameters: $A(T_0)$, n_I, J and $H_{int,para}$. To reduce the number of parameters to three, we set $J = 1/2$ for an electron with quenched orbital angular momentum in a bonding environment [162]. Although the corresponding confidence intervals are larger than those of the J-free model, the estimated parameters are more consistent as a function of temperature. For example, the J-free model solution for HH0 yields values of J that are $O(10^{-3})$ to $O(10^{0})$ at

Table 5.1: Fitting parameters extracted from the comparison of the heat capacity data for the half-Heusler samples and Au (Figs. 5.1 and 5.6) to Eq. 5.1.

Sample	T_0 (K)	$A(T_0)$ (μJ g^{-1} K^{-1})	n_I (10^{16} g^{-1})	$H_{int,para}$ (T)	Δ J
HH0	2	13.1	84.9±19.0	0.99±0.23	0.13
	3	26.1	86.3±17.6	1.29±0.10	0.13
	4	47.1	76.1±23.9	1.34±0.19	0.14
	5	78.8	92.6±29.5	1.55±0.69	0.22
HH5	2	19.8	398±58.9	1.60±0.08	0.37
	3	33.7	403±69.6	2.10±0.15	0.10
	4	54.0	400±97.0	2.45±0.15	0.13
	5	84.2	411±99.7	2.67±0.14	0.14
HH10	2	42.4	556±116	2.45±0.20	0.75
	3	64.9	570±137	3.70±0.16	0.14
	4	93.7	541±125	4.48±0.33	0.13
	5	130	540±103	4.86±0.39	0.10
	0.4	10.2	213±60	0.32±0.15	0.96
	0.8	19.3	372±101	0.75±0.38	0.31
	1.2	27.3	504±112	1.25±0.25	0.77
	1.6	35.8	562±178	1.86±0.30	0.54

different temperatures, which is not physically reasonable.

The best fits of the PM model to the $C_p(H)$ of HH0 are shown for 2 to 5 K in Fig. 5.2(a)-(d), along with the calculated confidence intervals. The normalized heat capacity data, $C_p(H)/C_p(H = 0)$, for HH0 from 2 to 10 K is shown in Fig. 5.2(e). The fit parameters collected in Table 5.1 indicate the number of paramagnetic centers to be around 8.5 x 10^{17} per gram of HH0. Based on the molecular weight of the compound ($\approx$ 300 grams per mol), there are approximately 4 paramagnetic centers of strength μ_B for every 10000 unit cells. Because none of the intentional dopants are at such a low level, the $C_p(H)$ effect likely stems from trace impurities introduced during the synthesis of the compounds. An alternative explanation is that the phase separation native to these composites naturally hosts unpaired electrons at the grain boundaries, where defects are in abundance.

To see how well a paramagnon-only model can capture the $C_p(H,T)$ of the HH5 and HH10 samples that contain ferromagnetic regions, we fit the sample data with the PM model. The best fits and corresponding confidence intervals for HH5 and HH10 for temperatures of 2 to 5 K are displayed in Figs. 5.3(a)-(d) and 5.4(a)-(d), respectively. The normalized heat capacity data for HH5 and HH10 from 2 to 10 K are shown in Figs. 5.3(e) and 5.4(e), respectively. The fit parameters are tabulated in Table 5.1. The paramagnon concentration is in the mid 10^{18} per gram, amounting

to about 1 for every 500 formula units of the compounds. Although n_I is at a higher level than HH0 (1 every 2500 unit cells), the concentration still does not correspond to any element within the compound. The added Fe amplifies the effect from the base sample either through additional impurities or the enhanced phase separation that its presence drives within the composites.

5.4.2 Model PM+M: Paramagnons and Magnons

Because HH5 and HH10 both consist of paramagnetic and ferromagnetic phases at the nano- and micro-scale, we sought to understand the role of the ferromagnetic equivalent of paramagnons, i.e. "magnons", in the heat capacity. I derive the magnon contribution, $C_{p,ferro}(H,T)$, here.

Like phonons (Section 1.4.1), magnons are bosons, but without the different polarizations. Following Refs. [24, 28, 147, 174], we can write down the total energy of the magnons, similar to Eq. 1.19 as

$$U_{ferro} = \hbar \sum_k n_k \omega_k = \frac{V}{8\pi^3} \int \frac{\hbar\omega_k dk^3}{\exp\left(\mathscr{T}\hbar\omega_k\right) - 1} = \frac{V}{8\pi^3} \int \hbar\omega_k dk^3 \sum_{p=1}^{\infty} e^{-p\mathscr{T}\hbar\omega_k}, \tag{5.4}$$

where ω_k is the frequency of the magnon with momentum k, and the integral is over all of k-space. We have made the substitution $\mathscr{T}^{-1} = k_B T$ for ease of reading. The last equality replaces the Bose distribution with an infinite series by

$$\begin{aligned} \sum_{p=1}^{\infty} e^{-px} &= e^{-x} + e^{-2x} + e^{-3x} + \cdots = e^{-x}(1 + e^{-x} + e^{-2x} + \cdots) = e^{-x}\left(1 + \sum_{p=1}^{\infty} e^{-px}\right) \\ &\implies \sum_{p=1}^{\infty} e^{-px} = \frac{e^{-x}}{1 - e^{-x}} = \frac{1}{e^x - 1}. \end{aligned} \tag{5.5}$$

The dispersion relation for ω_k, or how it depends functionally on the momentum, is typically taken from an Ising model calculation without the presence of an applied field, such that $\hbar\omega_k \approx Dk^2$ in three dimensions [24, 28, 147, 174]. To include the magnetic field and higher order terms of the momentum, we combine two separate calculations from Ref. [174] to perform an original derivation with the following dispersion relation

$$\hbar\omega_k = Dk^2 + Dc_1k^4 + Dc_2(k_x^4 + k_y^4 + k_z^4) + g\mu_B H. \tag{5.6}$$

In Eq. 5.6, D is known as the "spin stiffness", and c_1 and c_2 are constants characterizing the quartic dispersion terms. We will link these terms to crystal symmetries and neutron diffraction studies momentarily. The magnetic term is similar to Eq. 1.13, again with g the unitless Landé g-factor that is approximately 2 for electrons and $\mu_B = 9.274$ x 10^{-24} Joules per Tesla the Bohr magneton.

We proceed by inserting Eq. 5.6 into Eq. 5.4 and expanding the integrals to include all directions k_x, k_y, and k_z with bounds $(-\infty, +\infty)$.

$$\begin{aligned} U_{ferro} &= \frac{V}{8\pi^3} \iiint dk_x\, dk_y\, dk_z \hbar\omega_k \sum_{p=1}^{\infty} e^{-p\mathscr{T}(Dk^2+g\mu_B H)} e^{-p\mathscr{T}[Dc_1k^4+Dc_2(k_x^4+k_y^4+k_z^4)]} \\ &\approx \frac{V}{8\pi^3} \sum_{p=1}^{\infty} e^{-p\mathscr{T}g\mu_B H} \iiint dk_x\, dk_y\, dk_z \hbar\omega_k e^{-p\mathscr{T}Dk^2} [1 - p\mathscr{T}Dc_1k^4 - p\mathscr{T}Dc_2(k_x^4+k_y^4+k_z^4)], \end{aligned} \tag{5.7}$$

In the second line of Eq. 5.7, we have assumed that the quartic correction terms are small so that the exponential can be expanded, i.e. $e^x \approx 1 + x$ for $x \ll 1$. Considering the constituents of $\hbar\omega_k$ (Eq. 5.6), we can assess the product within the integral of Eq. 5.7 and keep all terms up to $O(k^4)$. We find

$$U_{ferro} = \frac{V}{8\pi^3} \sum_{p=1}^{\infty} e^{-p\mathscr{T}g\mu_B H} \iiint dk_x\, dk_y\, dk_z e^{-p\mathscr{T}D(k_x^2+k_y^2+k_z^2)} \mathscr{I}(H; k_x, k_y, k_z), \tag{5.8}$$

with

$$\begin{aligned} \mathscr{I}(H; k_x, k_y, k_z) &= Dk^2 + Dc_1k^4 + Dc_2(k_x^4+k_y^4+k_z^4) + g\mu_B H \\ &\quad - p\mathscr{T}g\mu_B H Dc_1k^4 - p\mathscr{T}g\mu_B H Dc_2(k_x^4+k_y^4+k_z^4) \\ &= D(k_x^2+k_y^2+k_z^2) + Dc_1(1-p\mathscr{T}g\mu_B H)(k_x^2+k_y^2+k_z^2)^2 + g\mu_B H \\ &\quad + Dc_2(1-p\mathscr{T}g\mu_B H)(k_x^4+k_y^4+k_z^4) \\ &= D(k_x^2+k_y^2+k_z^2) + 2Dc_1(1-p\mathscr{T}g\mu_B H)(k_x^2k_y^2+k_x^2k_z^2+k_y^2k_z^2) + g\mu_B H \\ &\quad + D(c_1+c_2)(1-p\mathscr{T}g\mu_B H)(k_x^4+k_y^4+k_z^4), \end{aligned} \tag{5.9}$$

where we have used the fact that $k^2 = k_x^2 + k_y^2 + k_z^2$. Each term in the integrand (Eq. 5.9) becomes related to the Gaussian integral when inserted in Eq. 5.8, which can be solved using the following

$$\mathcal{I}_j = \int_{-\infty}^{\infty} x^j e^{-ax^b} dx = \frac{2\,\Gamma((j+1)/b)}{b a^{(j+1)/b}}, \tag{5.10}$$

for the even j of interest here. In Eq. 5.8, $a = p\mathscr{T}D$ and $b = 2$. Recall that Gamma function follows $\Gamma(j+1) = j\Gamma(j)$. With $\Gamma(1/2) = \sqrt{\pi}$, then $\Gamma(3/2) = \sqrt{\pi}/2$ and $\Gamma(5/2) = 3\sqrt{\pi}/4$.

Because the integration in Eq. 5.8 is identical for k_x, k_y, and k_z, the terms that add individual directions in Eq. 5.9 will yield a factor of 3. Furthermore, when a particular direction is not represented in the integrand terms, it still contributes a factor of $\mathcal{I}_0$. For example, the $g\mu_B H$ term in Eq. 5.9 yields $g\mu_B H\mathcal{I}_0^3$ when integrated in Eq. 5.8. With these two rules in mind, we can combine Eqs. 5.8 - 5.10 to write

$$
\begin{aligned}
U_{ferro} &= \frac{V}{8\pi^3}\sum_{p=1}^{\infty} e^{-p\mathscr{T}g\mu_B H}\left\{3D\left[\mathcal{I}_2\mathcal{I}_0^2 + 2c_1(1-p\mathscr{T}g\mu_B H)\mathcal{I}_2^2\mathcal{I}_0\right.\right. \\
&\qquad \left.\left. +(c_1+c_2)(1-p\mathscr{T}g\mu_B H)\mathcal{I}_4\mathcal{I}_0^2\right] + g\mu_B H\mathcal{I}_0^3\right\} \\
&= \frac{V}{8\pi^3}\sum_{p=1}^{\infty} e^{-p\mathscr{T}g\mu_B H}\left\{3D\left[\left(\frac{\sqrt{\pi}}{2}\right)(pD\mathscr{T})^{-\frac{3}{2}}\pi(pD\mathscr{T})^{-1}\right.\right. \\
&\qquad + 2c_1(1-p\mathscr{T}g\mu_B H)\left(\frac{\pi}{4}\right)(pD\mathscr{T})^{-3}\pi^{\frac{1}{2}}(pD\mathscr{T})^{-\frac{1}{2}} \\
&\qquad \left.\left. + (c_1+c_2)(1-p\mathscr{T}g\mu_B H)\left(\frac{3\sqrt{\pi}}{4}\right)(pD\mathscr{T})^{-\frac{5}{2}}\pi(pD\mathscr{T})^{-1}\right] \right. \\
&\qquad \left. + g\mu_B H\pi^{\frac{3}{2}}(pD\mathscr{T})^{-\frac{3}{2}}\right\} \\
&= \frac{V}{8\pi^{3/2}}\sum_{p=1}^{\infty} e^{-p\mathscr{T}g\mu_B H}\left\{3D\left[\frac{1}{2}(pD\mathscr{T})^{-\frac{5}{2}} + \frac{1}{4}(5c_1+3c_2)(1-p\mathscr{T}g\mu_B H)(pD\mathscr{T})^{-\frac{7}{2}}\right]\right. \\
&\qquad \left. + g\mu_B H(pD\mathscr{T})^{-\frac{3}{2}}\right\}, \qquad (5.11)
\end{aligned}
$$

where we have collected the terms of $pD\mathscr{T}$ together in the last equality. To rewrite the sums in Eq. 5.11, we can use the Bose-Einstein integrals, defined as

$$
\mathscr{F}(j,t_H) = \frac{1}{\Gamma(j)}\int_0^{\infty}\frac{x^{j-1}dx}{\exp\left(x+t_H^{-1}\right)-1} = \sum_{p=1}^{\infty} p^{-j}e^{-p/t_H}. \qquad (5.12)
$$

In Eq. 5.11, $t_H = k_BT/g\mu_BH$. We can pull out the $(D\mathscr{T})^{-3/2}$ in the last equality of Eq. 5.11 and insert the Bose-Einstein integrals to yield

$$
\begin{aligned}
U_{ferro} &= \frac{V}{(4\pi D\mathscr{T})^{3/2}}\left\{\frac{3}{2}\mathscr{T}^{-1}\mathscr{F}\left(\frac{5}{2},t_H\right) + g\mu_B H\mathscr{F}\left(\frac{3}{2},t_H\right)\right. \\
&\qquad \left. +\frac{3D}{4}(5c_1+3c_2)\left[\mathscr{F}\left(\frac{7}{2},t_H\right) - \mathscr{T}g\mu_B H\mathscr{F}\left(\frac{5}{2},t_H\right)\right](D\mathscr{T})^{-2}\right\} \\
&= V\left(\frac{k_BT}{4\pi D}\right)^{\frac{3}{2}}\left\{g\mu_B H\mathscr{F}\left(\frac{3}{2},t_H\right) + 3k_BT\left[\frac{1}{2} - \frac{5c_1+3c_2}{4D}(g\mu_B H)\right]\mathscr{F}\left(\frac{5}{2},t_H\right)\right. \\
&\qquad \left. + \frac{3(k_BT)^2}{4D}(5c_1+3c_2)\mathscr{F}\left(\frac{7}{2},t_H\right)\right\}. \qquad (5.13)
\end{aligned}
$$

In the last equality of Eq. 5.13, we have substituted back in $\mathscr{T}^{-1} = k_BT$ and organized the terms with common powers of k_BT and orders of $\mathscr{F}(j,t_H)$.

Now, we can calculate the heat capacity by taking the temperature derivative of Eq. 5.13. Recalling that $t_H = k_BT/g\mu_BH$, we will require the temperature derivative of the Bose-Einstein

integrals as follows

$$\frac{d}{dT}\mathscr{F}(j,t_H) = \frac{d}{dT}\sum_{p=1}^{\infty} p^{-j}e^{-p/t_H} = \frac{g\mu_B H}{k_B T^2}\sum_{p=1}^{\infty} p^{-j+1}e^{-p/t_H} = \frac{g\mu_B H}{k_B T^2}\mathscr{F}(j-1,t_H). \quad (5.14)$$

The heat capacity is then

$$\begin{aligned}
C_{p,ferro} = {} & \frac{3VT^{\frac{1}{2}}}{2}\left(\frac{k_B}{4\pi D}\right)^{\frac{3}{2}}\left\{g\mu_B H\mathscr{F}\left(\frac{3}{2},t_H\right) + 3k_BT\left[\frac{1}{2} - \frac{5c_1+3c_2}{4D}(g\mu_B H)\right]\mathscr{F}\left(\frac{5}{2},t_H\right)\right. \\
& \left. + \frac{3(k_BT)^2}{4D}(5c_1+3c_2)\mathscr{F}\left(\frac{7}{2},t_H\right)\right\} \\
& + V\left(\frac{k_BT}{4\pi D}\right)^{\frac{3}{2}}\left\{\frac{1}{k_B}\left(\frac{g\mu_B H}{T}\right)^2\mathscr{F}\left(\frac{1}{2},t_H\right)\right. \\
& + \left[\frac{1}{2} - \frac{5c_1+3c_2}{4D}(g\mu_B H)\right]\left[3k_B\mathscr{F}\left(\frac{5}{2},t_H\right)\frac{3g\mu_B H}{T}\mathscr{F}\left(\frac{3}{2},t_H\right)\right] \\
& \left. + \frac{3k_B^2T}{2D}(5c_1+3c_2)\mathscr{F}\left(\frac{7}{2},t_H\right) + \frac{3k_Bg\mu_B H}{4D}(5c_1+3c_2)\mathscr{F}\left(\frac{5}{2},t_H\right)\right\} \\
= {} & VT^{\frac{1}{2}}\left(\frac{k_B}{4\pi D}\right)^{\frac{3}{2}}\left\{\frac{(g\mu_B H)^2}{k_BT}\mathscr{F}\left(\frac{1}{2},t_H\right) + g\mu_B H\left[3 - \frac{5c_1+3c_2}{4D}(g\mu_B H)\right]\mathscr{F}\left(\frac{3}{2},t_H\right)\right. \\
& + \frac{21k_BT}{2}\left[\frac{5}{14} - \frac{5c_1+3c_2}{4D}(g\mu_B H)\right]\mathscr{F}\left(\frac{5}{2},t_H\right) \\
& \left. + \frac{21(k_BT)^2}{8D}(5c_1+3c_2)\mathscr{F}\left(\frac{7}{2},t_H\right)\right\}. \quad (5.15)
\end{aligned}$$

To compare Eq. 5.15, which is an original result, to formulations by other authors for simpler dispersion relations, we can assess a few different limits of Eq. 5.15. For the typical $\hbar\omega_k = Dk^2$, we can set $c_1 = c_2 = 0$ and $H = 0$ for the magnon heat capacity without applied field, leaving only one term from Eq. 5.15

$$C_{p,ferro}^{quad}(H=0) = \frac{15V}{4}\left(\frac{k_BT}{4\pi D}\right)^{\frac{3}{2}}\zeta\left(\frac{5}{2}\right), \quad (5.16)$$

where $\mathscr{F}(j, t_H \to \infty) \to \zeta(j)$, the Riemann zeta function. Specifically, $\zeta(5/2) \approx 1.341$. Eq. 5.16 is a demonstration of the $T^{3/2}$ scaling for the magnon heat capacity in zero magnetic field, which is also derived in Refs. [24, 28, 147, 174, 175]. With a magnetic field present and quadratic dispersion, Eq. 5.15 becomes

$$C_{p,ferro}^{quad}(H \neq 0) = VT^{\frac{1}{2}} \left(\frac{k_B}{4\pi D}\right)^{\frac{3}{2}} \left[\frac{(g\mu_B H)^2}{k_B T} \mathscr{F}\left(\frac{1}{2}, t_H\right) + 3g\mu_B H \mathscr{F}\left(\frac{3}{2}, t_H\right) + \frac{15}{4} k_B T \mathscr{F}\left(\frac{5}{2}, t_H\right)\right], \tag{5.17}$$

as can be found in Refs. [174, 175].

Given the complexity of $C_{p,ferro}$ (Eq. 5.15), its value can surprisingly be calculated for ideal magnon systems if the spin stiffness, D, is measured. Inelastic neutron scattering experiments can map out the magnon dispersion and therefore extract D at low momenta. For example, pure Fe has $D = 281$ meVÅ^2 [176]. From Ref. [174], we are able to discern that for cubic lattices, the expression $5c_1 + 3c_2$ that appears repeatedly in Eq. 5.15 takes on a value of $-L^2/4$ when the ferromagnetic exchange interactions are held to nearest neighbors. L is the lattice parameter of a given cubic structure, values of which are commonly tabulated [177]. With knowledge of L, D, and the experimental conditions, $C_{p,ferro}$ can be calculated directly.

The magnon contribution to the heat capacity (Eq. 5.15) is directly added to the paramagnon contribution (Eq. 5.1) to model the magnetic field-dependent C_p of the Fe-added HH composites of the study, i.e. $C_p = C_{p,para} + C_{p,ferro}$. To include the possibility that the presence of a magnon secondary phase may create a magnetic field, $H_{int,para}$, in the intervening paramagnetic matrix, we maintain $H = H_{int,para} + H_{ext}$ in $C_{p,para}$, with H_{ext} the applied field from the PPMS within the experiment. For the $C_{p,ferro}$ term, Eq. 5.15, the only magnetic field is the applied one, $H = H_{ext}$. We label this model as PM+M (paramagnons and magnons). It has the following six free parameters: $A(T_0)$, n_I, J, $H_{int,para}$, V and D. By setting $J = 1/2$ for the paramagnetic component, as we did for the PM model, we reduce the number of free parameters to five. Last, we match the units of Eq. 5.15 to the experimental data by weighting the $C_{p,ferro}/V$ by a constant that is the volume of the magnon phase per mass of the sample, v_M. Related to the volume fraction of the sample that is magnonic, v_M is a free parameter in the model, taking the place of V in the previous list. The results of the fitting for HH5 and HH10 are shown in Figs. 5.3(f) and 5.4(f), respectively. Although the best fit curves match the experimental data well, the PM+M model is overfit. The total confidence intervals are incalculable, and the estimated errors on the fit parameters are orders of magnitude larger than the mean values themselves. Even setting v_M to a reasonable value to reduce the free parameter set does not allow the fitting algorithm to hone in on a D value with any certainty. Using Eq. 5.17 for the simplified quadratic dispersion does not improve the results.

5.4.3 Model PM+C: Paramagnons and Spin Clusters

Ideal Kondo systems, in which parts per million of magnetic elements are dissolved in non-magnetic elements, are similar in structure to the Fe-added TZHNSS composites. While the nano-

and micro-scale secondary magnetic phases in HH5 and HH10 are certainly not as dilute, we thought that heat capacity modeling of Kondo systems could be applied to the TZHNSS composites. The work of Levin and Mills [178] put forth a model of clusters of magnetic moments within a non-magnetic matrix, and even considered non-dilute alloys where clusters could contain hundreds of electronic spins. The model Hamiltonian is written as

$$\mathscr{H}_{cl} = -2\sum_{i,j} J_{dd}\vec{S}_i \cdot \vec{S}_j - \mu_B \sum_i \vec{H} \cdot \vec{S}_i - \sum_{i,e} J_{sd}\vec{S}_i \cdot s_e \delta(\vec{R}_i - \vec{R}_e). \tag{5.18}$$

The first term in Eq. 5.18 is the intracluster interactions by a short-range d-d exchange coupling of the spins within a given cluster, similar to Eq. 1.17 described in Section 1.3.4. Although the sum is over all of the spins in the system, the nearest neighbor aspect of J_{dd} restricts the sum to intracluster behavior. Intercluster interactions are included in the second term by way of a local magnetic field that originates from a molecular-field approximation in the case of ferromagnets or a weak anisotropy energy in the case of paramagnets. The last term of Eq. 5.18 includes the longer range s-d exchange between conduction electrons and the localized spins. These last two terms are what distinguish the spin cluster model from the physically separated, non-interacting, individual magnon contributions described by Eqs. 5.4, 5.6, and 5.15 in the paramagnons and magnons (PM+M) model.

In Ref. [178], the number of spins per cluster was considered to be a constant in order to attain semiquantitative agreement with the experimental resistivity and neutron scattering data of Cu-Ni samples. The geometric arrangement of the Ni spins within the clusters was taken as cubic, which is the case for the TZHNSS composites studied here (Section 5.3.1). At low temperatures ($T < T_C$ for ferromagnetic materials), the heat capacity can be expressed by incorporating the energy eigenfunctions of Eq. 5.18, which are solved for numerically, into the definition of the heat capacity (Eq. 1.18) to get the specific heat (heat capacity per mass) contribution from the clusters

$$C_{p,cl} = n_{cl} k_B y^2 \left[e^y (e^y - 1)^{-2} - (N_{cl} + 1)^2 e^{y(N_{cl}+1)} (e^{y(N_{cl}+1)} - 1)^{-2} \right]. \tag{5.19}$$

In Eq. 5.19, n_{cl} is the number of clusters per gram of material, N_{cl} is the number of spins in each cluster, and $y = \mu_B H / k_B T$. For the purposes of our study, n_{cl} is taken as a free parameter, and we set N_{cl} to certain values based on the approximate configuration we hoped to model. Here, $H = H_{int,cl} + H_{ext}$ includes the local fields developed by the spins, $H_{int,cl}$, in addition to the applied field, H_{ext}. The size of $H_{int,cl}$ determines whether the intercluster interactions are paramagnetic ($\lessapprox$ 50 mT at $T = 1$ K) or ferromagnetic (several Tesla at $T = 1$ K). Last, because $C_{p,cl}$ is the contribution to the heat capacity from the clusters and does not include the remaining matrix, we combine it with the paramagnetic contribution, Eq. 5.1, normalized by the mass for an overall $C_p = C_{p,para} + C_{p,cl}$. We label this model as PM+C (paramagnons and spin clusters). It has the

following seven free parameters: $A(T_0)$, n_I, J, $H_{int,para}$, n_{cl}, N_{cl} and $H_{int,cl}$. Given that the PM model is successful in fitting the higher temperature data in HH5 and HH10, we maintained the constant value of n_I determined at higher temperatures and kept the $J = 1/2$ for the paramagnetic term. Setting the value of N_{cl} for each fitting analysis reduced the number of free parameters to four.

Considering the magnetic secondary phase of $TiNi_{4/3}Fe_{2/3}Sn$ in the HH10 sample, its average areal extent determined by image analysis in Ref. [98] is approximately 460 μm^2. With the lattice parameter of the cubic secondary phase as $\approx$ 6.07Å, the number of unit cells fitting within an average spherical secondary phase would be $N_{cl} \approx 1$ x 10^{13}. The Ni and/or Fe within the cell serve as the sources of magnetic spins within the large clusters. Because the Ni and Fe are in a bonding environment in the secondary phase, their magnetic moments are not the full value of the bare elements. Therefore, we introduced a free parameter as the coefficient of μ_B within Eq. 5.19. As an alternative spin cluster, we considered the possibility of more dilute isolated regions of Fe and Ni. Our microstructure analysis (Section 5.3.1 and Ref. [98]) did not find evidence of such impurity phases, but such 1-3 nm regions could have been missed. Similar to Ref. [178], we set N_{cl} to appropriate values of 5 to 30 and ran the fitting analyses for HH5 and HH10. In either case of N_{cl}, the resultant fits could not capture the $C_p(H)$ behavior and produced best-fit parameters with standard deviations larger than their magnitudes. Fits of the PM+C model in which the constraints on the paramagnetic contribution were relaxed cut $C_{p,para}$ to a third of its value or less and returned values of $J = 1$. Such a scenario would be discontinuous from the higher temperature behavior and also require an orbital angular momentum value of 1/2, which is not physically reasonable. Thus, the spin cluster model does not help to explain the $C_p(H)$ trends at 2 K in HH5 and at 2 and 3 K in HH10.

5.4.4 Fitting Procedure and Error Analysis

The raw specific heat data in units of Joules per gram-Kelvin is a function of temperature at the magnetic fields used during the experiment. In order to compare the magnetic field dependence at specified temperatures (e.g., 2 to 10 K every 1 K), we set the PPMS to collect the specific heat data at those temperatures. The temperature of the sample when the specific heat was recorded was not exactly the desired temperature, e.g. 1.95 K instead of 2 K. This is a result of the time it takes for complete temperature stabilization upon cooling the PPMS from room temperature, the heating involved during the measurement, and also the different values of the heat capacity when different magnetic fields are applied. To adjust the sample temperature from the PPMS data file, T', to a consistent desired temperature, T_0, we first fit an electron+phonon model ($C_p(H = 0, T) = \gamma T + \beta T^3$, Eq. 1.30) to the finer zero-field data with $T : [T_0 - 1, T_0 + 1]$. By using the first-order

Taylor expansion of the C_p fit, we interpolated the value of $C_p(H, T_0)$ as $C_{p,data}(H, T') + (T_0 - T')(\gamma + 3\beta T'^2)$. With the correction in place, we can compare the specific heat as a function of magnetic field with confidence that the C_p values are at the exact same temperature.

When fitting a given model to experimental data, we use one of the least-squares solvers from Matlab known as 'lsqcurvefit'. From the solution at each data point, we can calculate the residual, or the absolute difference between the fit curve and the data, as well as the Jacobian, which is a matrix of partial derivatives of the model function with respect to its variables. The residuals and Jacobian can be input to the 'nlparci' function of Matlab to determine the 95% confidence intervals of the individual model parameters. To find the 95% confidence interval and 1σ standard deviation ($\approx$ 68% confidence interval) of the overall fit, we use the Matlab function 'nlpredci' that also requires the residuals and Jacobian as arguments. We perform the confidence interval calculations as a way of comparing the models to each other and to understand the precision of the fit parameters.

5.5 Ruling Out Experimental Artifacts

The distinct trends of $C_p(H)$ observed in the different compounds - namely, a field independence in Au, the peak feature in the HH samples, and the low-field decline in HH10 - were the first indications that systematic effects were not responsible for the field dependence of the heat capacity. To be certain that the $C_p(H)$ effect that we measured was not an experimental artifact, we ensured that the PPMS was properly calibrated and ran the experiment multiple times for different samples, as detailed below.

5.5.1 Calibration

For accurate temperature and heater power data, all components of the PPMS heat capacity holder were calibrated as a function of temperature and magnetic field, including the holder heater, the holder thermometer, and the sample stage thermometer. The two thermometers were calibrated based on the known temperature and magnetic field dependence of the system thermometer. With the calibrations in place, the errors in temperature and heater power are less than 2% [179, 180]. The same holder and calibration files were used for the addendum and sample heat capacity measurements.

As further calibration, we measured the addendum heat capacity of the blank holder with grease on the sample stage in a number of magnetic fields similar to those used for the sample measurement. The results are displayed in Figure 5.9(a). At 2 K, the heat capacity of the addendum changes at most by 3%. At higher temperatures, the addendum heat capacity values are mainly in-

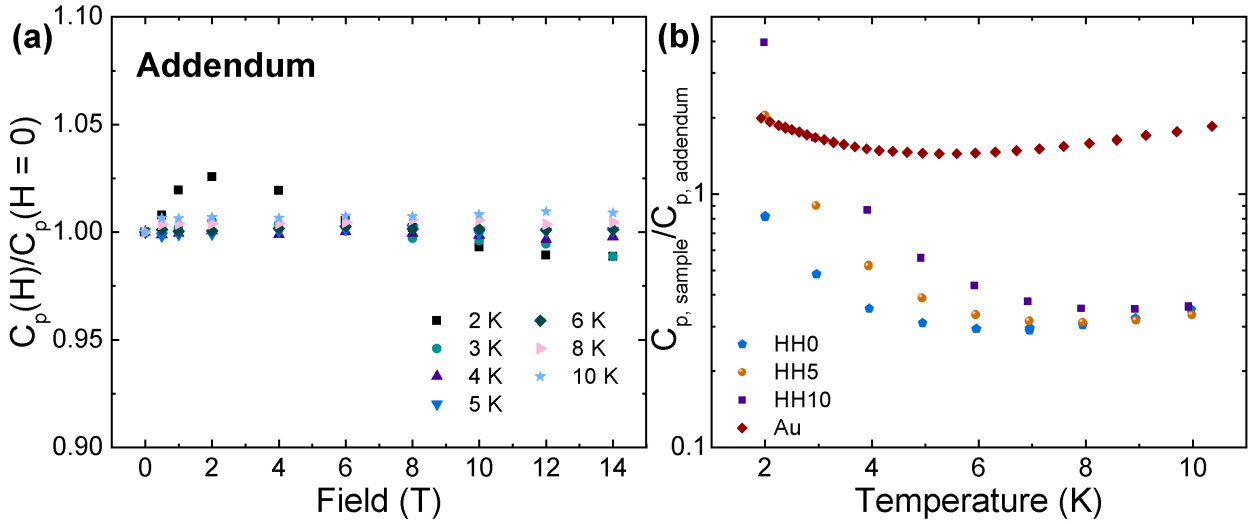

Figure 5.9: **Calibration and signal of the $Ti_{0.25}Zr_{0.25}Hf_{0.50}NiFe_xSn_{0.975}Sb_{0.025}$ samples and Au during the heat capacity measurement.** (a) Normalized addendum (blank sample holder) heat capacity as a function of magnetic field for temperatures from 2 to 10 K. (b) Ratio of zero-field sample heat capacity to addendum heat capacity for the four samples of the study from 2 to 10 K (b).

dependent of magnetic field. Thus, applying magnetic fields of 0 to 14 T during the heat capacity measurement has very little impact on the sample holder at temperatures between 2 and 10 K.

To ensure the accuracy of the sample measurement, the heat capacity of the sample must be of comparable magnitude with the addendum heat capacity. That way, the sample itself has a heat capacity signal that is discernible from the underlying sample holder. For example, regarding metallic compounds, $C_{p,sample}/C_{p,addendum} \approx 1/3$ results in heat capacity errors certainly less than 10% and usually less than 5% [179, 180]. We confirm the values of $C_{p,sample}/C_{p,addendum}$ in each of our measurements, as illustrated in Fig. 5.9(b). For the entire temperature range, all HH samples have heat capacities that are at least 30% of their respective addendum values, with even higher magnitudes of the ratio at lower temperature ($T < 4$ K). With a larger heat capacity and sample mass (28 mg vs. $\approx$ 14 mg for the HH samples), the Au sample has C_p values greater than its addendum over the entire temperature range. Overall, the above calibrations demonstrate that the background signal in the PPMS heat capacity measurement is small enough to rigorously determine the sample heat capacity as a function of temperature and magnetic field.

5.5.2 Reproducibility

In the final step in confirming that the magnetic field dependence of C_p for the HH samples is truly fundamental to the materials themselves, we performed the measurement multiple times for HH5 and HH10. The normalized sample heat capacity data as a function of magnetic field for

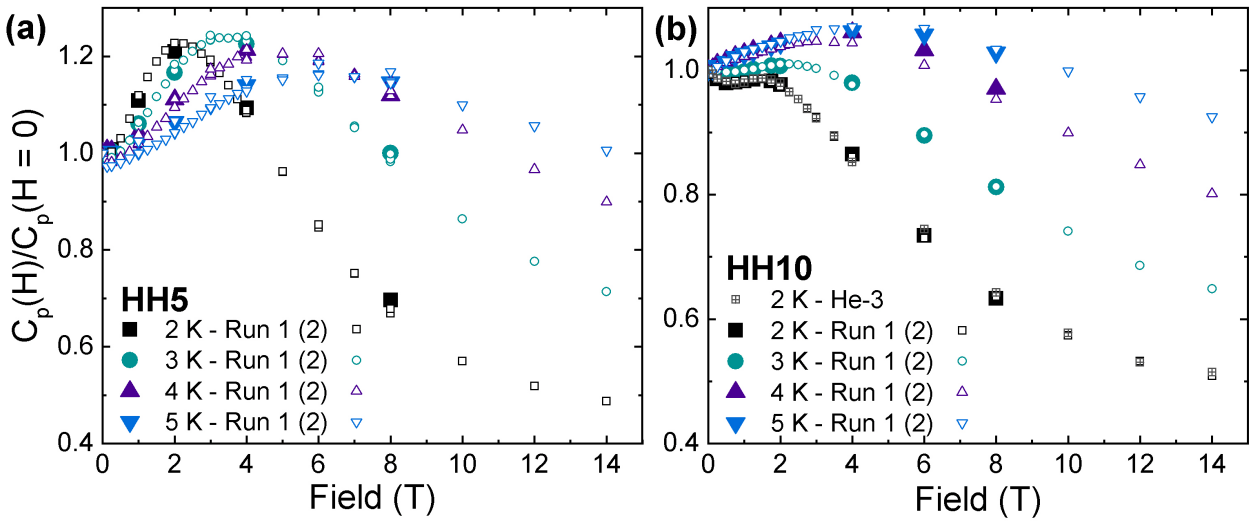

Figure 5.10: **Reproducibility of the heat capacity measurement for HH5 and HH10.** Two separate measurements of the normalized sample heat capacity as a function of magnetic field for temperatures from 2 to 5 K for (a) HH5 and (b) HH10. (b) also includes the $C_p(H)$ data at 2 K recorded using the He-3 setup with its distinct sample holder. The sample masses in the different runs were unique: 16.5 mg (Run 1) and 13.5 mg (Run 2) for HH5; and 19.5 mg (Run 1), 14 mg (Run 2), and 13 mg (He-3 setup) for HH10.

the distinct measurements are displayed in Figure 5.10. For each sample, a new addendum was measured with a fresh layer of grease on the sample stage. The samples from the previous run were cleaned, repolished, and weighed. The sample masses between Run 1 and Run 2 changed as follows: 16.5 mg (Run 1) and 13.5 mg (Run 2) for HH5, and 19.5 mg (Run 1) and 14 mg (Run 2) for HH10. Data from an entirely separate measurement using the He-3 PPMS option is also included in Fig. 5.10(b) for HH10. The He-3 setup uses a distinct sample holder with its own calibration, and the sample mass for that measurement was 13 mg. The data sets recorded during the separate measurements (Fig. 5.10) are nearly identical, adding to the robust nature of the magnetic field effect on C_p in these samples. Furthermore, because the effect is independent of mass, we are not concerned about any possible contribution from potential stage vibration in the high magnetic fields [179].

Last, our measured values of the zero-field heat capacity of gold are in agreement with previous studies. Specifically, at $T = 2$ K, we find $C_{p,Au}(H = 0, T = 2\text{ K}) = 24.4 \pm 0.9$ μJ g^{-1} K^{-1} compared to values of 24.7-25.2 μJ g^{-1} K^{-1} in Refs. [180, 181], and our $\gamma_{Au} = 3.4$ μJ g^{-1} K^{-2} matches that of Ref. [181]. The only heat capacity study we know of assessing $C_p(H)$ for Au does so for nanoscale colloids only at $H = 0.5$ T [182], so we cannot make any comparison regarding the behavior we recorded.

5.6 Conclusions

In this chapter, we have shown that the magnetic field-dependent heat capacity, $C_p(H,T)$, at low temperatures (2 to 10 K) is highly sensitive to the presence of paramagnetic centers in a number of magnetically different materials. High purity, diamagnetic gold displays a mainly constant heat capacity with applied magnetic field, whereas $Ti_{0.25}Zr_{0.25}Hf_{0.50}NiSn_{0.975}Sb_{0.025}$, a highly disordered paramagnetic composite, exhibits a $\gtrapprox$ 20% enhancement in $C_p(H)$ at 2 K under an applied field of 3 T. The peak is gradually suppressed with increasing temperature, essentially vanishing above 6 K. We rigorously showed that a two-level paramagnon contribution to the heat capacity can capture the field-dependent behavior. With added iron, the mictomagnetic $Ti_{0.25}Zr_{0.25}Hf_{0.50}NiFe_xSn_{0.975}Sb_{0.025}$ (x = 0.05 and 0.10) samples possess similar tendencies as the paramagnetic half-Heusler above 3 K. However, at lower temperatures, the confidence intervals of the paramagnon model fits to the experimental data become quite large for the mictomagnetic samples, suggesting a separate magnetic field-dependent contribution to $C_p(H,T)$. The intuitive magnon model that we derived to explain the additional effect in the partially ferromagnetic samples can mimic the heat capacity trend with one additional free parameter. However, the confidence intervals on the fit parameters indicate that the combined paramagnon+magnon model overfits the data. Separate measurements of the heat capacity of the x = 0.10 sample down to 0.36 K confirm our paramagnon analysis and the remaining low-field decline in $C_p(H)$ at the lowest temperatures. We qualitatively link the additional effect to a magnetotransport phenomenon we observed in a previous study, likely stemming from superconducting Sn-based binaries that could be present in the composites. Our work illuminates the advantage of studying the magnetic field dependence of C_p at set temperatures, compared to the less sensitive temperature-dependent studies at set fields, in order to witness the totality of underlying physical phenomena.

CHAPTER 6

Conclusions and Future Work

6.1 Summary

As a means of converting waste heat into usable electricity, thermoelectric materials should be an important facet of the global energy portfolio. To implement thermoelectric materials more broadly, I focused on two separate material systems: the superionic conductor, Cu_2Se, detailed in Chapter 3, and the half-Heusler composites, $Ti_{0.25}Zr_{0.25}Hf_{0.50}NiFe_xSn_{0.975}Sb_{0.025}$, described in Chapters 4 and 5.

Cu_2Se, a thermoelectric material with high conversion efficiency, unfortunately degrades in application conditions. In an effort to chemically stabilize the compound while maintaining its superior thermoelectric properties, I replaced small percentages of Cu with Sn and synthesized the series of samples $Cu_{2-2x}Sn_xSe$ (x = 0, 0.01, 0.02, and 0.05). By the thermoelectric transport measurements from room temperature to 873 K, the x = 0.01 sample possesses the largest zT values, averaging a 15% enhancement from 473 K to 823 K compared to the pure Cu_2Se. The augmented thermoelectric performance stems from a diminished thermal conductivity and a slightly improved power factor. Increased point defect scattering of phonons in the Cu_2Se matrix and the interaction of phonons with the sub-micron secondary phase of SnSe are the major contributing factors for the reduced thermal conductivity of $Cu_{1.98}Sn_{0.01}Se$. The larger hole mobility of $Cu_{1.98}Sn_{0.01}Se$ leads to the enhanced power factors compared to Cu_2Se.

To test the ability of the large tin ions to chemically stabilize the compounds, I modified electrical property measurement equipment to support a current stress test. During the experiments, each sample was held at 773 K with a $\Delta T \approx 50$ K while a current was driven through the material to emulate typical thermoelectric power generation conditions. The $Cu_{2-2x}Sn_xSe$ compounds with greater tin concentrations exhibited decreased material degradation, as measured by the density loss of the samples during the test. The Sn atoms within the matrix and as a secondary phase of SnSe act as electrical and physical barriers for the copper ion electromigration. However, even at the 5 at% Sn dopant level, solid copper was expelled and selenium-rich granules developed, which

eliminates the prospects for these compounds in long-term thermoelectric applications. Because there was a lack of current stress tests in the research on Cu_2Se, and superionic conductors in general, I emphasized that the electrical stability of the materials must be examined in thermoelectric operating conditions in order for the research to have significant meaning.

Following collaborative work demonstrating the ability of added Fe to enhance the thermoelectric performance of a half-Heusler composite, $Ti_{0.25}Zr_{0.25}Hf_{0.50}NiSn_{0.975}Sb_{0.025}$ (Ref. [98]), I sought to understand the magnetic properties of the $Ti_{0.25}Zr_{0.25}Hf_{0.50}NiFe_xSn_{0.975}Sb_{0.025}$ (x = 0, 0.02, 0.05, 0.075 and 0.10) series of samples ($T_C \approx 650$ K) at low temperatures (2 K to 300 K). The DC magnetization and AC susceptibility measurements of the Fe-added samples all point to a combination of superparamagnetism and cluster-glass behavior, the combination of which is called "mictomagnetism". The phenomena are most apparent in the x = 0.05 sample, which our previous work showed contains the greatest density of magnetic $TiNi_{4/3}Fe_{2/3}Sn$ nanoparticles [98]. The evidence for the spin freezing phenomena near 175 K lies in the magnetization hysteresis and the splitting of the zero-field-cooled and field-cooled temperature-dependent magnetic moments, as well as the frequency- and field-dependent maxima in the AC susceptibility. In the magnetotransport data, the Fe-added samples exhibit a Kondo minimum in the electrical resistivity near 25 K, which is consistent with the magnetic secondary phase in the non-magnetic matrix. The electrical resistivity below 4 K drops off sharply with temperature, an effect that can be explained by either weak-localization or superconducting Sn-based binaries. Research in magnetic thermoelectrics is a burgeoning pursuit, and the techniques and analyses demonstrated in Chapter 4 are important for understanding a variety of magnetic phenomena in thermoelectric materials.

In the same $Ti_{0.25}Zr_{0.25}Hf_{0.50}NiFe_xSn_{0.975}Sb_{0.025}$ composites, I observed a non-monotonic heat capacity dependence on the applied magnetic field at temperatures below 10 K. The paramagnetic x = 0 sample features a peak enhancement of the heat capacity of $\gtrapprox$ 20% at 2 K with an applied field of 3 T. At higher temperatures, the peak contracts and shifts to greater magnetic fields. In the mictomagnetic samples, the heat capacity behavior with magnetic field is quite similar to that of the paramagnetic sample, except for its augmented magnitudes and entirely unique trend at temperatures below 4 K. The measured $C_p(H)$ of diamagnetic gold was essentially constant, with the slight 2% increase at 2 K accounted for by the change of the addendum in magnetic field. The majority of the field dependence of the heat capacity can be explained by a two-level paramagnon model, an intuitive approach with reasonable confidence intervals when fit to the data. From the fit parameters, the concentration of paramagnetic centers aligns with either ionized impurities or defects at the grain boundaries of the composite materials. The paramagnon model fails to capture the lowest temperature field dependence of the heat capacity in the mictomagnetic samples. Namely, between 1.4 K and 3 K at low fields (up to 2 T), the heat capacity of the x = 0.10 sample is initially flat or declines to a slight minimum before following the paramagnon

trend. To explain the distinct dependence, I derived the magnon contribution to the heat capacity in field and with fourth-order dispersion terms, adding just one free parameter to the overall paramagnon+magnon model. Although the combined model fits the experimental data quite well, the confidence intervals in the fit parameters are larger than the mean values, and the overall confidence intervals cannot be calculated, both signs of overfitting. The lowest temperature measurements of $Ti_{0.25}Zr_{0.25}Hf_{0.50}NiFe_{0.10}Sn_{0.975}Sb_{0.025}$ down to 0.36 K confirm the paramagnon peak, but still do not allow for any reasonable fit by the paramagnon model. In the end, the separate contribution to the heat capacity in the mictomagnetic samples below 4 K could be associated with superconducting Sn-based binaries potentially present in the composites. Overall, the chapter highlights the insight of field-dependent heat capacity studies at fixed temperatures that cannot be as easily gleaned from the temperature-dependent heat capacity at fixed magnetic fields.

6.2 Future Work

With research being an ongoing, iterative process, it is important to provide some potential routes forward based on current findings. Regarding the promise of Cu_2Se and superionic conductors as stable thermoelectric materials, more recent results are highlighted in Section 3.6. Specifically, nanocomposites, segmentation, and a proper accounting for the critical voltage of electrodeposition are viable techniques for the eventual development of thermoelectric modules, and many of these efforts are ongoing worldwide. Considering the role of magnetic dopants in many classic thermoelectric materials, it is possible that high-T_C ferromagnetic nanoprecipitates within superionic conductors could interact with itinerant Cu ions and help to localize the electromigration up to a certain temperature. While improvements in zT are important, the main hurdle for superionic conductors to be used more broadly in thermoelectric technologies is the issue of stability. Measuring the time evolution of either the thermoelectric properties of a given material or the power output of a fabricated device in application conditions over the span of several weeks is therefore essential.

For the magnetic half-Heusler composites, the routes for high temperature thermoelectric performance enhancement could certainly include attempts with other magnetic dopants, such as the d-block Cr and Mn or the rare-earth elements. Other base compounds could be synthesized as the non-magnetic matrix similar to $Ti_{0.25}Zr_{0.25}Hf_{0.50}NiSn_{0.975}Sb_{0.025}$. Using the work of Galanakis [93], the magnetic strength of some of the full-Heusler compounds can be compared as a starting point for the intended magnetic composite phase. The size and concentration of the full-Heusler phases are critical in determining the magnetism of the composites and their overall thermoelectric properties. Therefore, the solubility of the magnetic dopant on the Ni site is a crucial parameter to consider in future synthesis. One possible way of understanding the potential for the largest impact

of the magnetism at high temperatures is to first screen the samples for the greatest magnetic frustration (seen from the separation of the zero-field-cooled and field-cooled DC magnetic moments) at low temperatures. With the desired materials in hand, it would be ideal to synthesize the individual magnetic full-Heusler compound within the composite as close to a single crystal as possible so that its fundamental low-temperature properties can be understood. New half-Heusler compounds are still being synthesized at various research centers globally, so many promising projects in this realm are possible.

The magnetic field-dependent heat capacity is intricately linked to the temperature-dependent magnetization by equilibrium thermodynamics, seen in the following expression:

$$C_{p,H}(H,T_0) = C_{p,H}(0,T_0) + T_0 \int_0^H \left.\frac{\partial^2 M(H,T)}{\partial T^2}\right|_{T=T_0} dH, \tag{6.1}$$

where the heat capacity and second derivative of the magnetization are evaluated at temperature T_0. Eqn. 6.1 relies on the definition of heat capacity that $C_{p,H} = T(\partial S/\partial T)_H$, where S is the total entropy of the system, as well as a magnetic Maxwell relation $\left(\frac{\partial S}{\partial H}\right)_T = \left(\frac{\partial M}{\partial T}\right)_H$. Experimental verification of Eq. 6.1 would be a demonstration that the Maxwell relation indeed holds. However, most magnetocaloric studies in the literature assume the Maxwell relation to be true in order to derive the corresponding change in entropy with applied magnetic field. Because heat capacity measurements are rarely performed at such fine increments of magnetic field, there are very few reports confirming the equality in Eq. 6.1 [183, 184, 185]. Coupling the data from Chapter 5 with the temperature-dependent magnetization would yield a comparison of the two sides of the equation. Care must be taken in evaluating the second derivative of the magnetization data since most numerical techniques introduce a lot of noise. Eq. 6.1 is independent of the type of magnetic system studied so it should hold in mictomagnetic composites, pure ferromagnets, etc.

Furthermore, the magnon model that I derived in Section 5.4.2 (with the final result in Eq. 5.15) depends on the spin stiffness, the volume of the sample, and the material's lattice parameters. If the only unknown variable is the spin stiffness, the magnetic field-dependent heat capacity could be used to extract the value in compounds where the magnon term is dominant. The value can then be compared with inelastic neutron scattering experiments that map the dispersion relation. Conversely, if the spin stiffness is known from neutron scattering data, $C_{p,ferro}$ can be calculated as a function of field and temperature by Eq. 5.15. Coupling the magnon contribution with that from electrons and phonons, the experimentally measured $C_{p,H}(H,T)$ can be compared with the calculation. While some efforts to perform such a study do exist [150], they are absent for most materials, including the elementary magnets Fe, Ni and Co. Perhaps the electronic term in these elements is highly dependent on magnetic field, obscuring the magnon contribution. Additional efforts in this area are certainly granted and appear straightforward.

BIBLIOGRAPHY

[1] "Estimated U.S. Energy Consumption in 2018," https://flowcharts.llnl.gov/commodities/energy, 2019, Accessed: 2020-03-14.

[2] Goldsmid, H. J., *Introduction to Thermoelectricity*, Vol. 121 of *Springer Series in Materials Science*, Springer-Verlag, Berlin Heidelberg, 2nd ed., 2016.

[3] Rowe, D., "Thermoelectrics, an environmentally-friendly source of electrical power," *Renew. Energy*, Vol. 16, No. 1, 1999, pp. 1251–1256.

[4] BCS, I., "Waste Heat Recovery: Technologies and Opportunities in U.S. Industry," Tech. rep., U.S. Department of Energy, 2008.

[5] Shakouri, A., "Recent Developments in Semiconductor Thermoelectric Physics and Materials," *Annu. Rev. Mater. Res.*, Vol. 41, No. 1, 2011, pp. 399–431.

[6] Zheng, X., Liu, C., Yan, Y., and Wang, Q., "A review of thermoelectrics research – Recent developments and potentials for sustainable and renewable energy applications," *Renew. Sustain. Energy Rev.*, Vol. 32, 2014, pp. 486–503.

[7] Tan, G., Zhao, L.-D., and Kanatzidis, M. G., "Rationally Designing High-Performance Bulk Thermoelectric Materials," *Chem. Rev.*, Vol. 116, No. 19, 2016, pp. 12123–12149.

[8] Han, C., Sun, Q., Li, Z., and Dou, S. X., "Thermoelectric Enhancement of Different Kinds of Metal Chalcogenides," *Adv. Energy Mater.*, Vol. 6, No. 15, 2016, pp. 1600498.

[9] Shi, X., Chen, L., and Uher, C., "Recent advances in high-performance bulk thermoelectric materials," *Int. Mater. Rev.*, Vol. 61, No. 6, 2016, pp. 379–415.

[10] He, J. and Tritt, T. M., "Advances in thermoelectric materials research: Looking back and moving forward," *Science*, Vol. 357, No. 6358, 2017.

[11] Chung, D.-Y., Hogan, T., Brazis, P., Rocci-Lane, M., Kannewurf, C., Bastea, M., Uher, C., and Kanatzidis, M. G., "$CsBi_4Te_6$: A High-Performance Thermoelectric Material for Low-Temperature Applications," *Science*, Vol. 287, No. 5455, 2000, pp. 1024–1027.

[12] Poudel, B., Hao, Q., Ma, Y., Lan, Y., Minnich, A., Yu, B., Yan, X., Wang, D., Muto, A., Vashaee, D., Chen, X., Liu, J., Dresselhaus, M. S., Chen, G., and Ren, Z., "High-Thermoelectric Performance of Nanostructured Bismuth Antimony Telluride Bulk Alloys," *Science*, Vol. 320, No. 5876, 2008, pp. 634–638.

[13] Zhao, H., Sui, J., Tang, Z., Lan, Y., Jie, Q., Kraemer, D., McEnaney, K., Guloy, A., Chen, G., and Ren, Z., "High thermoelectric performance of MgAgSb-based materials," *Nano Energy*, Vol. 7, 2014, pp. 97–103.

[14] Shutoh, N. and Sakurada, S., "Thermoelectric properties of the $Ti_x(Zr_{0.5}Hf_{0.5})_{1-x}NiSn$ half-Heusler compounds," *J. Alloys Compd.*, Vol. 389, No. 1, 2005, pp. 204–208.

[15] Rogl, G., Grytsiv, A., Rogl, P., Peranio, N., Bauer, E., Zehetbauer, M., and Eibl, O., "n-Type skutterudites $(R,Ba,Yb)_yCo_4Sb_{12}$ (R=Sr, La, Mm, DD, SrMm, SrDD) approaching $ZT \approx 2.0$," *Acta Mater.*, Vol. 63, 2014, pp. 30–43.

[16] Sui, J., Li, J., He, J., Pei, Y.-L., Berardan, D., Wu, H., Dragoe, N., Cai, W., and Zhao, L.-D., "Texturation boosts the thermoelectric performance of BiCuSeO oxyselenides," *Energy Environ. Sci.*, Vol. 6, 2013, pp. 2916–2920.

[17] Liu, H., Shi, X., Xu, F., Zhang, L., Zhang, W., Chen, L., Li, Q., Uher, C., Day, T., and Snyder, G. J., "Copper ion liquid-like thermoelectrics," *Nat. Mater.*, Vol. 11, No. 5, 2012, pp. 422–425.

[18] Basu, R., Bhattacharya, S., Bhatt, R., Roy, M., Ahmad, S., Singh, A., Navaneethan, M., Hayakawa, Y., Aswal, D. K., and Gupta, S. K., "Improved thermoelectric performance of hot pressed nanostructured n-type SiGe bulk alloys," *J. Mater. Chem. A*, Vol. 2, 2014, pp. 6922–6930.

[19] Tan, G., Shi, F., Hao, S., Zhao, L.-D., Chi, H., Zhang, X., Uher, C., Wolverton, C., Dravid, V. P., and Kanatzidis, M. G., "Non-equilibrium processing leads to record high thermoelectric figure of merit in PbTe–SrTe," *Nat. Commun.*, Vol. 7, 2016, pp. 12167.

[20] Zhao, L.-D., Lo, S.-H., Zhang, Y., Sun, H., Tan, G., Uher, C., Wolverton, C., Dravid, V. P., and Kanatzidis, M. G., "Ultralow thermal conductivity and high thermoelectric figure of merit in SnSe crystals," *Nature*, Vol. 508, 2014, pp. 373–377.

[21] Goldsmid, H. J., *Electronic Refrigeration*, Pion, London, 1986.

[22] Snyder, G. J. and Toberer, E. S., "Complex thermoelectric materials," *Nat. Mater.*, Vol. 7, 2008, pp. 105–114.

[23] Uher, C., editor, *Materials Aspect of Thermoelectricity*, CRC Press, 2016.

[24] Ashcroft, N. W. and Mermin, N. D., *Solid State Physics*, Brooks/Cole, CA, USA, 1st ed., 1976.

[25] "Hall (Magnetic) Sensors, LakeShore Cryotronics," https://www.lakeshore.com/products/categories/magnetic-products/hall-(magnetic)-sensors, 2019, Accessed: 2020-01-14.

[26] Ravich, I. U. I., Efimova, B. A., and Smirnov, I. A., *Semiconducting Lead Chalcogenides*, Plenum Press, New York, 1970.

[27] Day, T. W., Zeier, W. G., Brown, D. R., Melot, B. C., and Snyder, G. J., "Determining conductivity and mobility values of individual components in multiphase composite $Cu_{1.97}Ag_{0.03}Se$," *Appl. Phys. Lett.*, Vol. 105, No. 17, 2014, pp. 172103.

[28] Kittel, C., *Introduction to Solid State Physics*, John Wiley & Sons, New Delhi, 8th ed., 2005.

[29] Hurd, C. M., "Varieties of magnetic order in solids," *Contemp. Phys.*, Vol. 23, No. 5, 1982, pp. 469–493.

[30] Mydosh, J., *Spin Glasses: An Experimental Introduction*, Taylor & Francis, 1993.

[31] Arora, A., *Optical and electric field control of magnetism*, Ph.D. thesis, University of Potsdam, 2018.

[32] Ruderman, M. A. and Kittel, C., "Indirect Exchange Coupling of Nuclear Magnetic Moments by Conduction Electrons," *Phys. Rev.*, Vol. 96, Oct 1954, pp. 99–102.

[33] Kasuya, T., "A Theory of Metallic Ferro- and Antiferromagnetism on Zener's Model," *Prog. Theor. Phys.*, Vol. 16, No. 1, 1956, pp. 45–57.

[34] Yosida, K., "Magnetic Properties of Cu-Mn Alloys," *Phys. Rev.*, Vol. 106, 1957, pp. 893–898.

[35] Mermin, N. D. and Wagner, H., "Absence of Ferromagnetism or Antiferromagnetism in One- or Two-Dimensional Isotropic Heisenberg Models," *Phys. Rev. Lett.*, Vol. 17, 1966, pp. 1133–1136.

[36] Onsager, L., "Crystal Statistics. I. A Two-Dimensional Model with an Order-Disorder Transition," *Phys. Rev.*, Vol. 65, 1944, pp. 117–149.

[37] Gopal, E., *Specific Heats at Low Temperatures*, Plenum Press, New Delhi, 1966.

[38] Debye, P., "Zur Theorie der spezifischen Wärmen," *Ann. Phys. (Berl.)*, Vol. 344, No. 14, 1912, pp. 789–839.

[39] Putley, E. H., *The Hall Effect and Related Phenomena*, Vol. 4 of *Semi-Conductor Monographs*, Butterworths, London, 1960.

[40] Kaviany, M., *Heat Transfer Physics*, Cambridge, New York, 1st ed., 2008.

[41] He, Y., Day, T., Zhang, T., Liu, H., Shi, X., Chen, L., and Snyder, G. J., "High Thermoelectric Performance in Non-Toxic Earth-Abundant Copper Sulfide," *Adv. Mater.*, Vol. 26, No. 23, 2014, pp. 3974–3978.

[42] Boyce, J. and Huberman, B., "Superionic conductors: Transitions, structures, dynamics," *Phys. Rep.*, Vol. 51, No. 4, 1979, pp. 189–265.

[43] Trachenko, K., "Heat capacity of liquids: An approach from the solid phase," *Phys. Rev. B*, Vol. 78, 2008, pp. 104201.

[44] Yu, B., Liu, W., Chen, S., Wang, H., Wang, H., Chen, G., and Ren, Z., "Thermoelectric properties of copper selenide with ordered selenium layer and disordered copper layer," *Nano Energy*, Vol. 1, No. 3, 2012, pp. 472–478.

[45] Su, X., Fu, F., Yan, Y., Zheng, G., Liang, T., Zhang, Q., Cheng, X., Yang, D., Chi, H., Tang, X., Zhang, Q., and Uher, C., "Self-propagating high-temperature synthesis for compound thermoelectrics and new criterion for combustion processing," *Nat. Commun.*, Vol. 5, No. 1, 2014, pp. 4908–4914.

[46] Wu, L., Su, X., Yan, Y., Uher, C., and Tang, X., "Ultra-Fast One-Step Fabrication of Cu_2Se Thermoelectric Legs With Ni–Al Electrodes by Plasma-Activated Reactive Sintering Technique," *Adv. Eng. Mater.*, Vol. 18, No. 7, 2016, pp. 1181–1188.

[47] Li, D., Qin, X. Y., Liu, Y. F., Song, C. J., Wang, L., Zhang, J., Xin, H. X., Guo, G. L., Zou, T. H., Sun, G. L., Ren, B. J., and Zhu, X. G., "Chemical synthesis of nanostructured Cu_2Se with high thermoelectric performance," *RSC Adv.*, Vol. 4, 2014, pp. 8638–8644.

[48] Yang, L., Chen, Z.-G., Han, G., Hong, M., Zou, Y., and Zou, J., "High-performance thermoelectric Cu_2Se nanoplates through nanostructure engineering," *Nano Energy*, Vol. 16, 2015, pp. 367–374.

[49] Ballikaya, S., Chi, H., Salvador, J. R., and Uher, C., "Thermoelectric properties of Ag-doped Cu_2Se and Cu_2Te," *J. Mater. Chem. A*, Vol. 1, 2013, pp. 12478–12484.

[50] Day, T. W., Borup, K. A., Zhang, T., Drymiotis, F., Brown, D. R., Shi, X., Chen, L., Iversen, B. B., and Snyder, G. J., "High-temperature thermoelectric properties of $Cu_{1.97}Ag_{0.03}Se_{1+y}$," *Mater. Renew. Sustain. Energy*, Vol. 3, No. 2, 2014, pp. 26.

[51] Zhao, L., Wang, X., Yun, F. F., Wang, J., Cheng, Z., Dou, S., Wang, J., and Snyder, G. J., "The Effects of Te^{2-} and I^- Substitutions on the Electronic Structures, Thermoelectric Performance, and Hardness in Melt-Quenched Highly Dense $Cu_{2-x}Se$," *Adv. Electron. Mater.*, Vol. 1, No. 3, 2015, pp. 1400015.

[52] Day, T. W., Weldert, K. S., Zeier, W. G., Chen, B.-R., Moffitt, S. L., Weis, U., Jochum, K. P., Panthöfer, M., Bedzyk, M. J., Snyder, G. J., and Tremel, W., "Influence of Compensating Defect Formation on the Doping Efficiency and Thermoelectric Properties of $Cu_{2-y}Se_{1-x}Br_x$," *Chem. Mater.*, Vol. 27, No. 20, 2015, pp. 7018–7027.

[53] Tyagi, K., Gahtori, B., Bathula, S., Jayasimhadri, M., Singh, N. K., Sharma, S., Haranath, D., Srivastava, A., and Dhar, A., "Enhanced thermoelectric performance of spark plasma sintered copper-deficient nanostructured copper selenide," *J. Phys. Chem. Solids*, Vol. 81, 2015, pp. 100–105.

[54] Gahtori, B., Bathula, S., Tyagi, K., Jayasimhadri, M., Srivastava, A., Singh, S., Budhani, R., and Dhar, A., "Giant enhancement in thermoelectric performance of copper selenide by incorporation of different nanoscale dimensional defect features," *Nano Energy*, Vol. 13, 2015, pp. 36–46.

[55] Milat, O., Vučić, Z., and Ruščić, B., "Superstructural ordering in low-temperature phase of superionic Cu_2Se," *Solid State Ion.*, Vol. 23, No. 1, 1987, pp. 37–47.

[56] Kashida, S. and Akai, J., "X-ray diffraction and electron microscopy studies of the room-temperature structure of Cu_2Se," *J. Phys. C: Solid State Phys.*, Vol. 21, No. 31, 1988, pp. 5329–5336.

[57] Yamamoto, K. and Kashida, S., "X-ray study of the average structures of Cu_2Se and $Cu_{1.8}S$ in the room temperature and the high temperature phases," *J. Solid State Chem.*, Vol. 93, No. 1, 1991, pp. 202–211.

[58] Gulay, L., Daszkiewicz, M., Strok, O., and Pietraszko, A., "Crystal Structure of Cu_2Se," *Chemistry of Metals and Alloys*, Vol. 4, 2011, pp. 200–205.

[59] Chi, H., Kim, H., Thomas, J. C., Shi, G., Sun, K., Abeykoon, M., Bozin, E. S., Shi, X., Li, Q., Shi, X., Kioupakis, E., Van der Ven, A., Kaviany, M., and Uher, C., "Low-temperature structural and transport anomalies in Cu_2Se," *Phys. Rev. B*, Vol. 89, 2014, pp. 195209.

[60] Lu, P., Liu, H., Yuan, X., Xu, F., Shi, X., Zhao, K., Qiu, W., Zhang, W., and Chen, L., "Multiformity and fluctuation of Cu ordering in Cu_2Se thermoelectric materials," *J. Mater. Chem. A*, Vol. 3, 2015, pp. 6901–6908.

[61] Tonejc, A. and Tonejc, A., "X-ray diffraction study on $\alpha \leftrightarrow \beta$ phase transition of Cu_2Se," *J. Solid State Chem.*, Vol. 39, No. 2, 1981, pp. 259–261.

[62] Vučić, Z., Milat, O., Horvatić, V., and Ogorelec, Z., "Composition-induced phase-transition splitting in cuprous selenide," *Phys. Rev. B*, Vol. 24, 1981, pp. 5398–5401.

[63] Skomorokhov, A., Trots, D., Knapp, M., Bickulova, N., and Fuess, H., "Structural behaviour of $\beta-Cu_{2-\delta}Se$ ($\delta = 0$, 0.15, 0.25) in dependence on temperature studied by synchrotron powder diffraction," *J. Alloys Compd.*, Vol. 421, No. 1, 2006, pp. 64–71.

[64] Danilkin, S., Avdeev, M., Sakuma, T., Macquart, R., and Ling, C., "Neutron diffraction study of diffuse scattering in $Cu_{2-\delta}Se$ superionic compounds," *J. Alloys Compd.*, Vol. 509, No. 18, 2011, pp. 5460–5465.

[65] Sirusi, A. A., Ballikaya, S., Uher, C., and Ross, J. H., "Low-Temperature Structure and Dynamics in Cu_2Se," *J. Phys. Chem. C*, Vol. 119, No. 35, 2015, pp. 20293–20298.

[66] Kim, H., Ballikaya, S., Chi, H., Ahn, J.-P., Ahn, K., Uher, C., and Kaviany, M., "Ultralow thermal conductivity of β-Cu_2Se by atomic fluidity and structure distortion," *Acta Mater.*, Vol. 86, 2015, pp. 247–253.

[67] Miyatani, S.-Y. and Suzuki, Y., "On the Electric Conductivity of Cuprous Sulfide : Experiment," *J. Phys. Soc. Jpn.*, Vol. 8, No. 5, 1953, pp. 680–681.

[68] Wei, G., Keiser, J. R., Crouse, R. S., Allen, M. D., and Schaffhauser, A. C., "Post-test analysis of components from selenide isotope generator modules M-7, M-15, and M-18," Tech. rep., Oak Ridge National Laboratory, Tennessee, USA, 1979.

[69] Ema, Y., "Cu Electromigration Effect on $Cu_{2-x}Se$ Film Properties," *Jpn. J. Appl. Phys.*, Vol. 29, No. 10, 1990, pp. 2098–2102.

[70] Brown, D. R., Day, T., Caillat, T., and Snyder, G. J., "Chemical Stability of $(Ag,Cu)_2Se$: a Historical Overview," *J. Electr. Mater.*, Vol. 42, 2013, pp. 2014–2019.

[71] Dennler, G., Chmielowski, R., Jacob, S., Capet, F., Roussel, P., Zastrow, S., Nielsch, K., Opahle, I., and Madsen, G. K. H., "Are Binary Copper Sulfides/Selenides Really New and Promising Thermoelectric Materials?" *Adv. Energy Mater.*, Vol. 4, No. 9, 2014, pp. 1301581.

[72] Bailey, T. P. and Uher, C., "Potential for superionic conductors in thermoelectric applications," *Curr. Opin. Green Sustain. Chem.*, Vol. 4, 2017, pp. 58–63.

[73] Bailey, T. P., Hui, S., Xie, H., Olvera, A., Poudeu, P. F. P., Tang, X., and Uher, C., "Enhanced ZT and attempts to chemically stabilize Cu_2Se via Sn doping," *J. Mater. Chem. A*, Vol. 4, 2016, pp. 17225–17235.

[74] Qiu, P., Zhang, T., Qiu, Y., Shi, X., and Chen, L., "Sulfide bornite thermoelectric material: a natural mineral with ultralow thermal conductivity," *Energy Environ. Sci.*, Vol. 7, 2014, pp. 4000–4006.

[75] Rowe, D. M., editor, *CRC Handbook of Thermoelectrics*, CRC Press, 1995.

[76] Rivet, J., Laruelle, P., Flahaut, J., and Fichet, R., "Diagrammes de phases de systèmes SnSe-Cu_2Se et $SnSe_2$-Cu_2Se," *Bull. Soc. Chim. Fr.*, Vol. 5, 1970, pp. 1667–1670.

[77] Shannon, R. D. and Prewitt, C. T., "Effective ionic radii in oxides and fluorides," *Acta Crystallogr. Sect. B*, Vol. 25, No. 5, 1969, pp. 925–946.

[78] Shannon, R. D., "Revised effective ionic radii and systematic studies of interatomic distances in halides and chalcogenides," *Acta Crystallogr. Sect. A*, Vol. 32, No. 5, 1976, pp. 751–767.

[79] Liu, F., Huang, M., Gong, Z., Ao, W., Li, Y., and Li, J., "Enhancing the thermoelectric performance of β-Cu_2Se by incorporating SnSe," *J. Alloys Compd.*, Vol. 651, 2015, pp. 648–654.

[80] Singh, N. K., Bathula, S., Gahtori, B., Tyagi, K., Haranath, D., and Dhar, A., "The effect of doping on thermoelectric performance of p-type SnSe: Promising thermoelectric material," *J. Alloys Compd.*, Vol. 668, 2016, pp. 152–158.

[81] Hirahara, E., "The Electrical Conductivity and Isothermal Hall Effect in Cuprous Sulfide, Semi-Conductor," *J. Phys. Soc. Jpn.*, Vol. 6, No. 6, 1951, pp. 428–437.

[82] Dudkin, L. D. and Abrikosov, N. K., "The effect of nickel on the properties of the semiconducting compound $CoSb_3$," *Zhurnal Neorganicheskoi Khimii*, Vol. 2, 1957, pp. 212–221.

[83] Sassi, S., Candolfi, C., Vaney, J.-B., Ohorodniichuk, V., Masschelein, P., Dauscher, A., and Lenoir, B., "Assessment of the thermoelectric performance of polycrystalline p-type SnSe," *Appl. Phys. Lett.*, Vol. 104, No. 21, 2014, pp. 212105.

[84] Alekseev, P. A., "High borides: determining the features and details of lattice dynamics from neutron spectroscopy," *Physics-Uspekhi*, Vol. 58, 2015, pp. 330–344.

[85] Mills, K. C., *Thermodynamic data for inorganic sulphides, selenides and tellurides*, Butterworths, 1974.

[86] Barbier, T., Lemoine, P., Gascoin, S., Lebedev, O. I., Kaltzoglou, A., Vaqueiro, P., Powell, A. V., Smith, R. I., and Guilmeau, E., "Structural stability of the synthetic thermoelectric ternary and nickel-substituted tetrahedrite phases," *J. Alloys Compd.*, Vol. 634, 2015, pp. 253–262.

[87] Bhattacharya, S., Bohra, A., Basu, R., Bhatt, R., Ahmad, S., Meshram, K. N., Debnath, A. K., Singh, A., Sarkar, S. K., Navneethan, M., Hayakawa, Y., Aswal, D. K., and Gupta, S. K., "High thermoelectric performance of $(AgCrSe_2)_{0.5}(CuCrSe_2)_{0.5}$ nano-composites having all-scale natural hierarchical architectures," *J. Mater. Chem. A*, Vol. 2, 2014, pp. 17122–17129.

[88] Olvera, A. A., Moroz, N. A., Sahoo, P., Ren, P., Bailey, T. P., Page, A. A., Uher, C., and Poudeu, P. F. P., "Partial indium solubility induces chemical stability and colossal thermoelectric figure of merit in Cu_2Se," *Energy Environ. Sci.*, Vol. 10, 2017, pp. 1668–1676.

[89] Qiu, P., Agne, M. T., Liu, Y., Zhu, Y., Chen, H., Mao, T., Yang, J., Zhang, W., Haile, S. M., Zeier, W. G., Janek, J., Uher, C., Shi, X., Chen, L., and Snyder, G. J., "Suppression of atom motion and metal deposition in mixed ionic electronic conductors," *Nat. Commun.*, Vol. 9, 2018, pp. 2910–2917.

[90] Qiu, P., Mao, T., Huang, Z., Xia, X., Liao, J., Agne, M. T., Gu, M., Zhang, Q., Ren, D., Bai, S., Shi, X., Snyder, G. J., and Chen, L., "High-Efficiency and Stable Thermoelectric Module Based on Liquid-Like Materials," *Joule*, Vol. 3, No. 6, 2019, pp. 1538–1548.

[91] Graf, T., Felser, C., and Parkin, S. S. P., "Simple rules for the understanding of Heusler compounds," *Prog. Solid State Ch.*, Vol. 39, 2011, pp. 1–50.

[92] Wollmann, L., Nayak, A. K., Parkin, S. S. P., and Felser, C., "Heusler 4.0: Tunable Materials," *Annu. Rev. Mater. Res.*, Vol. 47, 2017, pp. 247–270.

[93] Galanakis, I., "Theory of Heusler and Full-Heusler Compounds," *Heusler Alloys: Properties, Growth, Applications*, edited by C. Felser and A. Hirohata, No. 222 in Springer Series in Materials Science, chap. 1, Springer International Publishing, Switzerland, 2016, pp. 3–36.

[94] Palmstrøm, C. J., "Heusler compounds and spintronics," *Prog. Cryst. Growth Ch.*, Vol. 62, 2016, pp. 371–397.

[95] Fecher, G. H., Rausch, E., Balke, B., Weidenkaff, A., and Felser, C., "Half-Heusler materials as model systems for phase-separated thermoelectrics," *Phys. Status Solidi A*, Vol. 213, 2016, pp. 716–731.

[96] Yu, J., Xia, K., Zhao, X., and Zhu, T., "High performance p-type half-Heusler thermoelectric materials," *J. Phys. D Appl. Phys.*, Vol. 51, 2018, pp. 113001–113015.

[97] LeBlanc, S., "Thermoelectric generators: Linking material properties and systems engineering for waste heat recovery applications," *Sustain. Mater. Tech.*, Vol. 1-2, 2014, pp. 26–35.

[98] Lu, R., Lopez, J. S., Liu, Y., Bailey, T. P., Page, A. A., Wang, S., Uher, C., and Poudeu, P. F. P., "Coherent magnetic nanoinclusions induce charge localization in half−Heusler alloys leading to high−T_C ferromagnetism and enhanced thermoelectric performance," *J. Mater. Chem. A*, Vol. 7, 2019, pp. 11095–11103.

[99] Uher, C., Yang, J., Hu, S., Morelli, D. T., and Meisner, G. P., "Transport properties of pure and doped MNiSn (M=Zr, Hf)," *Phys. Rev. B*, Vol. 59, Apr 1999, pp. 8615–8621.

[100] Populoh, S., Aguirre, M. H., Brunko, O. C., Galazka, K., Lu, Y., and Weidenkaff, A., "High figure of merit in (Ti,Zr,Hf)NiSn half-Heusler alloys," *Scripta. Mater.*, Vol. 66, 2012, pp. 1073–1076.

[101] Schwall, M. and Balke, B., "Phase separation as a key to a thermoelectric high efficiency," *Phys. Chem. Chem. Phys.*, Vol. 15, 2013, pp. 1868–1872.

[102] Downie, R. A., MacLaren, D. A., and Bos, J.-W. G., "Thermoelectric performance of multiphase XNiSn (X = Ti, Zr, Hf) half-Heusler alloys," *J. Mater. Chem. A*, Vol. 2, 2014, pp. 6107–6114.

[103] Geng, H. and Zhang, H., "Effects of phase separation on the thermoelectric properties of (Ti, Zr, Hf)NiSn half-Heusler alloys," *J. Appl. Phys.*, Vol. 116, 2014, pp. 033708.

[104] Downie, R. A., Barczak, S. A., Smith, R. I., and Bos, J. W. G., "Compositions and thermoelectric properties of XNiSn (X = Ti, Zr, Hf) half-Heusler alloys," *J. Mater. Chem. C*, Vol. 3, 2015, pp. 10534–10542.

[105] Makongo, J. P. A., Misra, D. K., Zhou, X., Pant, A., Shabetai, M. R., Su, X., Uher, C., Stokes, K. L., and Poudeu, P. F. P., "Simultaneous Large Enhancements in Thermopower and Electrical Conductivity of Bulk Nanostructured Half-Heusler Alloys," *J. Am. Chem. Soc.*, Vol. 133, 2011, pp. 18843–18852.

[106] Liu, Y., Sahoo, P., Makongo, J. P. A., Zhou, X., Kim, S.-J., Chi, H., Uher, C., Pan, X., and Poudeu, P. F. P., "Large Enhancements of Thermopower and Carrier Mobility in Quantum Dot Engineered Bulk Semiconductors," *J. Am. Chem. Soc.*, Vol. 135, 2013, pp. 7486–7495.

[107] Chi, H., Tan, G., Kanatzidis, M. G., Li, Q., and Uher, C., "A low-temperature study of manganese-induced ferromagnetism and valence band convergence in tin telluride," *Appl. Phys. Lett.*, Vol. 108, No. 18, 2016, pp. 182101.

[108] Gorai, P., Toberer, E. S., and Stevanović, V., "Thermoelectricity in transition metal compounds: the role of spin disorder," *Phys. Chem. Chem. Phys.*, Vol. 18, 2016, pp. 31777–31786.

[109] Zhao, W., Liu, Z., Wei, P., Zhang, Q., Zhu, W., Su, X., Tang, X., Yang, J., Liu, Y., Shi, J., Chao, Y., Lin, S., and Pei, Y., "Magnetoelectric interaction and transport behaviours in magnetic nanocomposite thermoelectric materials," *Nat. Nanotechnol.*, Vol. 12, 2016, pp. 55–60.

[110] Ahmed, F., Tsujii, N., and Mori, T., "Thermoelectric properties of $CuGa_{1-x}Mn_xTe_2$: power factor enhancement by incorporation of magnetic ions," *J. Mater. Chem. A*, Vol. 5, 2017, pp. 7545–7554.

[111] Acharya, S., Anwar, S., Mori, T., and Soni, A., "Coupling of charge carriers with magnetic entropy for power factor enhancement in Mn doped $Sn_{1.03}Te$ for thermoelectric applications," *J. Mater. Chem. C*, Vol. 6, 2018, pp. 6489–6493.

[112] Tsujii, N., Nishide, A., Hayakawa, J., and Mori, T., "Observation of enhanced thermopower due to spin fluctuation in weak itinerant ferromagnet," *Sci. Adv.*, Vol. 5, No. 2, 2019.

[113] Li, C., Ma, S., Wei, P., Zhu, W., Nie, X., Sang, X., Sun, Z., Zhang, Q., and Zhao, W., "Magnetism-induced huge enhancement of the room-temperature thermoelectric and cooling performance of p-type BiSbTe alloys," *Energy Environ. Sci.*, Vol. 13, 2020, pp. 535–544.

[114] Beck, P. A., "Properties of mictomagnets (spinglasses)," *Prog. Mater. Sci.*, Vol. 23, 1980, pp. 1–49.

[115] Li, D. X., Nimori, S., Shiokawa, Y., Haga, Y., Yamamoto, E., and Onuki, Y., "Ferromagnetic cluster glass behavior in U_2IrSi_3," *Phys. Rev. B*, Vol. 68, 2003, pp. 172405.

[116] Balanda, M., "AC Susceptibility Studies of Phase Transitions and Magnetic Relaxation: Conventional, Molecular and Low-Dimensional Magnets," *Acta Phys. Pol. A*, Vol. 124, 2013, pp. 964–976.

[117] Upadhyay, S. K., Iyer, K. K., and Sampathkumaran, E. V., "Magnetic behavior of metallic kagome lattices, $Tb_3Ru_4Al_{12}$ and $Er_3Ru_4Al_{12}$," *J. Phys. Condens. Mat.*, Vol. 29, 2017, pp. 325601–325610.

[118] Ahilan, K., Bennett, M. C., Aronson, M. C., Anderson, N. E., Canfield, P. C., Munoz-Sandoval, E., Gortenmulder, T., Hendrikx, R., and Mydosh, J. A., "Magnetotransport in single-crystal half-Heusler compounds," *Phys. Rev. B*, Vol. 69, 2004, pp. 245116.

[119] Ślebarski, A., Maple, M. B., Wrona, A., and Winiarska, A., "Kondo-type behavior in $Fe_{2-x}M_xTiSn$(M = Co,Ni)," *Phys. Rev. B*, Vol. 63, 2001, pp. 214416.

[120] Aharoni, A., "Relaxation Time of Superparamagnetic Particles with Cubic Anisotropy," *Phys. Rev. B*, Vol. 7, 1973, pp. 1103–1107.

[121] Ferrari, E. F., da Silva, F. C. S., and Knobel, M., "Influence of the distribution of magnetic moments on the magnetization and magnetoresistance in granular alloys," *Phys. Rev. B*, Vol. 56, 1997, pp. 6086–6093.

[122] Fonseca, F. C., Goya, G. F., Jardim, R. F., Muccillo, R., Carreño, N. L. V., Longo, E., and Leite, E. R., "Superparamagnetism and magnetic properties of Ni nanoparticles embedded in SiO_2," *Phys. Rev. B*, Vol. 66, 2002, pp. 104406.

[123] Allia, P., Knobel, M., Tiberto, P., and Vinai, F., "Magnetic properties and giant magnetoresistance of melt-spun granular $Cu_{100-x} - Co_x$ alloys," *Phys. Rev. B*, Vol. 52, 1995, pp. 15398–15411.

[124] Knobel, M., Nunes, W. C., Socolovsky, L. M., De Biasi, E., Vargas, J. M., and Denardin, J. C., "Superparamagnetism and Other Magnetic Features in Granular Materials: A Review on Ideal and Real Systems," *J. Nanosci. Nanotechno.*, Vol. 8, No. 6, 2008, pp. 2836–2857.

[125] Haldar, A., Suresh, K. G., and Nigam, A. K., "Observation of re-entrant spin glass behavior in $(Ce_{1-x}Er_x)Fe_2$ compounds," *Europhys. Lett.*, Vol. 91, No. 6, 2010, pp. 67006.

[126] Levin, E. M., Pecharsky, V. K., and Gschneidner, K. A., "Real and imaginary components of the alternating current magnetic susceptibility of RAl_2 (R=Gd, Dy, and Er) in the ferromagnetic region," *J. Appl. Phys.*, Vol. 90, No. 12, 2001, pp. 6255–6262.

[127] Dormann, J. L., Bessais, L., and Fiorani, D., "A dynamic study of small interacting particles: superparamagnetic model and spin-glass laws," *J. Phys. C Solid State*, Vol. 21, No. 10, 1988, pp. 2015–2034.

[128] Casimir, H. and du Pré, F., "Note on the thermodynamic interpretation of paramagnetic relaxation phenomena," *Physica*, Vol. 5, No. 6, 1938, pp. 507–511.

[129] Aliev, F. G., Kozyrkov, V. V., Moshchalkov, V. V., Scolozdra, R. V., and Durczewski, K., "Narrow band in the intermetallic compounds MNiSn (M=Ti, Zr, Hf)," *Z. Phys. B Con. Mat.*, Vol. 80, No. 3, 1990, pp. 353–357.

[130] Kondo, J., "Resistance Minimum in Dilute Magnetic Alloys," *Prog. Theor. Phys.*, Vol. 32, No. 1, 1964, pp. 37–49.

[131] Hamann, D. R., "New Solution for Exchange Scattering in Dilute Alloys," *Phys. Rev.*, Vol. 158, 1967, pp. 570–580.

[132] He, H. T., Yang, C. L., Ge, W. K., Wang, J. N., Dai, X., and Wang, Y. Q., "Resistivity minima and Kondo effect in ferromagnetic GaMnAs films," *Appl. Phys. Lett.*, Vol. 87, No. 16, 2005, pp. 162506.

[133] Hasegawa, R. and Tsuei, C. C., "Kondo Effect in Amorphous Fe-Pd-Si and Co-Pd-Si Alloys," *Phys. Rev. B*, Vol. 3, 1971, pp. 214–219.

[134] Lee, P. A. and Ramakrishnan, T. V., "Disordered electronic systems," *Rev. Mod. Phys.*, Vol. 57, 1985, pp. 287–337.

[135] Webb, G., Marsiglio, F., and Hirsch, J., "Superconductivity in the elements, alloys and simple compounds," *Physica C*, Vol. 514, 2015, pp. 17–27.

[136] Yosida, K., "Anomalous Electrical Resistivity and Magnetoresistance Due to an s-d Interaction in Cu-Mn Alloys," *Phys. Rev.*, Vol. 107, 1957, pp. 396–403.

[137] Toyozawa, Y., "Theory of Localized Spins and Negative Magnetoresistance in the Metallic Impurity Conduction," *J. Phys. Soc. Jpn.*, Vol. 17, No. 6, 1962, pp. 986–1004.

[138] Khosla, R. P. and Fischer, J. R., "Magnetoresistance in Degenerate CdS: Localized Magnetic Moments," *Phys. Rev. B*, Vol. 2, 1970, pp. 4084–4097.

[139] Giauque, W. F., Lyon, D. N., Hornung, E. W., and Hopkins, T. E., "Calorimetric Determination of Isothermal Entropy Changes in High Magnetic Fields at Low Temperatures. $CoSO_4 \cdot 7H_2O$," *J. Chem. Phys.*, Vol. 37, No. 7, 1962, pp. 1446–1452.

[140] Pecharsky, V. K. and Gschneidner, Jr., K. A., "Giant Magnetocaloric Effect in $Gd_5(Si_2Ge_2)$," *Phys. Rev. Lett.*, Vol. 78, Jun 1997, pp. 4494–4497.

[141] Franco, V., Blázquez, J., Ipus, J., Law, J., Moreno-Ramírez, L., and Conde, A., "Magnetocaloric effect: From materials research to refrigeration devices," *Prog. Mater. Sci.*, Vol. 93, 2018, pp. 112–232.

[142] Sessoli, R., Gatteschi, D., Caneschi, A., and Novak, M. A., "Magnetic bistability in a metal-ion cluster," *Nature*, Vol. 365, 1993, pp. 141–143.

[143] Gaita-Ariño, A., Luis, F., Hill, S., and Coronado, E., "Molecular spins for quantum computation," *Nat. Chem.*, Vol. 11, 2019, pp. 301–309.

[144] Uchida, K., Takahashi, S., Harii, K., Ieda, J., Koshibae, W., Ando, K., Maekawa, S., and Saitoh, E., "Observation of the spin Seebeck effect," *Nature*, Vol. 455, 2008, pp. 778–781.

[145] Bauer, G. E. W., Saitoh, E., and van Wees, B. J., "Spin caloritronics," *Nat. Mater.*, Vol. 11, 2012, pp. 391–399.

[146] Heisenberg, W., "Zur Theorie des Ferromagnetismus," *Z. Phys.*, Vol. 49, 1928, pp. 619–636.

[147] Kittel, C., *Quantum Theory of Solids*, John Wiley and Sons, New York, 2nd ed., 1987.

[148] Imada, M., Fujimori, A., and Tokura, Y., "Metal-insulator transitions," *Rev. Mod. Phys.*, Vol. 70, 1998, pp. 1039–1263.

[149] Wohlfarth, E., "Thermodynamic aspects of itinerant electron magnetism," *Physica B+C*, Vol. 91, 1977, pp. 305–314.

[150] Roy, M., Mitchell, J., Potashnik, S., and Schiffer, P., "Field dependent specific-heat of rare earth manganites," *J. Magn. Magn. Mater.*, Vol. 218, No. 2, 2000, pp. 191–197.

[151] Onose, Y., Ideue, T., Katsura, H., Shiomi, Y., Nagaosa, N., and Tokura, Y., "Observation of the Magnon Hall Effect," *Science*, Vol. 329, No. 5989, 2010, pp. 297–299.

[152] Riggs, S. C., Vafek, O., Kemper, J. B., Betts, J. B., Migliori, A., Balakirev, F. F., Hardy, W. N., Liang, R., Bonn, D. A., and Boebinger, G. S., "Heat capacity through the magnetic-field-induced resistive transition in an underdoped high-temperature superconductor," *Nat. Phys.*, Vol. 7, 2011, pp. 332–335.

[153] Ikeda, K. and Gschneider, K., "Disappearance of the heat capacity peak of Sc_3In around the curie temperature in high magnetic fields," *J. Magn. Magn. Mater.*, Vol. 22, No. 3, 1981, pp. 207–211.

[154] Tien, C., Lu, J. J., and Jang, L. Y., "Random magnetic moments and spin-glass-like behaviors in the heavy-fermion compound $CeNi_2Sn_2$," *Phys. Rev. B*, Vol. 65, 2002, pp. 214416.

[155] Phelan, W. A., Koohpayeh, S. M., Cottingham, P., Freeland, J. W., Leiner, J. C., Broholm, C. L., and McQueen, T. M., "Correlation between Bulk Thermodynamic Measurements and the Low-Temperature-Resistance Plateau in SmB_6," *Phys. Rev. X*, Vol. 4, 2014, pp. 031012.

[156] Yadam, S., Singh, D., Venkateshwarlu, D., Gangrade, M. K., Samatham, S. S., and Ganesan, V., "Magneto-heat capacity study on Kondo lattice system $Ce(Ni_{1-x}Cu_x)_2Al_3$," *Bull. Mater. Sci.*, Vol. 39, No. 2, 2016, pp. 537–541.

[157] Mishra, A. K., Krishnan, M., Singh, D., Samatham, S. S., Gangrade, M., Venkatesh, R., and Ganesan, V., "Spin fluctuations in Cr doped MnSi," *J. Magn. Magn. Mater.*, Vol. 448, 2018, pp. 130–134.

[158] Kneidinger, F., Zeiringer, I., Siderenko, A., Bauer, E., Michor, H., Rogl, P., and Sereni, J. G., "Physical properties of CeIrSi with trillium-lattice frustrated magnetism," *Phys. Rev. B*, Vol. 100, 2019, pp. 134442.

[159] Bailey, T. P., Lu, R., Poudeu, P., and Uher, C., "Mictomagnetic full-Heusler nanoprecipitates in (Ti, Zr, Hf)NiFexSn half-Heusler composites," *Mater. Today Phys.*, Vol. 11, 2019, pp. 100155.

[160] Kim, S., Fisher, R., Phillips, N., and Gordon, J., "Specific heat of high-T_c $YBa_2(Cu_{3-x}M_x)O_7$ with M=Cr or Zn," *Physica C*, Vol. 162-164, 1989, pp. 494–495.

[161] Loram, J., Mirza, K., and Freeman, P., "The electronic specific heat of $YBa_2(Cu_{1-x}Zn_x)_3O_7$ from 1.6 K to 300 K," *Physica C*, Vol. 171, No. 3, 1990, pp. 243–256.

[162] Roduner, E., "Superatom chemistry: promising properties of near-spherical noble metal clusters," *Phys. Chem. Chem. Phys.*, Vol. 20, 2018, pp. 23812–23826.

[163] Falge, R. L. and Wolcott, N. M., "Cluster specific heats in copper-rich Cu-Ni alloys: The effect of iron," *J. Low Temp. Phys.*, Vol. 5, No. 6, 1971, pp. 617–650.

[164] Kamimura, H. and Yamaguchi, E., "Electron correlation effects on Anderson localized states," *Solid State Commun.*, Vol. 28, No. 1, 1978, pp. 127–131.

[165] Kobayashi, N., Ikehata, S., Kobayashi, S., and Sasaki, W., "Magnetic field dependence of the specific heat of heavily phosphorus doped silicon," *Solid State Commun.*, Vol. 32, No. 11, 1979, pp. 1147–1150.

[166] Li, W.-H., Yang, C. C., Tsao, F. C., Wu, S. Y., Huang, P. J., Chung, M. K., and Yao, Y. D., "Enhancement of superconductivity by the small size effect in In nanoparticles," *Phys. Rev. B*, Vol. 72, 2005, pp. 214516.

[167] Zhang, Y., Wong, C. H., Shen, J., Sze, S. T., Zhang, B., Zhang, H., Dong, Y., Xu, H., Yan, Z., Li, Y., Hu, X., and Lortz, R., "Dramatic enhancement of superconductivity in single-crystalline nanowire arrays of Sn," *Sci. Rep.*, Vol. 6, 2016, pp. 32963.

[168] Khlopkin, M. N., "The specific heat of Nb_3Sn in magnetic fields up to 19 T," *J. Exp. Theor. Phys.*, Vol. 63, 1986, pp. 164–168.

[169] Wang, Y., Plackowski, T., and Junod, A., "Specific heat in the superconducting and normal state (2–300 K, 0–16 T), and magnetic susceptibility of the 38 K superconductor MgB_2: evidence for a multicomponent gap," *Physica C*, Vol. 355, No. 3, 2001, pp. 179–193.

[170] Ikeda, K., Gschneidner, K., Tsang, T.-W., and Schmidt, F., "Quenching of spin fluctuations in scandium," *Solid State Commun.*, Vol. 41, No. 12, 1982, pp. 889–892.

[171] Jin, H., Restrepo, O. D., Antolin, N., Boona, S. R., Windl, W., Myers, R. C., and Heremans, J. P., "Phonon-induced diamagnetic force and its effect on the lattice thermal conductivity," *Nat. Mater.*, Vol. 14, 2015, pp. 601–606.

[172] Chouteau, G., Fourneaux, R., Tournier, R., and Lederer, P., "Specific Heat of Nearly Magnetic Centers in Pd:Ni Alloys," *Phys. Rev. Lett.*, Vol. 21, 1968, pp. 1082–1085.

[173] Takeuchi, J. and Masuda, Y., "Low Temperature Specific Heat of Itinerant Electron Ferromagnet Sc_3In," *J. Phys. Soc. Jpn.*, Vol. 46, No. 2, 1979, pp. 468–474.

[174] Keffer, F., *Spin Waves*, Springer Berlin Heidelberg, Berlin, Heidelberg, 1966, pp. 1–273.

[175] Kouvel, J. and Brooks, H., "Some Spin Wave Properties of Ferrimagnetic and Antiferromagnetic Simple Cubic Crystals," Tech. Rep. 198, Harvard University, Massachusetts, USA, 1954.

[176] Collins, M. F., Minkiewicz, V. J., Nathans, R., Passell, L., and Shirane, G., "Critical and Spin-Wave Scattering of Neutrons from Iron," *Phys. Rev.*, Vol. 179, 1969, pp. 417–430.

[177] Levin, I., "NIST Inorganic Crystal Structure Database (ICSD)," https://doi.org/10.18434/M32147, 2018, Accessed: 2019-03-18.

[178] Levin, K. and Mills, D. L., "Contribution of giant spin clusters to the resistivity, neutron-scattering cross section, and specific heat in alloys: Application to Ni-Cu," *Phys. Rev. B*, Vol. 9, 1974, pp. 2354–2371.

[179] Quantum Design, *Physical Property Measurement System: Heat Capacity Option User's Manual*.

[180] Lashley, J., Hundley, M., Migliori, A., Sarrao, J., Pagliuso, P., Darling, T., Jaime, M., Cooley, J., Hults, W., Morales, L., Thoma, D., Smith, J., Boerio-Goates, J., Woodfield, B., Stewart, G., Fisher, R., and Phillips, N., "Critical examination of heat capacity measurements made on a Quantum Design physical property measurement system," *Cryogenics*, Vol. 43, No. 6, 2003, pp. 369–378.

[181] Boerstoel, B., Zwart, J., and Hansen, J., "The specific heat of palladium, platinum, gold and copper below 30 K," *Physica*, Vol. 54, No. 3, 1971, pp. 442–458.

[182] Goll, G. and Lohneysen, H., "Specific heat of nanocrystalline and colloidal noble metals at low temperatures," *Nanostruct. Mater.*, Vol. 6, No. 5, 1995, pp. 559–562, Proceedings of the Second International Conference on Nanostructured Materials.

[183] Pecharsky, V. K. and Gschneidner, K. A., *Comparison of the Magnetocaloric Effect Derived from Heat Capacity, Direct, and Magnetization Measurements*, Springer US, Boston, MA, 1997, pp. 423–430.

[184] Evangelisti, M., Candini, A., Ghirri, A., Affronte, M., Piligkos, S., Brechin, E. K., and McInnes, E. J., "Molecular nanoclusters as magnetic refrigerants: The case of Fe14 with very large spin ground-state," *Polyhedron*, Vol. 24, No. 16, 2005, pp. 2573–2578.

[185] Evangelisti, M., Roubeau, O., Palacios, E., Camón, A., Hooper, T. N., Brechin, E. K., and Alonso, J. J., "Cryogenic Magnetocaloric Effect in a Ferromagnetic Molecular Dimer," *Angew. Chem. Int. Ed.*, Vol. 50, No. 29, 2011, pp. 6606–6609.